Drop and spray impact onto a hot substrate: Dynamics and heat transfer

Vom Fachbereich Maschinenbau
der Technischen Universität Darmstadt
zur
Erlangung des Grades eines Doktor-Ingenieurs (Dr.-Ing.)
genehmigte

Dissertation

vorgelegt von

Jan Breitenbach, M.Sc.

aus Frankfurt am Main

Berichterstatter:	Prof. Dr.-Ing. C. Tropea
1. Mitberichterstatter:	Apl. Prof. Dr. I.V. Roisman
2. Mitberichterstatter:	Prof. Dr.-Ing. G. Brenn
Tag der Einreichung:	15.10.2018
Tag der mündlichen Prüfung:	18.12.2018

Darmstadt 2018

D 17

Breitenbach, Jan:
Drop and spray impact onto a hot substrate: Dynamics and heat transfer
Darmstadt, Technische Universität Darmstadt
Jahr der Veröffentlichung der Dissertation auf TUprints: 2019
Tag der mündlichen Prüfung: 18.12.2018

Bitte zitieren Sie dieses Dokument als:
URN: urn:nbn:de:tuda-tuprints-80970
URL: http://tuprints.ulb.tu-darmstadt.de/id/eprint/8097

Dedicated to my grandparents...

Abstract

Non-isothermal spray/wall interaction is an important process encountered in a large number of existing and emerging technologies, such as fuel injection in aircraft gas engines and internal combustion engines, and is the underlying phenomenon associated with spray cooling technology. Spray cooling is a very promising technique for the cooling of devices with very high heat flux densities (as encountered in the fields of metalworking, cooling of electronic components or light-water nuclear reactors), surpassing all other conventional cooling methods. The effectiveness of spray cooling is influenced by a large number of parameters, including spray characteristics like drop size, velocity and number density, the surface morphology, but also by the temperature range and thermal properties of the materials involved. Indeed, the temperature of the substrate can have significant influence on the hydrodynamics of drop and spray impact, an aspect which is seldom considered in model formulation. This process is extremely complex and current approaches are highly empirical in nature.

In the present thesis the single drop impact as a central element of spray impact is experimentally investigated for various thermodynamic and hydrodynamic conditions. Understanding single drop impact is an important and necessary preliminary work in the description and modeling of non-isothermal spray impact. The observed outcomes of single drop impact are classified for various impact conditions according to the well-known heat transfer regimes: single phase cooling, nucleate boiling, transition boiling and film boiling. Observations from the present work also introduce the thermal atomization regime. The phenomenon is characterized by the dewetting of the substrate, caused not by rim dynamics but induced by thermal effects, and an intensive evaporation leading to a fine secondary spray.

Various theoretical considerations for the heat transfer regimes single phase cooling, nucleate boiling, thermal atomization and film boiling are obtained to describe the quantities involved in the non-isothermal drop impact. The theories allow predictions of the heat transferred from the hot substrate to the impinging drop, the typical time of drop contact, and the secondary spray. These quantities are of paramount importance for spray cooling application, since they can be used to determine the optimum spray. The theoretical predictions account for the underlying physical phenomena and are validated with existing data. Finally, the consideration for the single drop impact is used for the development of a theoretical model for an average heat transfer coefficient for spray cooling in the film boiling regime. The model captures the influence of spray characteristics and accounts for the probability of drop interactions on the wall, when the droplet number density in the spray is high. The theory agrees well with existing experimental data.

Kurzfassung

Der Tropfenaufprall auf beheizte Wände ist ein wichtiger Prozess in vielen industriellen Anwendungen, wie bspw. bei der Kraftstoffeinspritzung von Verbrennungsmotoren und Gasturbinen, sowie ist ein grundlegender Bestandteil der Sprühkühlungstechnologie. Die Sprühkühlung ist eine sehr bedeutende Technik zur Kühlung von Materialien mit sehr hohen Wärmestromdichten und übertrifft alle herkömmlichen Kühlmethoden. Dies ist besonders in der Metallverarbeitung oder der Kühlung von Elektronikkomponenten von großer Bedeutung. Die Wirksamkeit der Sprühkühlung wird durch eine Vielzahl von Parametern beeinflusst, darunter Sprühparameter wie Tropfengröße, Geschwindigkeit und Anzahldichte, die Oberflächenmorphologie, aber auch der Temperaturbereich und die thermischen Eigenschaften der beteiligten Materialien. In der Tat kann die Temperatur des Substrats einen signifikanten Einfluss auf die Hydrodynamik des Tropfen- und Sprayaufpralls haben. Daher ist dieser Prozess äußerst komplex und aktuelle Modellierungsansätze sind weitestgehend empirischer Natur.

In der vorliegenden Arbeit wird der Einzeltropfenaufprall als zentrales Element des Sprayaufpralls für verschiedene thermodynamische und hydrodynamische Randbedingungen experimentell untersucht. Das Verständnis des Einzeltropfenaufpralls ist eine wichtige und notwendige Vorarbeit bei der Beschreibung und Modellierung des Sprayaufpralls auf eine beheizte Wand. Die beobachteten Ergebnisse des Einzeltropfenaufpralls werden für verschiedene Aufprallbedingungen gemäß der bekannten Wärmeübertragungsregime klassifiziert: Reine Konvektion, Blasensieden, Übergangssieden und Filmsieden. Beobachtungen aus der vorliegenden Arbeit ergänzen zusätzlich das Regime "Thermal Atomization". Dieses Regime ist durch die Entnetzung des Tropfens gekennzeichnet, welche durch thermische Effekte verursacht wird und zu einer intensiven Verdampfung, sowie einer feinen Sekundärzerstäubung führt.

Für die beschriebenen Wärmeübertragungsregime werden weiterführend theoretische Modelle entwickelt, um die an dem Tropfenaufprall beteiligten Einflussgrößen zu quantifizieren. Die Modelle erlauben die Bestimmung der Wärmeströme vom heißen Substrat auf den aufprallenden Tropfen, die typische Zeit des Tropfenkontakts, sowie die Charakteristika des Sekundärsprays. Diese Kenngrößen sind für die Sprühkühlung von größter Wichtigkeit, da sie zur Bestimmung eines optimalen Sprays verwendet werden können. Die theoretischen Modelle berücksichtigen die zugrunde liegenden physikalischen Phänomene und werden mit existierenden Daten validiert. Schlussendlich werden die Erkenntnisse des Einzeltropfenaufpralls für die Entwicklung eines theoretischen Modells des Wärmeübertragungskoeffizienten für die Sprühkühlung im Filmsiedeverfahren verwendet. Das Modell erfasst den Einfluss der Parameter des Sprays und berücksichtigt die Wahrscheinlichkeit von Tropfeninteraktionen auf der Wand, wenn die Dichte der Tropfen im Spray hoch ist. Ein Vergleich mit vorhandenen experimentellen Daten zeigt eine gute Übereinstimmung mit dem entwickelten Modell.

Acknowledgments

First of all I would like to thank my supervisors Apl. Prof. Ilia V. Roisman and Prof. Cameron Tropea for the confidence and giving me the opportunity to conduct my research at the Institute for Fluid Dynamics and Aerodynamics (SLA) of the Technische Universität Darmstadt. The unique facilities and equipment helped and contributed a lot to this thesis. In particular, working for the SLA in Griesheim was always a pleasure for me. Furthermore, special thanks to Prof. Brenn from TU Graz for fruitful discussions during the SFB-TRR 75 Summer School and for refereeing my thesis.

The financial support from the German Research Foundation (DFG) under grant SFB-TRR-75 is gratefully acknowledged. My project gave me the opportunity to meet many people at places all around the world, which inspired and developed myself professionally. In particular I want to mention the colleagues from the SFB-TRR-75 and from the Institute for Fluid Dynamics and Aerodynamics (SLA) of the Technische Universität Darmstadt.

Without the help of students my research would not have been so successful. The long list underlines the support I experienced: Markus Rieken, Benedikt Schmidt, Patrick Hoppe de Palet dos Santos, David Kirchhoff, Sebastian Dehe, Johannes Hartmann, Marcel Neu, Hendrik Nicolai, Jens Schelbert, Christian Becker, Marco Becker, Alessio Cipolla, Johannes Kissing, Pakorn Thongraya, Louis Reitter und Niels Paul v. Kieckebusch.

Special thanks to my former and current roommates at SLA Lars Opfer, Maximilian Kuhnhenn and Patrick Seiler who worked with me during the years. In addition I want to thank all former and current colleagues from SLA for such a wonderful time at the campus in Griesheim and Lichtwiese. A very special word of thanks goes to Birgit Neuthe, Stepahnie Lath, Petra Fuhrmann and Corinna Neumann from the administrative team, to Ilona Kaufhold, Martin Weiß and their workshop teams. My work during the years couldn't have been successfully performed without their support. A big thanks goes to Benjamin Lambie and Hubertus Marschall for their help and for always having an open door for me. Many thanks to Maximilian Kuhnhenn and Johannes Feldmann for proof reading this thesis.

Finally, I would like to thank my family and friends for the support during my time in Darmstadt and abroad. Particularly, special thanks goes to Lena who supported me the last years. Without your love, passion and inspiration I wouldn't be so successful.

Thank you.

Jan

Contents

1 Introduction

Section 1.1 in the present chapter provides a main motivation of the study followed by a critical review of the non-isothermal drop/wall and spray/wall interaction in section 1.2. The chapter closes with the objectives and outlines of the present thesis in section 1.3. Parts of the following sections have been published in Breitenbach et al. (2017a,b, 2018a,b).

1.1 Motivation

The study of a spray impact onto a heated wall is motivated by a wide range of industrial applications such as spray cooling (Estes & Mudawar, 1995; Lin & Ponnappan, 2003; Kim, 2007) or fuel injection in aircraft gas engines and internal combustion engines (Rolls Royce, 2015; Naber & Reitz, 1988). For instance, during spray injection in internal combustion engines and aircraft gas turbines the fuel may strike cylinder walls or walls of the intake valve (Bai & Gosman, 1995). In these cases, fuel deposition on the wall can cause adverse effects by developing a liquid film on the wall, which leads to unburned hydrocarbons and increased emissions. Furthermore, the impact is often accompanied by the generation of multiple secondary droplets. Their characteristics are important parameters since they affect mixture formation, its combustion and deposition of coke residues. In order to optimize combustion processes and to make it more efficient or to reduce pollutants, fuel injection has been explored more in detail over the recent years (Moreira et al., 2010).

Spray cooling technology is a promising technique for the cooling of devices with very high heat flux densities (Yang et al., 1996; Rini et al., 2002; Cheng et al., 2016), as encountered in the fields of metal production such as die forging and hot rolling (Chen & Tseng, 1992; Mudawar & Deiters, 1994; Hall & Mudawar, 1995; Aamir et al., 2017), cooling of electronic modules (Tilton et al., 1994; Bar-Cohen et al., 2006; Fabbri et al., 2005), light-water reactors

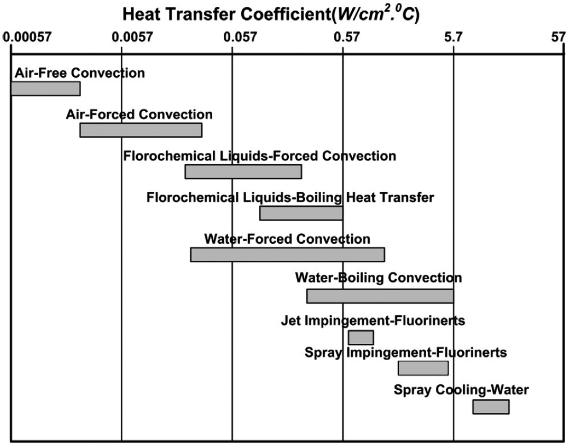

Figure 1.1: Heat transfer coefficients for cooling techniques. (Reprint from Nayak et al. (2016) with permission of Elsevier.)

(Sawan & Carbon, 1975) or of diode laser arrays (Huddle et al., 2000), as well as for cryogenic cooling of human tissues (Nelson et al., 1995; Kelly et al., 1999; Zenzie et al., 2000; Datrice et al., 2006). Moreover, spray cooling determines the phase transformations and influences the emergence of strains in substrate materials during thermal spraying (Gross & Berndt, 1998; Tsui & Clyne, 1997). As shown by the large number of industrial applications spray cooling covers a wide variety of boundary conditions. The temperature range of spray cooling lies between cryogenic temperatures (80 K) (Sehmbey et al., 1995; Cho & Goodson, 2015; Wang et al., 2016) to about 1300 K (Bolle & Moureau, 1982). An important demand in general, but in particular for spray cooling of electronic equipment, is the uniform heat removal from the surface and avoidance of hot spots. Compared to other heat transfer mechanisms, such as forced air or jet impingement, spray cooling has the highest heat transfer coefficient, which is shown schematically in Fig. 1.1.

During spray cooling the formation of a liquid film is undesirable, since this leads to a decrease in the heat transfer rate compared to single spray drops impacting onto a dry, heated surface. Furthermore, a large diversity of the spray impact phenomena is associated with the flow in the liquid layer initiated by single drop impacts onto a wall and their interactions. Due to the complexity of the problem, the hydrodynamics of liquid films created by sprays and the associated heat transfer are not entirely understood. Heat flux during spray cooling is usually measured as a function of the various thermodynamic boiling regimes, mass flux densities and the substrate structure, such as morphology or porosity (Estes & Mudawar, 1995; Lin & Ponnappan, 2003; Silk et al., 2006; Sodtke & Stephan, 2007). Current theoretical approaches, usually presented in the form of empirical correlations or developed as a simple superposition of single drop impacts, disregard to a large extent the physics of drop/spray wall interaction. No universal model predicting the effectiveness of spray cooling over a significant range of operating parameters has been developed to date. The main difficulty in spray research is the fact that most sprays are usually polydisperse. Their behavior is governed by a large number of parameters which cannot be varied and controlled independently. Thus, it is not easy to identify the main influencing parameters or their combinations which define the problem.

Single drop impact onto a dry or wetted substrate is a central element of spray/wall interaction (Yarin et al., 2017). The phenomenon of drop impact onto hot surfaces has been extensively investigated in the past years; however many questions and dependencies remain unclear. For an isothermal drop impact without phase change the outcome (rebound, deposition or splash) is mainly determined by the impact parameters, liquid properties, substrate morphology and wettability (Rioboo et al., 2001; Marengo et al., 2011; Roisman et al., 2015; Josserand & Thoroddsen, 2016) and for the properties of the surrounding gas (Xu et al., 2005; Stevens et al., 2014). Drop impact onto a hot surface can be additionally accompanied by Marangoni effects, nucleate boiling, film boiling, phase change phenomena and other thermodynamic effects. Depending on the substrate temperature, the drop impact outcome can change significantly and additional thermodynamic influences can be observed. At very high substrate temperatures, significantly exceeding the saturation temperature, the liquid does not remain in contact with the solid. The vapor layer dividing the liquid from the hot substrate exhibits a pressure distribution which suspends the impacting drop above the surface (Leidenfrost, 1966).

The impingement of single drops onto a heated wall has been investigated experimentally in a large number of studies (Chandra & Avedisian, 1991; Bernardin & Mudawar, 1997; Bernardin et al., 1996; Tran et al., 2012;

Bertola, 2015; Khavari et al., 2015; Staat et al., 2015). In particular, the influence of the wall temperature, the Weber number, the surface roughness and the liquid properties on the impingement result have been examined in detail. A comprehensive review can be found in Liang & Mudawar (2017a). Nevertheless, it is not completely clear how the results of such investigations with single drops can be used for the modeling of spray impact, in particular for the prediction of the parameters of the secondary spray or of the values of the heat flux.

1.2 Spray cooling models

Different phenomena for the drop impact onto a hot substrate have been observed in literature (Bernardin & Mudawar, 1997; Tran et al., 2012; Bertola, 2015; Staat et al., 2015; Khavari et al., 2015), leading to various thermodynamic boiling phenomena (*e.g. single phase cooling*, *nucleate boiling*, *film boiling*) and hydrodynamic impact outcomes (*e.g. deposition, rebound, breakup*). Depending on the impact parameters and substrate temperature as well as the fluid properties, ambient conditions, the surface wettability and morphology, the drop impact outcome on the heated wall significantly changes. A detailed description of the various thermodynamic boiling phenomena and hydrodynamic impact outcome observed in the present thesis for different substrate temperatures and impact conditions is given in section 3.

In this comprehensive review the physical phenomena accompanying the spray cooling process and their modeling approaches are discussed. Single drop and spray impact are considered in various boiling regimes:

- Spray cooling without boiling (single phase cooling regime), for relatively low temperatures below the boiling onset. The heat transfer is governed mainly by heat conduction in the wall and heat convection in the wall film flow.

- Spray cooling in the nucleate boiling regime. The heat flux in this regime is relatively high, since despite the boiling process, liquid is in contact with the hot substrate. The heat transfer in this regime is governed by the vaporization of the superheated liquid near the substrate, leading to the formation, growth and departure of bubbles. Moreover, the flow associated with the bubbles also intensifies the heat convection. At very high substrate temperatures, intensive thermal drop atomization can occur.

- Spray cooling in the film boiling regime at temperatures above the Leidenfrost point. The heat flux in this regime is relatively low, since a continuous thin vapor layer between the substrate and the liquid acts as an insulating layer and prohibits direct contact of the liquid with the hot substrate.

After a short introduction of the common dimensionless parameters, this review is organized into three main subsequent sections. In section 1.2.1 the drop and spray impact not accompanied by boiling is examined, while in section 1.2.2 and section 1.2.3 the drop and spray impact in which boiling occurs is addressed. In both of these two last sections first nucleate boiling is addressed and then film boiling.

Common dimensionless parameters

The parameters determining the outcome of an isothermal single drop impact are the impact velocity U_0 and initial drop diameter D_0. In the case of drop impact onto a liquid film, the film thickness $\hat{h}_{\mathrm{film}}$ is also an important influencing parameter. The flow generated by drop impact and the hydrodynamic phenomena are determined by the Reynolds and Weber numbers,

$$\mathrm{Re} = \frac{U_0 D_0}{\nu}, \tag{1.1}$$

$$\mathrm{We} = \frac{\rho_l D_0 U_0^2}{\sigma}. \tag{1.2}$$

Here ρ_l, ν and σ are the density, kinematic viscosity and surface tension of the drop liquid.

In some cases it is more convenient to use some combinations of the Reynolds and Weber numbers. Among these combinations are the capillary number and Ohnesorge number:

$$\mathrm{Ca} = \mathrm{We}\,\mathrm{Re}^{-1}, \tag{1.3}$$

$$\mathrm{Oh} = \mathrm{We}^{1/2}\,\mathrm{Re}^{-1}. \tag{1.4}$$

In the case of transient heat transfer, typical for the case of a single drop impact onto a heated wall, the ratio of the thicknesses of the viscous and thermal boundaries are determined by the Prandtl number

$$\mathrm{Pr}_l = \frac{\nu}{\alpha_l}, \tag{1.5}$$

where α_l is the thermal diffusivity of the liquid.

In order to represent the measurement results of non-isothermal impacts in dimensionless form, further dimensionless numbers, Stanton, Nusselt and Jakob numbers, involving only the physical parameters influencing the heat transfer in the wall film, are introduced:

$$\mathrm{St} = \frac{\dot{q}}{c_p j_m \Delta T}, \tag{1.6}$$

$$\mathrm{Nu} = \frac{\hat{h}_{\mathrm{film}} \dot{q}}{\lambda_l \Delta T}, \tag{1.7}$$

$$\mathrm{Ja} = \frac{c_p \Delta T}{L}, \tag{1.8}$$

respectively. Here $\dot{q}$ is the heat flux, j_m is the spray mass flux, ΔT is the temperature difference between the substrate and the fluid, c_p, λ_l and L are the heat capacity, the thermal conductivity and the latent heat of evaporation of the liquid.

1.2.1 Drop and spray impact without boiling

Hydrodynamics of isothermal drop impact are already well understood and described. Most of the phenomena were observed already in the detailed pioneering work of Worthington (1876); Worthington & Cole (1897). Drop spreading and receding are governed by the dynamics of the rim, formed by capillary forces. In some cases the rim is unstable and drop impact leads to breakup. Various impact outcomes for an isothermal drop impact are shown in Fig. 1.2: depostion, prompt and corona splash, receding breakup, partial rebound and rebound. Comprehensive reviews on the phenomena and modeling of isothermal drop impact can be found in Yarin (2006); Marengo et al. (2011); Roisman et al. (2015); Josserand & Thoroddsen (2016); Yarin et al. (2017). In this survey only the phenomena relevant to the modeling of spray cooling will be considered.

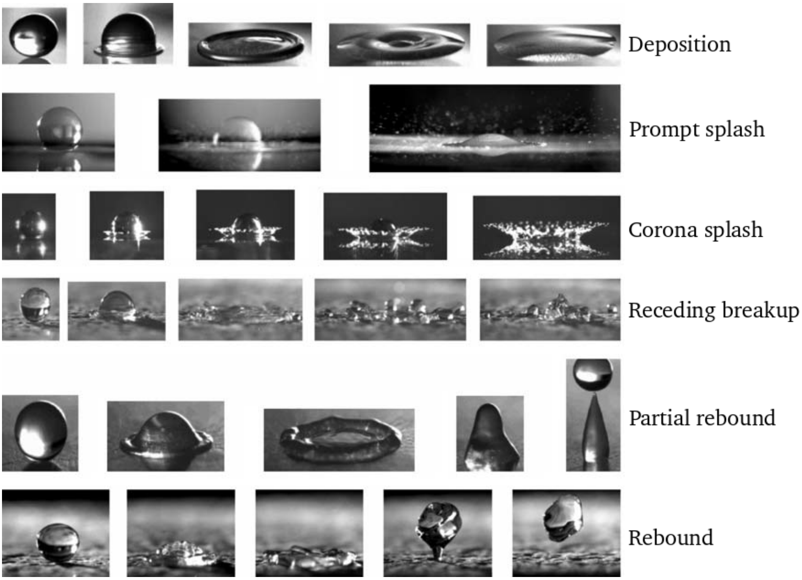

Figure 1.2: Isothermal drop impact outcome: drop deposition, corona and prompt splash, partial or complete rebound. (Reprint of Rioboo et al. (2001) with permission of Begel House Inc.)

Drop impact onto a solid substrate: hydrodynamics and heat transfer

Drop impact onto a dry substrate is an important phenomenon related to spray cooling at the very initial phase of spray impingement, when a liquid film has not yet accumulated on the surface. It is also important for the dry spots on hydrophobic substrates, which form due to intensive evaporation of a wall film. Similarly, this phenomenon is dominant in cases of fast evaporation of very small drops on the substrate, which prevents formation of a wall film. In the following sections several aspects will be considered regarding drop impact without boiling.

Drop impact dynamics: When a drop impacts onto a solid substrate it generates a radially expanding flow in a thinning lamella of nearly uniform thickness (Yarin & Weiss, 1995). This lamella is bounded by a rim, created by capillary forces and the stresses associated with the liquid viscosity (Taylor, 1959; Roisman et al., 2002). An inviscid, remote approximate solution for the velocity field in a thin expanding lamella, valid for impacts at high Reynolds and Weber numbers and which satisfies the mass balance and momentum balance equations, is obtained in Yarin & Weiss (1995) in the form

$$v_{r0} = \frac{r}{t+\tau}, \quad v_{z0} = -\frac{2z}{t+\tau}, \tag{1.9}$$

where r and z are the radial and axial coordinates, v_{r0} and v_{z0} are the corresponding components of the velocity field, t is the time after impact and τ is a time constant. This flow field is valid outside the viscous boundary layer, which develops on the substrate wall.

A more general, exact similarity solution, which accounts for the liquid viscosity, is obtained in Roisman (2009)

$$v_r = \frac{r}{t} g'(\xi), \quad v_z = -2\sqrt{\frac{\nu}{t}} g(\xi), \quad \xi \equiv \frac{z}{\sqrt{\nu t}}, \tag{1.10}$$

where the dimensionless function $g(\xi)$ of the similarity variable ξ is obtained by numerical solution of the ordinary differential equation

$$g''' + 2gg'' + \frac{1}{2}\xi g'' + g' - g'^2 = 0, \tag{1.11}$$

subject to the boundary conditions

$$g = 0, \quad g' = 0, \qquad \text{at} \qquad \xi = 0, \tag{1.12}$$

$$g' = 1, \qquad \text{at} \qquad \xi \to \infty. \tag{1.13}$$

The analysis in Roisman (2009) yields an expression for the residual thickness of the lamella, formed by viscosity

$$h_{\text{res}} \approx 0.79 D_0 \text{Re}^{-2/5}. \tag{1.14}$$

Maximum spreading diameter: The value of the maximum spreading diameter determines the contact area between the impacting drop and the substrate and is therefore an important parameter influencing heat flux during spray cooling. The maximum spreading diameter and the spreading dynamics during drop impact has been experimentally investigated from millimeter drops (Chen, 1977; Lagubeau et al., 2012) to small micrometer drops (van Dam & Clerc, 2004; Visser et al., 2015).

It is convenient to define a maximum spreading diameter (or spreading factor) as $\overline{D}_{\max} \equiv D_{\max}/D_0$. The scaling of Clanet et al. (2004) for the dimensionless maximum spreading diameter, $\overline{D}_{\max}\mathrm{Re}^{-1/5}$ of a drop impacting onto a dry superhydrophobic substrate is determined as a function of the dimensionless impact parameter $\Lambda = \mathrm{We}\,\mathrm{Re}^{-4/5}$. For the impact of a low viscosity liquid ($\Lambda < 1$) the maximum drop diameter is determined exclusively by the capillary number and can be scaled as $\overline{D}_{\max} \sim \mathrm{We}^{1/4}$. In the viscous regime ($\Lambda > 1$) the maximum drop diameter is determined mainly by the impact Reynolds number, $\overline{D}_{\max} \sim \mathrm{Re}^{1/5}$.

Marmanis & Thoroddsen (1996) and Scheller & Bousfield (1995) have found that the dimensionless maximum spreading diameter scaled by the initial drop diameter, $\overline{D}_{\max}$, correlates well with the dimensionless parameter $\mathrm{K} = \mathrm{Re}^{1/2}\mathrm{We}^{1/4}$, first introduced by Walzel (1980). For example, Scheller & Bousfield (1995) proposed the following empirical correlation

$$\overline{D}_{\max} = 0.61\,\mathrm{K}^{0.332}. \tag{1.15}$$

Some estimations have been obtained using the energy balance of the impacting drop (Collings et al., 1990; Chandra & Avedisian, 1991; Fukai et al., 1995; Pasandideh-Fard et al., 1996; Wildeman et al., 2016), which compares the initial kinetic and surface energy of the impacting drop with the surface energy of the spreading lamella, accounting for the energy lost due to the viscous dissipation. Models of this type (Ukiwe & Kwok, 2005) predict the dimensionless maximum spreading diameter as the root of the following algebraic equation

$$\begin{aligned} A\overline{D}^3_{\max} &- B\overline{D}_{\max} + 8 = 0, && (1.16)\\ A &= 3(1-\cos\theta_c) + 4\mathrm{We}\,\mathrm{Re}^{-1/2}, && (1.17)\\ B &= \mathrm{We} + 12, && (1.18) \end{aligned}$$

where θ_c is the contact angle of the substrate.

The model for the maximum spreading diameter from Roisman (2009) uses the residual lamella thickness h_{res}, defined in Eq. (1.14), as a characteristic length scale, and accounts for the motion of the rim under action of surface tension

$$\overline{D}_{\max} = 0.87\mathrm{Re}^{1/5} - 0.40\mathrm{Re}^{2/5}\mathrm{We}^{-1/2}. \tag{1.19}$$

This expression agrees well with the existing experimental data for a wide range of the impact parameters. For relatively low Weber number and high contact angle the expression (1.19) slightly overpredicts the value of the spreading factor. Therefore, the following expression is recommended (Butt et al., 2014)

$$\overline{D}_{\max} = 0.87\mathrm{Re}^{1/5} - 0.48\mathrm{Re}^{2/5}\mathrm{We}^{-1/2},\ (\theta_c \to \pi), \tag{1.20}$$

for superhydrophobic substrates.

Drop splash: It is obvious, that the value of the maximum spreading diameter can be influenced by different outcomes which are observed at different impact velocities. Rioboo et al. (2001) identified the following outcomes: drop deposition, corona splash and prompt splash, partial or complete rebound (c.f. Fig. 1.2).

It is known that the splashing threshold for corona splash of a drop impacting onto a dry smooth substrate is influenced by the mechanical properties of the ambient gas, which can be varied by changing the ambient pressure (Xu et al., 2005). Many attempts have been made to correlate the splashing threshold using the well-known parameter $\mathrm{K} \equiv \mathrm{We}^{1/2}\mathrm{Re}^{1/4}$. Recent experiments (Vander Wal et al., 2006; Bird et al., 2009; Palacios et al., 2013; Pan et al., 2010) have shown that this parameter is applicable only for a rather narrow range of drop impact parameters. Currently the correlation for the boundary between drop deposition and corona splash, which is based on the existing experimental observations, is expressed in Roisman et al. (2015) as:

$$\mathrm{Ca}_{\mathrm{corona}} = 0,067 + 0,60\mathrm{Oh}^{0.35} \quad \text{for Re} < 450, \tag{1.21}$$

$$\mathrm{Oh}_{\mathrm{corona}} = 0.0044 \quad \text{for Re} > 450. \tag{1.22}$$

Substrate morphology and porosity are also significant influencing factors (Rioboo et al., 2008; Moita & Moreira, 2012; Lembach et al., 2010). Roughness promotes the phenomenon of prompt splash and porosity leads to the partial liquid penetration and subsequent target imbibition. The splashing threshold is determined mainly by the characteristic local inclination of the surface structures. The critical Weber number for prompt splash on rough and structured surfaces is determined in Roisman et al. (2015)

$$\mathrm{We}_{\mathrm{prompt}} \approx 10\,(\mathrm{Rpk}/\mathrm{Rsm})^{-0.83}, \tag{1.23}$$

where Rpk is the average height of protruding peaks above the roughness core profile and Rsm is the mean width of a profile element.

Heat transfer during drop impact: Theoretical predictions in literature for heat transfer during drop impact without boiling are often only based on heat conduction in the fluid, while neglecting the internal fluid motion (Liang & Mudawar, 2017a). The contact temperature and the heat flux at the liquid/wall interface is estimated similar to the heat conduction problem of two semi-infinite solid bodies (Myers, 1987):

$$T_c = \frac{e_\mathrm{w} T_{\mathrm{w}0} + e_l T_{d0}}{e_\mathrm{w} + e_l}, \tag{1.24}$$

$$\dot{q}(t) = \frac{e_l e_\mathrm{w}(T_{\mathrm{w}0} - T_{d0})}{(e_l + e_\mathrm{w})\sqrt{\pi}\sqrt{t}}. \tag{1.25}$$

Here e_l and e_w are the thermal effusivities of the liquid and solid. However, this is a critical assumption since the heat transfer in the drop is significantly influenced by the fluid flow (Batzdorf, 2016). In Roisman (2010) a theoretical model for the heat transfer without phase change is developed using an similarity solution which also accounts for the fluid motion and heat convection in the spreading drop. It has been recently validated by comparison with the predictions of the direct numerical simulations for single (Berberović et al., 2011; Schremb et al., 2017) drop impacts onto a heated substrate. The heat transfer model will be explained more in detail in section 4.1.2.

In many cases special attention has to be paid to the heat transfer phenomena in the vicinity of the moving contact line. Kunkelmann et al. (2012) and Herbert et al. (2013) have demonstrated that the contribution of the near-contact-line convection is significant during the receding phase or during sessile drop evaporation.

The effect of sessile drop evaporation on spray cooling is especially important if the drops are so small that their evaporation time is smaller than the typical spray impact time (typical expectation time of the next impacting drop at the same place). Lopes et al. (2013) have computed the evaporation process of sessile drops at various combinations of thermal properties of the substrates and liquids. They have shown that the transient effects are significant for the description of the process. A comprehensive review of the drop evaporation phenomena and the state of the art of modeling these phenomena can be found in Cazabat & Guena (2010); Erbil (2012) and Brutin (2015).

Spray cooling without boiling

Since spray cooling in the single phase cooling regime is not accompanied by boiling, the heat transfer rates between the spray and the wall are relatively low compared to regimes accompanied by boiling. For this reason, spray cooling without boiling is not the main focus of the heat transfer literature in comparison to spray cooling at different boiling regimes, *e.g* nucleate or film boiling. Nevertheless it is a relevant research topic (*e.g* for cooling of micro electronic components) and valuable research has been performed in the past investigating the non-boiling regime (Oliphant et al., 1998; Rybicki & Mudawar, 2006; Karwa et al., 2007; Wang et al., 2010; Hsieh et al., 2014). Even so, correlations for the relevant heat transfer quantities in the single phase cooling regime are mainly empirical in nature. As a result, multiple empirical correlations of the Nusselt number can be found in the literature, basically in the form

$$\mathrm{Nu} = C\,\mathrm{Re}^a\,\mathrm{Pr}_l^b, \tag{1.26}$$

based on the Reynolds number of the spray and the Prandtl number of the liquid. Although not uniformly interpreted, the Reynolds number is often based on the Sauter mean diameter of the spray as a length scale and the mean volumetric spray flux per unit area as a characteristic velocity. The coefficients a, b and C are empirical constants determined by experimental results. A comprehensive review of these empirical correlations are reported in Liang & Mudawar (2017b).

A very simple physics-based correlation of the heat transfer rate during spray cooling without boiling can be found in Shedd (2007). It is based on the hypothesis that the liquid film on the wall can be approximated as a turbulent liquid layer flowing over a thin viscous boundary layer. Within the viscous boundary layer of the liquid film the heat is transferred by conduction within a thermal boundary layer near the solid wall. The correlation was verified for different coolants with a wide range of properties.

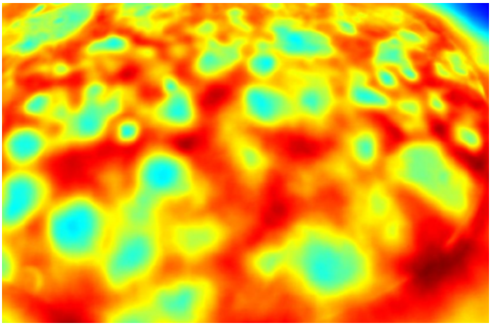

Figure 1.3: Spray-cooled target in microgravity environment captured with an infrared camera (Kyriopoulos, 2010). Red and yellow regions correspond to hot water film covering the target. Light blue and turquoise regions correspond to locations of recent impingement of cold droplets. (Reprinted from Breitenbach et al. (2018b), with permission of Springer Nature. © 2018 Springer Nature.)

Nonetheless, for the development of more comprehensive physical correlations it is essential to enhance the understanding of the physical mechanisms during the spray cooling process. Figure 1.3 illustrates an infrared image of the spray-cooled target (Kyriopoulos, 2010). The oscillating liquid film completely covers the target surface and cools it down. The regions highlighted in red and yellow correspond to the already heated liquid film covering the target, whereas the light blue and turquoise regions correspond to locations of recent cold drop impacts. Therefore, in the regime in which evaporation is not a significant factor, cooling is caused mainly by flow generated by single drop impacts.

A model for spray cooling has to consider the combined effects of the flow in the wall film, craters formed by single drop impacts and splash. Such a model has not yet been developed, since the phenomena are rather complicated.

As a first step we consider a case when the film thickness is much larger than the drop diameter in spray. For a rough estimation of the heat transfer, consider also a time-averaged, quasi-steady heat and flow fields in a liquid wall film. In this case a one-dimensional energy equation in the liquid film in the normal z-direction can be written in the form (Brenn, 2017)

$$v_z \frac{\partial T_l}{\partial z} - \alpha_l \frac{\partial^2 T_l}{\partial z^2} = 0, \tag{1.27}$$

where v_z is the normal component of the liquid velocity and T_l is the temperature. The temperature $T_l(z)$ in the liquid film has to satisfy the boundary conditions

$$T_l(0) = T_\mathrm{w}, \tag{1.28}$$

$$T_l(\hat{h}_\mathrm{film}) = T_s, \tag{1.29}$$

where $\hat{h}_\mathrm{film}$ is the average film thickness, T_w is the wall temperature, and T_s is the spray temperature. The velocity distribution can be approximated as

$$v_z = -\frac{Wz}{\hat{h}_\mathrm{film}}, \tag{1.30}$$

where W is a typical surface velocity, generated by drop impact and by the total spray volumetric flux. The typical velocity scale W can be determined from an accurate description of the flow in the wall film. As a zero approximation we estimate W as a momentum flux averaged velocity (Roisman & Tropea, 2005):

$$W = \sqrt{\frac{j_m U_0}{\rho_l}}, \tag{1.31}$$

where U_0 is the average impact velocity, j_m is the mass flux of the primary, impacting spray.

The solution of equation (1.27) is

$$T_l(z) = T_\mathrm{w} - (T_\mathrm{w} - T_s)\,\mathrm{erf}\left[\sqrt{\frac{X}{2}}\frac{z}{\hat{h}_\mathrm{film}}\right]/\mathrm{erf}\left[\sqrt{\frac{X}{2}}\right], \tag{1.32}$$

$$X \equiv \frac{W\hat{h}_\mathrm{film}}{\alpha_l}. \tag{1.33}$$

From this solution the Nusselt number can be determined using its definition in Eq. (1.7)

$$\mathrm{Nu} = \sqrt{\frac{2X}{\pi}}/\mathrm{erf}\left[\sqrt{\frac{X}{2}}\right]. \tag{1.34}$$

Expression (1.34) provides a very rough estimation for the Nusselt number. It is valid only for the cases if the thickness of the thermal boundary layer is much smaller than the film thickness, namely if $X \gg 1$, and if the film

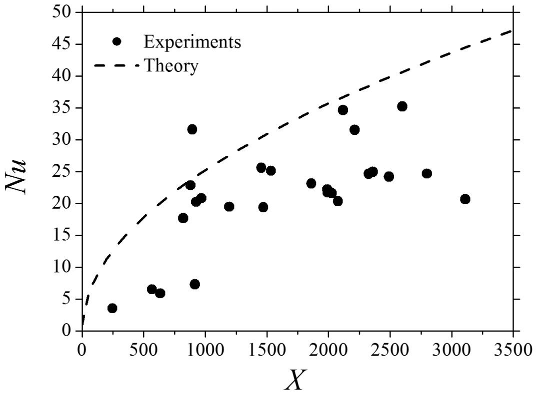

Figure 1.4: Nusselt number for spray cooling. Comparison of the experimental data obtained in Kyriopoulos (2010) with the theoretical prediction from Eq. (1.34). (Reprinted from Breitenbach et al. (2018b), with permission of Springer Nature. © 2018 Springer Nature.)

thickness is much larger than the initial drop diameter. In Fig. 1.4 the experimental data from Kyriopoulos (2010) for the Nusselt number is compared with the theoretical predictions (1.34). It can be clearly seen that the theory predicts well the order of magnitude for the Nusselt number, and can be considered as its upper bound. It should be stressed that there is no adjustable parameters in the model (1.34) which indicates that the main physics of the problem is accounted for.

1.2.2 Drop impact accompanied by boiling

Bubble nucleation and growth in the nucleate boiling regime

The dynamics of bubble growth during drop spreading are influenced by the flow in the expanding lamella and by the pressure variation during drop impact. However, heterogeneous nucleation and bubble growth, associated with the pool boiling regime, has been studied rather extensively. Two main regimes of the bubble growth are considered - inertia dominated growth and heat-transfer-controlled growth (Carey, 1992). The bubble radius, after some waiting period, expands as the square root of time

$$R_B = \beta t^{1/2}, \tag{1.35}$$

where factor β is determined by the thermodynamic material properties and the initial temperatures of the substrate and the liquid.

In many existing theoretical solutions for the bubble growth (Forster & Zuber, 1954; Griffith, 1958; Mikic & Rohsenow, 1969), the temperature of the wall interface exposed to the bubble is assumed to be close to the saturation temperature T_{sat}. The reason for this is the existence of a thin evaporating liquid film on the wall. The existence of this wall film is the only possible explanation of the fact that the bubble reaches sizes much larger than the thermal boundary layer (the majority of the bubble surface is therefore located in the relatively cold region of the drop). This liquid film beneath the bubble is formed by a process similar to dip coating (Landau & Levich, 1988; Van Stralen et al., 1975) and is usually referred as evaporation microlayer. The wall temperature below the bubble only slightly exceeds the saturation temperature, since the liquid film thickness is rather small. Outside the bubble, near the interface, a relaxation microlayer is usually considered. A sketch of the vapor bubble with surrounding liquid on the heated wall is schematically shown in Fig. 1.5.

The thickness of the evaporating layer (Van Stralen et al., 1975) is determined by the thickness of the laminar boundary layer

$$h_{l0} = 3.012 \left(\frac{\nu}{\beta^2} \right) \mathrm{Pr}_l^{-1/3} R_B. \tag{1.36}$$

As soon as the wall film evaporates, temperature fluctuations are possible, which also immediately influence the evolution of the bubble radius. At this stage a thin adsorbed film beneath the bubble is assumed in Stephan & Hammer (1994) and the evaporation occurs mainly in the micro-region of an advancing contact line. In this case the boundary condition at the interface beneath the bubble is the vanishing of the heat flux in the area beneath the bubble.

In the model by Bernardin & Mudawar (2002) the existence of the evaporating microlayer is completely neglected, the contact temperature is determined from the one-dimensional solution (Myers, 1987), associated with the contact of two solid semi-infinite bodies.

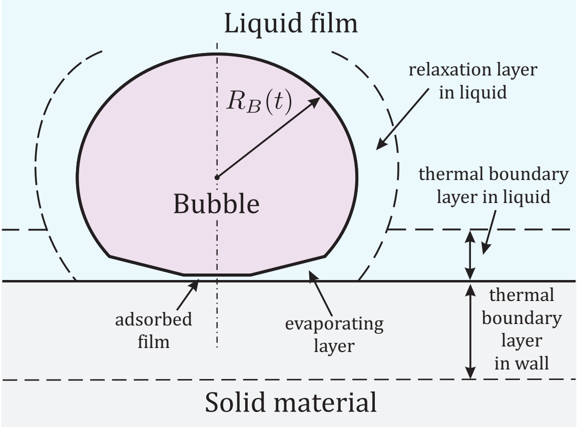

Figure 1.5: Sketch of a heated wall with vapor bubble and surrounding liquid. (Reprinted from Breitenbach et al. (2017a), with permission of the American Physical Society. © 2017 American Physical Society.)

Single drop impact in the nucleate boiling regime

Several studies have been performed in the past investigating the drop impact in the nucleate boiling regime. In the nucleate boiling regime the drop wets the surface after the drop impact until it is completely evaporated. Results for this contact time can be found in Chandra & Avedisian (1991); Tartarini et al. (1999); Abu-Zaid (2004); Buchmüller (2014) and Nakoryakov et al. (2012) for various conditions, *e.g.* liquid properties, impact parameters, surface materials and ambient conditions. Furthermore, in Itaru & Kunihide (1978) an estimation of the evaporation time is presented. The value of the drop contact time is an important quantity since it can help to estimate the heat flux between the substrate and the drop; thus, its knowledge can contribute to the spray impact modeling.

Investigations of the drop impact in the nucleate boiling regime are also often related to the critical heat flux, since it is an important parameter to characterize the efficiency of the cooling process. The critical heat flux is the maximal obtainable heat flux during drop impact in nucleate boiling regime and quantifies departure from the nucleate boiling to the transition boiling regime. Several studies have been performed investigating experimentally the critical heat flux (Kandlikar & Steinke, 2002; McGinnis & Holman, 1969) and a comprehensive review can be found in Liang & Mudawar (2017a). Nonetheless, the physics of drop impact accompanied with boiling are rather complicated, therefore mainly experimental research has been performed in the past leading to various boiling curves and empirical correlations for the heat transfer or the critical heat flux.

Single drop impact in the film boiling regime

At very high substrate temperatures, significantly exceeding the saturation temperature, the liquid does not remain in contact with the solid. The vapor layer dividing the liquid from the hot substrate exhibits a pressure distribution which suspends the impacting drop above the surface (Leidenfrost, 1966). One of the important parameters characterizing this nature of film boiling is the minimum film boiling temperature (or Leidenfrost temperature). The phenomenon has been extensively investigated in the past and various experiments have been performed characterizing the Leidenfrost temperature for different liquid properties, surface morphologies and ambient pressure conditions (Baumeister & Simon, 1973; Testa & Nicotra, 1986; Zhong & Guo, 2017). It has been shown that the Leidenfrost temperature for impinging drops is not a constant, but rather a dynamic value (also called dynamic Leidenfrost temperature) strongly influenced by the impact velocity (Bernardin & Mudawar, 1999; Rein, 2002; Shirota et al., 2016).

A model for the static Leidenfrost temperature is proposed in Berenson (1961); Yao & Henry (1978), which is based on the instability analysis of the vapor/liquid interface or stability of homogeneous nucleation. In Ohtake & Koizumi (2004) the collapse of the vapor film in the film boiling regime is explained by the non-uniformity of the surface heating. The presence of local cold spots on the surface is associated with conditions of the minimum heat flux temperature. Bernardin & Mudawar (2004) has been developed a model for the dynamic Leidenfrost temperature. In this study the bubble nucleation and growth and the interaction with the thermal boundary layer are analyzed. Since the flow in the drop is not known, empirical correlations for the energy loss are introduced into the model, which is finally fitted to the experimental data for the Leidenfrost temperature. The model predicts the rise of the Leidenfrost temperature for higher impact velocities. This observation is confirmed by numerous experimental observations (Celata et al., 2006; Karl et al., 1996; Yao & Cai, 1988). A detailed overview of the Leidenfrost phenomena and their modeling approaches can be found in Quéré (2013) and Liang & Mudawar (2017a).

Another important aspect is the evolution of the spreading diameter and its maximum value $\overline{D}_{\mathrm{max}} = D_{\mathrm{max}}/D_0$, since it influences the cooling effectiveness of the impacting drops. For low viscosity liquids the maximum spreading diameter in the film boiling regime is determined only by the Weber number (Tran et al., 2012; Castanet et al., 2015). The obtained correlation

$$\overline{D}_{\mathrm{max}} = (1 + 0.23\mathrm{We}^{1/2}), \text{ for low viscosity,} \tag{1.37}$$

proposed in (Castanet et al., 2015), indicates that the influence of the shear stresses in the vapor layer on the flow in the lamella is negligibly small, since there is no contact between the liquid and solid regions (or the duration of this contact is very short). Contrary to first expectations Chandra & Avedisian (1991) shows that for the same drop impact conditions the spreading factor $\overline{D}_{\mathrm{max}}$ in the film boiling regime is smaller compared to the ratio in the single phase cooling or nucleate boiling regime. This observation can be explained by the surface energy $E_S \sim D_{\mathrm{max}}^2 \sigma/(1 - \cos\theta_c)$ of the deformed drop (Ford & Furmidge, 1967). For smaller contact angles θ_c less energy is expended by deforming the drop, in consequence for the same kinetic energy the maximum drop spreading is larger. Observations of Chandra & Avedisian (1991) reveal that the contact angle during maximum spreading is much smaller ($\theta_c < 120°$) for lower surface temperatures compared to the Leidenfrost conditions ($\theta_c = 180°$). However, Castanet et al. (2015) has been shown that for high viscous liquids the maximum spreading diameter is additionally influenced by the drop viscosity, even if the drop is not in contact with the hot substrate. Consequently, a correction factor is introduced in their model for the spreading factor, which accounts for the viscous stresses. This yields to spreading factor

$$\overline{D}_{\mathrm{max}} = (1 + 0.077\mathrm{We}^{1/2}\mathrm{Re}^{1/5}), \tag{1.38}$$

for low and highly viscous liquids.

A first suggestion for an analytic solution of the drop evaporation time during film boiling has been developed by Gottfried & Bell (1966). It is based on conduction in the vapor layer and heat radiation of the hot substrate. A semi-empirical expression for the total heat transfer between the impinging single droplet and the heated surface during initial contact has been developed for the film boiling regime in Bolle & Moureau (1982) and Bernardin & Mudawar (1997). They claim that the heat transfer effectiveness of a single drop varies with the drop diameter and impact velocity. The study of Inada & Yang (1994) derives a semi-empirical correlation for the heat transfer as a function impact Weber number. However, a detailed overview of further investigations and modeling approaches can be found in the comprehensive review of Liang & Mudawar (2017a).

Overall, heat transfer during film boiling has to include heat conduction in an expanding thermal boundary in the solid wall, heat convection in the vapor layer and heat convection in an expanding thermal boundary in the liquid region. Current approaches usually presented in the form of empirical correlations or neglecting heat convection in the drop.

1.2.3 Spray impact accompanied by boiling

Spray cooling in the nucleate boiling regime

The physics of spray cooling accompanied with boiling are rather complicated, therefore mainly experimental research has been performed in the past for various mass flux densities and spray properties (Estes & Mudawar, 1995; Chen et al., 2002; Lin & Ponnappan, 2003; Deng & Gomez, 2011), surface morphologies (Pais et al., 1992; Zhang et al., 2013, 2014), spray inclination (Visaria & Mudawar, 2008b) and for microgravity (Kato et al., 1995; Elston et al., 2009; Michalak et al., 2010) leading to various boiling curves and empirical correlations for the heat transfer or critical heat flux during spray cooling. Most of the experiments and correlations are reported in the detailed reviews by Kim (2007), Cheng et al. (2016) and Liang & Mudawar (2017b).

Investigations of the spray cooling in the nucleate boiling regime are often related to the critical heat flux, since it is an important parameter to characterize the efficiency of the spray cooling process. The critical heat flux is the maximal obtainable heat flux during spray cooling in nucleate boiling regime and quantifies departure from this regime. A comprehensive experimental database of the critical heat flux for various parameters, *e.g.* fluids and mass flux densities, can be found in Visaria & Mudawar (2008a). Furthermore, a correlation form of the dimensionless critical heat flux for a water spray was first shown in Mudawar & Valentine (1989) and later modified for a wide range of nozzles, fluids, flow rates, subcoolings and inclination angles (Estes & Mudawar, 1995; Visaria & Mudawar, 2008b):

$$q_*^{''} = 2.3 \left(\frac{\rho_l \dot{V}''^2 D_{32}}{\sigma} \right)^{-0.35} . \tag{1.39}$$

Here $\dot{V}''$ is the local volumetric flux of liquid in the spray along the outer periphery of the impact area and D_{32} is the Sauter mean diameter (SMD) of the spray. It has been shown that the empirical correlation (1.39) is in good agreement with various experiments for a wide range of parameters.

Moreover, the dimensionless spray cooling heat transfer in the nucleate boiling regime is correlated in Holman & Kendall (1993) and Hsieh et al. (2004) for subcooled water

$$\mathrm{Bo_m} = 15.6\,\mathrm{We}^{0.59}\,\mathrm{Ja}^{1.68}, \tag{1.40}$$

and for subcooled hydrocarbons

$$\mathrm{Bo_m} = 2.1\,\mathrm{We}^{0.66}\,\mathrm{Ja}^{1.51}, \qquad \text{(R134a)} \tag{1.41}$$

$$\mathrm{Bo_m} = 9.5\,\mathrm{We}^{0.60}\,\mathrm{Ja}^{1.50}, \qquad \text{(R113)} \tag{1.42}$$

where $\mathrm{Bo_m}$ is the modified boiling number according to Ghodbane & Holman (1991). Here the Sauter mean diameter and the mean arithmetic velocity are used as length scale and characteristic velocity to calculate the Weber number of a polydisperse spray. It has been shown that the empirical correlations (1.40)-(1.42) are valid for a large range of spray parameters.

Spray cooling in the film boiling regime

Considerable research has been performed over the past decades investigating spray cooling in the film boiling regime for various aspects, *e.g.* different spray parameter, liquid properties, surface conditions and temperatures, mass fluxes, or nozzle types (Yamanouc, 1968; Saski et al., 1979; Choi & Yao, 1987; Bernardin & Mudawar, 1997; Wendelstorf et al., 2008b; Labergue et al., 2015); however, many questions and dependencies still remain unclear.

Similar to spray impact in the nucleate boiling regime, mainly empirical correlations can be found in literature. Correlations have been developed for polydispersed (Mudawar & Valentine, 1989; Klinzing et al., 1992; Wendelstorf et al., 2008a) and monodispersed sprays (Yao & Choit, 1987; Bernardin & Mudawar, 1997; Yao & Cox, 2002). A comprehensive review of the literature and developed correlations performed in the past for the spray cooling in the film boiling regime can be found in Liang & Mudawar (2017c).

Considering a sparse spray, where the mass flux of the spray is very small, drop interactions can be neglected. Therefore the transferred heat from the hot substrate to the impinging spray can be calculated based on superposition of the transferred heat from the single drop event.

A very simple theoretical model for the heat transfer of a sparse spray, which accounts for rebound motion and sensible heat of the impinging droplets, can be found in Nishio & Kim (1998). The spray heat flux is calculated as the sum of the heat fluxes by single droplets and its multiple rebounds on the hot substrate. It is assumed that the impinging droplets repeat the rebound motions on the hot substrate and the heat flux upon each droplet rebound is proportional to the sensible heat, while the latent heat of evaporation and phase change upon impact is neglected. This simplification is chosen by the authors due to the highly subcooled water used in the experiments.

For a dense spray however, drop interactions on the surface must be taken into account. Therefore, the analysis of drop interaction possibilities during spray cooling in the film boiling regime is important to determine whether the spray is sparse or dense and to estimate the wall film flow at the surface.

1.3 Objectives and outline of the thesis

Numerous applications and industrial processes involve non-isothermal interaction of a spray with hot walls, such as fuel spray injection in internal combustion engines and gas turbines, as well as spray cooling. In recent years a trend towards higher operating temperatures and pressures can be observed during combustion process to make engines and gas turbines more efficiency and reduce pollutants. As well, in spray cooling applications higher heat flux densities are a prerequisite in order to reduce cycle times during the production process. These tendencies require a profound knowledge of the physics and quantities involved in the phenomena, but the progress made over the past years is far from being complete and current approaches are highly empirical in nature.

The present thesis has the objectives to enhance the understanding of non-isothermal spray/wall interactions and to establish more reliable physic-based correlations for the various regimes in order to describe the quantities involved in the non-isothermal spray impact and cooling process. For this purpose, single drop impact as a central element of spray impact is an important and necessary preliminary work. The outline of the thesis is mainly organized into the parts *Drop impact without boiling*, *Drop impact accompanied by boiling*, and *Spray cooling in the film boiling regime*.

Chapter 2 provides a detailed description of the different configurations of the experimental setup and the measurement techniques applied to the characterization of drop impact phenomena.

Chapter 3 introduces various regimes of drop impact observed in the present thesis. A description of the thermodynamic and hydrodynamic phenomena is given followed by a quantitative regime classification in terms of a regime map for different substrate temperatures and impact conditions.

In **Chapter 4** the non-isothermal drop impact in the single phase cooling regime, which is not accompanied by boiling is investigated. It provides a theoretical model for the heat transfer during single drop impact. This quantity is finally used for the development of a heat transfer model for the simultaneous impact of two drops.

Chapter 5 deals with the non-isothermal drop impact accompanied by boiling, *i.e.* in section 5.1 the drop impact in the nucleate boiling regime, in section 5.2 the drop impact in the thermal atomization regime, and in section 5.3 the drop impact in the film boiling regime. In various subsections different theoretical predictions have been introduced in order to describe the quantities involved into the non-isothermal drop impact phenomena, *e.g* heat flux, duration of contact or secondary spray.

In **Chapter 6** the theory for single drops is extended to spray cooling. After introducing a comprehensive drop interaction analysis, the heat transfer in the film boiling regime is calculated for a sparse and dense spray by superposition of single drop events with respect to drop interactions.

Chapter 7 is the closing section, which completes the present thesis with a final conclusion and outlook for future research.

2 Experimental method

In the present chapter the experimental methods for the drop impact investigations are described. Section 2.1 provides a detailed description of the different configurations of the experimental setup, while section 2.2 focuses on the applied measurement techniques for drop characterization, *i.e.* image-based drop characterization and phase Doppler technique. Parts of the following sections have been published in Breitenbach et al. (2017a,b, 2018a) and in Roisman et al. (2018). Furthermore, parts of the experimental setup have been described in the theses of Kissing (2017) and Schmidt (2018).

2.1 Configurations of experimental setup

Two main configurations of experimental setup have been designed to investigate and characterize drop impact phenomena onto a hot surface. For the main experiments of the drop impact onto a hot metallic substrate, a configuration with a side camera position is used, allowing all phenomena to be observed in detail. To visualize the splashing phenomena, the bubble formation and the wetting behavior, a second configuration with a bottom camera position and a transparent heating system have been designed to achieve a bottom view of the impact process.

The experimental setup with a side camera position is shown schematically in Fig. 2.1(a), while the setup for the bottom view observations is shown in Fig. 2.1(b). Both configurations consist of four major subsystems comprising an observation system [Cam 1 and Cam 2] with illumination [LED], a heating system [HS] with temperature control, the drop-on-demand generation system [DG], and a computer control unit [CCU] for control and data acquisition. Each subsystem is explained in more detail in the following sections.

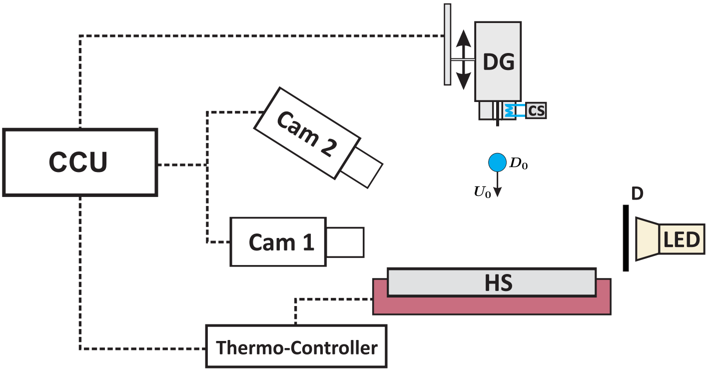

(a)

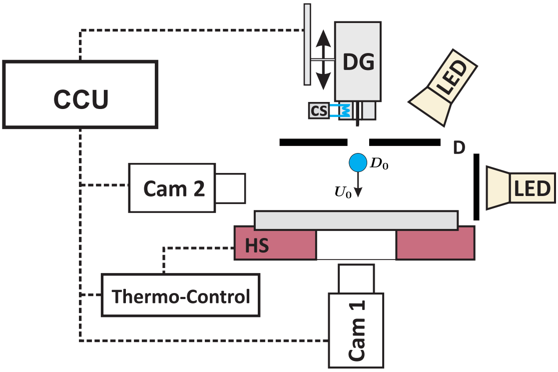

(b)

Figure 2.1: Two configurations of the experimental setup: (a) side camera position for the observations of drop impact and (b) bottom camera position for the observations of the contact dynamics. Both configurations comprise a heating system [HS] controlled by a thermo-controller, drop-on-demand generator [DG] with temperature control [CS], an illumination system [LED] with a diffuser plate [D], a computer control unit [CCU] and high-speed video camera system [Cam 1 and Cam 2].

Observation system

Two CMOS high-speed cameras (*Vision Research Phantom V12.1*) with a maximum resolution of 1280 × 800 pixel at 6242 fps are used to record side-view and top-view images of the drop impact simultaneously. The top-view camera is synchronized by the side-view camera, which is triggered by image based auto trigger of the falling drop. Both high-speed cameras have been equipped with a 60 mm micro lens (*Nikon AF NIKKOR 1:2.8 D*) and spacer rings (*Nikon PK*). With this apparatus a spatial resolution of 12.6 μm/px for the side view and 16.7 μm/px for the top view have been achieved. The illumination system [LED] is a 120 W high power LED spotlight (*Veritas Constellation 120E*) and is placed behind the drop to yield shadowgraphy imaging. To achieve a more uniform illumination a 3 mm optical diffuser plate [D] is placed between the LED spotlight and the drop impact. Since the exposure time of the camera system is much shorter than one microsecond, the LED spotlight has been operated in continuous mode. If a smaller exposure time was required to prevent motion blur, a pulsed *Cavilux HF* high speed diode laser has been used as light source instead of the LED spotlight.

Heating system: side camera position

The heating system [HS] consists of an impact target and a heated copper cylinder. A detailed sectional view of the whole system is shown in Fig. 2.2(a). The impact target is an interchangeable polished aluminum cylinder (*EN AW 7075*) with a diameter of 50.8 mm, embedded in a heated copper cylinder. To achieve a high quality surface the aluminum is processed in several stages with increasing grades of abrasive paper (*Micro Mesh 1500 - 12000* grit) and finally polished with a mirror polishing paste, reaching an average roughness of $R_\mathrm{a} \approx 0.05\,\mu$m for the impact surface. This average value was determined by atomic force microscopy, which is exemplary shown in Fig. 2.2(b). Subsequently, the target was cleaned with isopropyl alcohol to remove polish residuals. Furthermore, from time to time the whole surface is re-polished and re-cleaned to remove dirt and deposits.

To heat the impact surface a 250 W cartridge heater (*hotset hotrod HHP*) is mounted within the heating cylinder, and ceramic with a very low thermal conductivity is used to insulate the sidewalls of the cylinder. The initial temperature of the impact surface is controlled by a PID thermo-controller

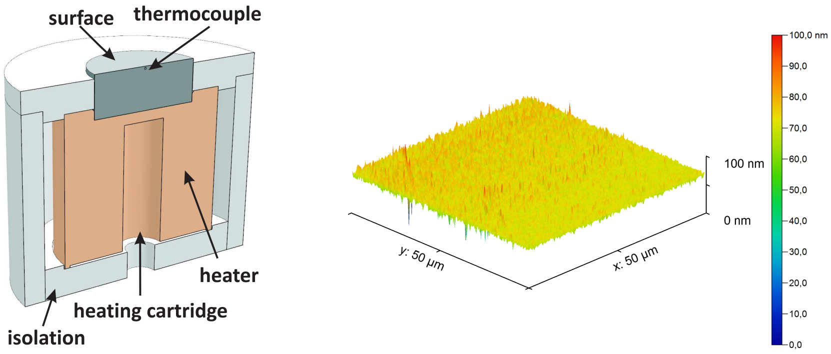

(a) (b)

Figure 2.2: (a) Sectional view of the heating system comprising an aluminum impact target on top of a copper heater, heated by a 250 W cartridge heater and insulated by a ceramic enclosure. A thermocouple is placed 0.5 mm below the impact point on the surface. (b) Atomic force microscopy of the aluminum impact target. (Reprinted (adapted) from Breitenbach et al. (2017a), with permission of the American Physical Society. © 2017 American Physical Society.)

(*hotset c448*) in combination with a calibrated type-J thermocouple (*hotset thermocouple class I*) placed 0.5 mm below the drop impact point on the substrate. The certification of the thermocouple ensures a maximum absolute uncertainty of 1.5 °C according to class I (IEC 60584-1, 2013).

Since the temperature difference between the thermocouple and the impact surface can be neglected, the surface temperature is approximated as the measured substrate temperature of the thermocouple. With the system the initial surface temperature of an aluminum substrate can be varied between $T_{\mathrm{w0}} = 50\,^{\circ}\mathrm{C}$ and $T_{\mathrm{w0}} = 450\,^{\circ}\mathrm{C}$.

Heating system: bottom camera position

To obtain detailed information about the splashing phenomena, bubble formation and wetting behavior, a transparent heating system has been developed. A sectional view of the system is shown in Fig. 2.3(a). To achieve a bottom view of the impact process, the heating system consists of a 3 mm thick transparent sapphire substrate (70 mm in diameter) heated by a cop-

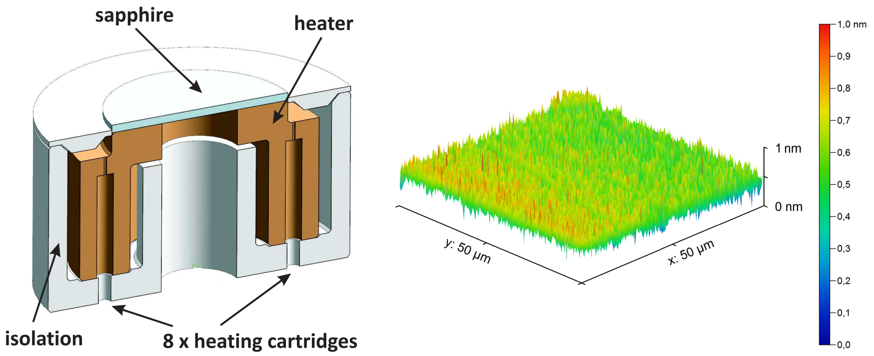

(a) (b)

Figure 2.3: (a) Sectional view of the transparent heating system comprising an transparent sapphire impact target on top of a copper heater, heated by a 250 W cartridge heater and insulated by a ceramic enclosure. (b) Atomic force microscopy of the aluminum impact target.

per ring. An average roughness of $R_\mathrm{a} \approx 0.5\,\mathrm{nm}$ is measured for the sapphire surface. The value is determined by atomic force microscopy which is shown in Fig. 2.3(b). Overall $8 \times 120\,\mathrm{W}$ cartridge heaters (*hotset hotrod HHP*) are placed circumferentially inside the copper ring. Furthermore, to insulate their lateral surface, the copper ring is encapsulated in a low conductive ceramic.

As it is not possible to place a thermocouple inside the sapphire, the surface temperature of the transparent sapphire surface is measured contactless by an infrared thermometer (*Optris CT Laser P7*) with a wavelength of $7.9\,\mu\mathrm{m}$. It has been calibrated at the beginning due to the uncertainty of the unknown emission coefficient of the sapphire. To eliminate the potential influence of long term instabilities, the surface temperature of the sapphire surface was checked before every measurement redundantly with a thermocouple placed on the top of the sapphire surface.

Finally, with the input of the infrared thermometer, the surface temperature is controlled with a *LabVIEW* based PID thermo-controller. Further information about the thermo-controller can be found in Kissing (2017). With the heating system the initial surface temperature of a sapphire substrate can be varied between $T_\mathrm{w0} = 50\,^\circ\mathrm{C}$ and $T_\mathrm{w0} = 450\,^\circ\mathrm{C}$.

Drop generation system

In the experiments the drop is generated by the drop-on-demand generation system [DG]. The drop is produced with a blunt hypodermic needle (*Braun Sterican*) and a piezoelectric micro-pump (*Bartels Mikrotechnik mp6*), which supplies the fluid very slowly from an insulated reservoir trough the needle until a drop detaches due to gravity. To reduce drop oscillations during drop generation the piezoelectric micro-pump is adjusted to a very low flow rate $\dot{V} \approx 50\,\mu\text{l/min}$. The pump is actuated by a function generator (*Bartels Mikrotechnik mp-x*), which is controlled by the computer system. An *Arduino* laser light barrier is aimed to detect the falling drop and trigger the drop generator and the observation system (Kissing, 2017).

The position of the drop generator above the hot surface can be moved by a linear motor. Therefore, different impact velocities have been obtained in the experiments. Neglecting aerodynamic drag forces for low heights Δz_0 of the needle above the impact surface, the impact velocity can be approximated as the theoretical free-fall velocity (Bertola, 2009). The drop diameter can be roughly estimated from a balance of gravity and surface tension forces (Lefebvre & McDonell, 2017):

$$U_0 = \sqrt{2g(\Delta z_0 - D_0)}, \quad D_0 = \left(\frac{6\,d_N \sigma}{\rho_l g}\right)^{1/3}, \tag{2.1}$$

where ρ_l and σ_l are the density and surface tension of the liquid drop, d_N is the outer diameter of the blunt hypodermic needle and g is the gravitational constant. By changing the size of the hypodermic needle (Gauge 18 - 34) and its position above the surface, different drop diameters $D_0 = 1.6 - 3.5\,\text{mm}$ and impact velocities $U_0 = 0.3 - 3.0\,\text{m/s}$ can be realized. For instance, with a needle (Gauge 27) and a height ($\Delta z_0 = 0.10\,\text{m}$) an inital drop with diameter $D_0 = 2.20 \pm 0.05\,\text{mm}$ and impact velocity $U_0 = 1.40 \pm 0.05\,\text{m/s}$ has been obtained. The fluid used in the experiments is highly purified laboratory water (double-distilled). Table 2.1 summarizes the liquid properties of the double-distilled water at a fluid temperature of 25 °C obtained from Wagner & Kretzschmar (2007).

Since the drop generator is placed above the hot substrate, cooling of the fluid system is needed to keep the temperature of the initial drop nearly constant during the experiments. A cooling system [CS] with a water circulation

Table 2.1: Liquid properties of highly purified laboratory water at a fluid temperature of 25 °C obtained from Wagner & Kretzschmar (2007).

Parameter	Symbol	Value
liquid density	ρ_l	$997\,\mathrm{kg/m^3}$
kinematic viscosity	ν	$0.893 \cdot 10^{-6}\,\mathrm{m^2/s}$
surface tension	σ	$71.96\,\mathrm{mN/m}$
thermal conductivity	λ_l	$0.61 \cdot 10^{-3}\,\mathrm{N/m}$
electrical conductivity	γ_l	$0.2\,\mu\mathrm{S/m}$

system in combination with two type-K thermocouples has been designed to control the fluid and needle temperature. As a consequence, the initial drop temperature, measured with a thermocouple within the fluid near the tip of the needle, is nearly constant $T_{d0} \approx 25 - 30\,^\circ\mathrm{C}$ for all the experiments.

Much smaller drops of diameter $D_0 = 0.1 - 0.8\,\mathrm{mm}$ and with a high impact velocity $U_0 = 4.0 - 12.0\,\mathrm{m/s}$ have been generated by a monodisperse piezo-electric drop generator (*FMP technology*). The drop generation is based on Rayleigh decay of a liquid jet. By introducing vibratory disturbances onto the liquid jet very small precise drops have been obtained (FMP Technology GmbH, 2014).

Computer control unit

In the experimental setup a computer control unit is used for control and data acquisition. As shown in Fig. 2.1, the various subsystems are connected to the computer control unit, which serves as a hub of the experimental setup. In the unit, the subsystems are linked with each other to synchronize the experimental procedure. Each measurement is operated and monitored with the computer control unit using different commercial software. The drop generator and the heating system are controlled by *National Instruments LabView*, while the observation system is operated by *Vision Research PCC*.

After the measurements, the raw data is converted into image files and subsequently post-processed by *Mathworks Matlab*. Further information about the post-processing can be found in section 2.2.1. Finally, all measured data are recorded and stored onto a RAID-storage system within the computer.

2.2 Measurement techniques for drop characterization

Characterization of the size and velocity of the impinging drop or its secondary spray are important quantities for the present study. For this reason, the implementation of an accurate drop characterization method is essential. Several measurement techniques can be used for this. In the following sections a description of the applied drop measurement techniques are given. The applied techniques can be divided into image-based drop measurement techniques for drops captured by the high-speed camera and into phase Doppler measurement techniques based on interferometry of small spherical particles.

2.2.1 Image based drop characterization

Whenever a drop is captured by the high speed video system, the drop characteristics can be obtained via direct imaging. A well-known and quite simple measurement technique is shadowgraphy imaging (Tropea, 2011). With this technique a homogeneous light source is placed in the background. Hence, the drop is illuminated from behind and a shadow appears on the image due to the drop. If the drop is well focused by the camera, the boundary between the bright background and the shadow of the drop is sharp, which allows a precise detection of the drop. Thus, the drop characteristics can be measured from the obtained images using an image processing algorithm.

Nonetheless, image based drop characterization is limited by some phenomena, which have to be taken into account for a precise analysis, *i.e.* resolving capacity, depth of field and motion blur. The following sections provide a detailed description of the different phenomena and conclude with a brief description about the image processing algorithm.

Resolving capacity

The minimum distance between two points that can still be distinguished from an optical system is known as the resolving capacity. This phenomenon is caused by Frauenhofer diffraction of light passing through a small circular aperture. It describes the physical resolution limit of an objective lens (Hecht, 1998; Pedrotti et al., 2007).

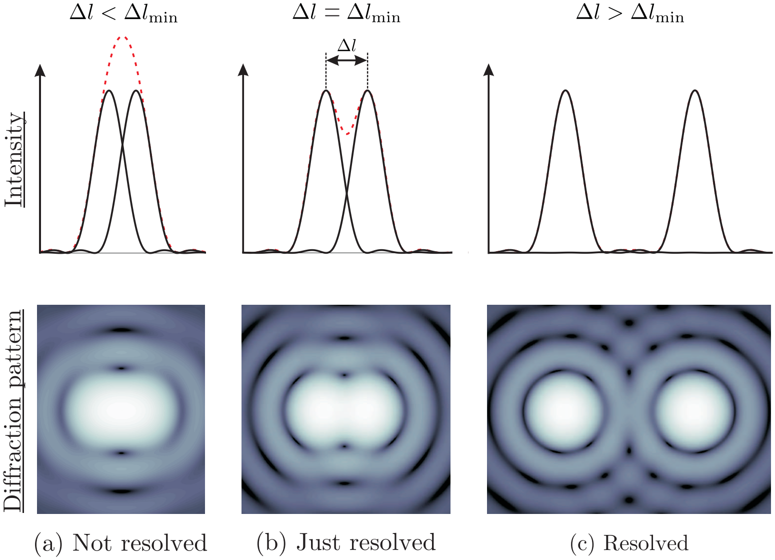

(a) Not resolved (b) Just resolved (c) Resolved

Figure 2.4: Airy pattern of two point sources at different distances: (a) both points are closer than the resolving capacity, (b) both points are equal to the resolving capacity and (c) both points are further away than the resolving capacity.

Due to light diffraction at the lens aperture, a point source is not projected as a point but rather as a diffraction pattern onto the projection screen (camera sensor). This pattern is known as Airy pattern and its central maximum intensity spot is called the Airy disk. Considering the Rayleigh criterion, two point sources at a small distance Δl can just be resolved as two separate points, if the center of one Airy disk is located at the first minimum of the second Airy disk (Hecht, 1998). It thus defines the resolving capacity Δl_{min}. The criterion is exemplary shown in Fig. 2.4. For instance, in case (a) the two points cannot be resolved since the distance $\Delta l < \Delta l_{\mathrm{min}}$ is too close, while in case (c) both points are clearly distinguishable. The resolving capacity Δl_{min} strongly depends on the focal length and the aperture diameter and can be calculated for an objective lens according to Pedrotti et al. (2007):

$$\Delta l_{\mathrm{min}} = 1.22 \, \frac{\lambda_1 \, f}{d_L} = 1.22 \, \lambda_1 \, k, \tag{2.2}$$

where λ_1 is the wavelength of the light, f is the focal length, d_L is the diameter of the aperture and $k = f/d_L$ is the f-number of the lens.

Consequently, smaller structures than the resolving capacity cannot be resolved with direct imaging methods. Furthermore, a higher camera resolution (at constant physical sensor size) would not lead to a better spatial resolution if the pixel size of the sensor is already the size of the resolving capacity (Opfer, 2014). For the optical system used in the present thesis, the resolving capacity yields $\Delta l_{\mathrm{min}} = 12.1\,\mu\mathrm{m}$ with an effective f-number of $k = 22$. This is close to the applied spatial resolution shown in section 2.1 and indicates an ideal alignment of the observation system.

Depth of field

The depth of field is an another important parameter for image based drop characterization. It strongly depends on the aperture of the optical system, *e.g.* focal length and f-number. To illustrate the depth of field (DOF), a ray diagram for a symmetrical thin lens is exemplary shown in Fig. 2.5. Points within the focal plane are projected as points onto the imaging plane (camera sensor). If a point is out of the focal plane it is not longer imaged as a clear point but rather as a blur spot, also known as the circle of confusion. The diameter of the circle increases with larger distance to the focal plane. Hence, the depth of field describes the maximum distance from which a point is still captured with an acceptable blur onto the camera sensor. This acceptable value strongly depends on the structure of the camera sensor.

Considering c as the acceptable circle of confusion, the near point a_n and the far point a_f of the depth of field can be thus calculated from the thin lens equation (Pedrotti et al., 2007):

$$a_n = \frac{a_0 f^2}{f^2 + k\,c\,(a_0 - f)}, \tag{2.3}$$

$$a_f = \frac{a_0 f^2}{f^2 - k\,c\,(a_0 - f)}, \tag{2.4}$$

where f is the focal length and k is the f-number. Consequently, the depth of field can be calculated using Eq. (2.3) and Eq. (2.4):

$$\mathrm{DOF} = a_f - a_n = 2\frac{a_0 f^2\,(a_0 + f)\,k\,c}{k^2 c^2\,(a_0 + f)^2 - f^4}. \tag{2.5}$$

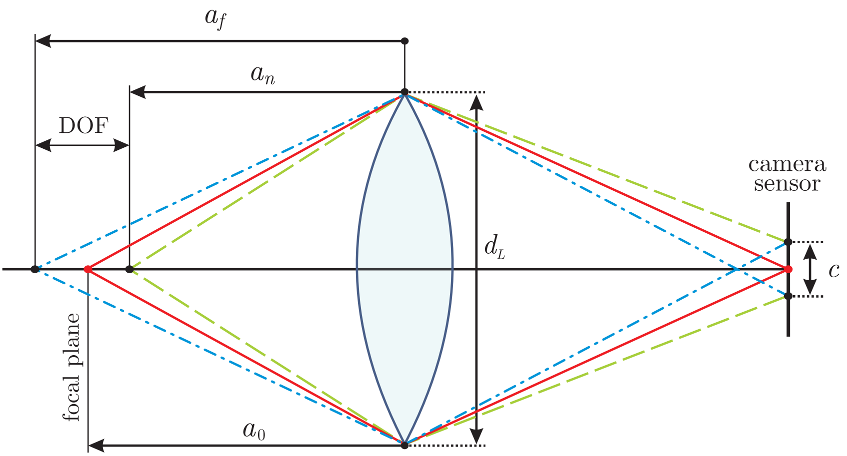

Figure 2.5: Ray diamgram for illustration of the depth of field (DOF) for a symmetrical thin lens. Adapted from Pedrotti et al. (2007).

With the help of the hyperfocal distance

$$a_H \approx \frac{f^2}{k\,c} \quad \text{for} \quad a_0 < a_H, \tag{2.6}$$

the depth of field DOF can be approximated to

$$\mathrm{DOF} \approx 2\frac{a_0^2 a_H}{a_H^2 - a_0^2}, \quad \text{for} \quad a_0 < a_H. \tag{2.7}$$

The hyperfocal distance is the distance beyond which all objects are be brought into focus with a given lens system. From Eq. (2.6) and Eq. (2.7) it can be seen, that the depth of field increases for larger f-number and smaller focal lengths.

The estimation of the depth of field for a system of lenses is rather complicated due to various parameters (Pedrotti et al., 2007), therefore in the present thesis it is determined experimentally using a DOF-Target (*Edmund optics DOF 5-15*). An image of the target is shown in Fig. 2.6(a). The surface of the target is tilted by 45° and consists of horizontal and vertical calibrated lines. By determining the intensity profile along the line pairs (exemplary marked as red line in the image), the depth of field can be easily estimated.

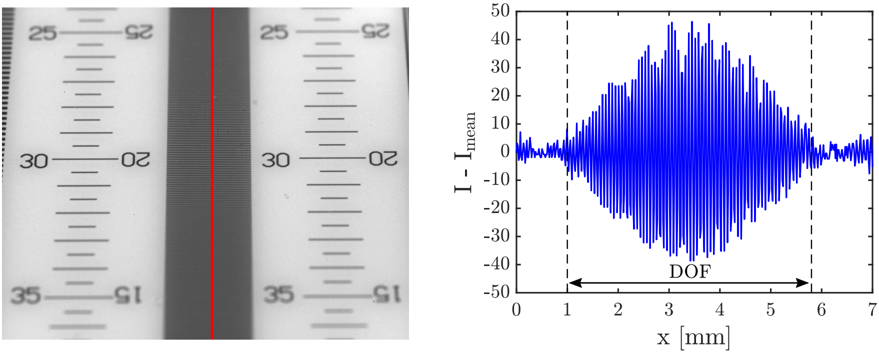

(a)

(b)

Figure 2.6: (a) DOF target for the experimental determination of the depth of field. (b) Analysis of the depth of field: Intensity profile of the line pairs along the red line.

In Fig. 2.6(b) the intensity profile along the red line is shown. The analysis yields a depth of field of DOF ≈ 4.8 mm. Since the drop diameter is in the order of two millimeters, the estimated depth of field is large enough for the present study.

Motion blur

Beside the resolving capacity and the depth of field, motion blur has to be taken into account in direct imaging methods. This is essential as long as fast objects have to be captured. Due to motion blur, objects seem to be out of focus even if they are within the depth of field. The reason for this phenomenon is the motion of the objects during the exposure time.

Even if a picture seems to be a snapshot of one infinitesimally small moment, it is captured over a finite amount of time. This time is known as exposure time, in which the incident light is temporally and spatially integrated for each pixel (Favaro & Soatto, 2007). Consequently, the motion of an object is also captured, which results in a blurred image of the moving object. For instance, if the exposure time is chosen too long, a moving light spot will be captured as a pathline.

Motion blur can be reduced by decreasing the exposure time of the camera. A further way to reduce motion blur is to lower the illumination time of the light source, *e.g.* with a pulsed light source. With the spatial resolution δx_{px} of one pixel and the maximal velocity $U_{\max}$ of the object, an upper bound for the exposure time can be estimated to prevent motion blur:

$$\delta t_{\mathrm{e}} = \frac{\delta x_{\mathrm{px}}}{U_{\max}}, \tag{2.8}$$

In the present thesis the upper bound for the exposure time to prevent motion blur yields $\delta t_{\mathrm{e}} = 5.1\,\mu\mathrm{s}$ for a maximum velocity $U_{\max} = 2.5\,\mathrm{m/s}$. Therefore a continuous light source is chosen for the main experiments, since the exposure time of the camera can be set up to one microsecond. If a much smaller exposure time was required, *e.g.* for the fast secondary spray, a short pulsed laser (*Cavilux HF*) with a wavelength of $\lambda_1 = 640\,\mathrm{nm}$ has been used as light source instead.

Image post-processing

To obtain the effective diameter and velocity of the impinging drop for each measurement, post-processing has been performed using a numerical computing environment (*MathWorks Matlab*). In Fig. 2.7 the input and the outcome of the image post-processing algorithm is exemplary shown. After the raw video files have been converted into image files, the gray scale images are processed with a developed image processing algorithm, which automatically detects and tracks the drop during impact. This is done by background subtraction and by conversion of the grayscale image into a binary image, based on a threshold. The threshold is globally determined according to a method described by Otsu (1979). Due to some processing errors, small artifacts may occur in the converted image, therefore an automatic detection and elimination procedure has been implemented in the algorithm. In the end, the shape of the drop can be easily detected from the filtered binarized image.

Based on the number of the pixel within the detected drop area A_d, an equivalent diameter of the drop $D_0 = \sqrt{4\,A_d/\pi}$ is calculated in each image. By tracking the centroid of the drop, the impact velocity has been obtained by using the time of flight method. Finally, for the full impact all measured values are averaged and the standard deviation is calculated.

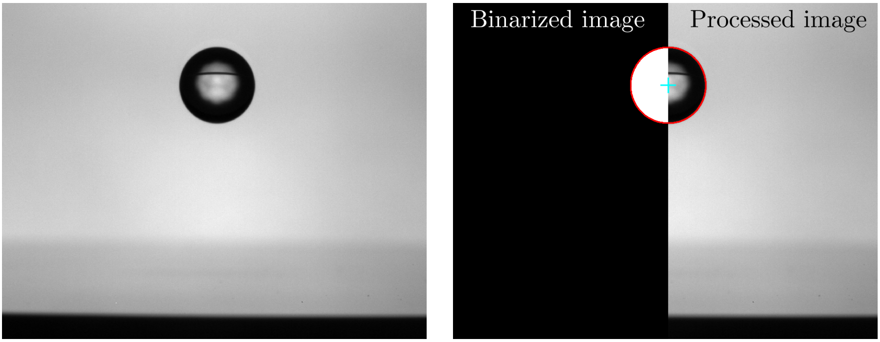

(a) (b)

Figure 2.7: (a) Input of the image post-processing algorithm: raw image. (b) Outcome of the image post-processing algorithm: binarized and processed image. The centeroid is marked with a cross, while the boundary of the drop and the backround is painted in red. By tracking the centeroid the drop velocity has been obtained.

To achieve more information about the accuracy of the drop detection algorithm and its maximum level of drop sizing error, a calibration measurement with a camera test target (*Edmund optics*) has been performed. It features a highly accurate dot pattern with different dot diameters. By changing the position of the target stepwise within the depth of field, the dots become slightly blurred and the absolute error of the drop detection algorithm can be easily determined. The results are shown in Fig. 2.8 for various particle sizes and distances from the focal plane. It is obvious that within the depth of field (±3 mm) the uncertainty of the drop size measurement is less than ±50 μm, which indicates a reliable post-processing algorithm.

2.2.2 Phase Doppler technique

For spherical drops much smaller compared to the initial drop, *e.g.* caused by secondary atomization, phase Doppler measurements have been conducted. Image based drop characterization is not applicable for such small drops, due to the limited resolving capacity of the image based measurement technique, as shown in section 2.2.1.

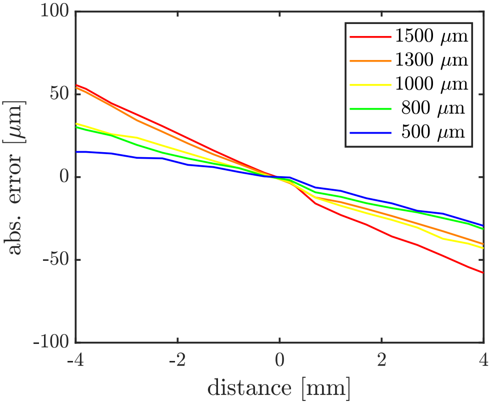

Figure 2.8: Absolute drop sizing error of the drop detection algortihm for various positions from the focal plane. The calibration measurement has been performed with a special test target.

The phase Doppler measurement technique is an extension of the laser Doppler measurement technique, allowing particle size measurements in addition to velocity measurements with a very high spatial and temporal resolution. It is based on light scattering of small spherical particles, which pass through a measurement volume formed by two intersecting laser beams (Albrecht et al., 2013). Within the intersecting area of the two beams, a fringe pattern is formed by positive and negative interference of the light waves. If a particle is passing the fringe pattern the scattered light is proportional to the local light intensity.

In Fig. 2.9 the basic configuration of the standard phase Doppler system is exemplary shown. Since the phase Doppler measurement technique comprises also the measurement principle for laser Doppler, the velocity of the particle u_p passing through the fringe pattern along the x-direction is obtained from the Doppler frequency f_D from one of the detector signals (Albrecht et al., 2013):

$$u_p = \frac{\lambda_1}{2\sin{}^{\theta}\!/_{2}} f_\mathrm{D}. \tag{2.9}$$

Here λ_1 is the wavelength of the laser beams and θ is the beam intersection angle of the transmitting optics.

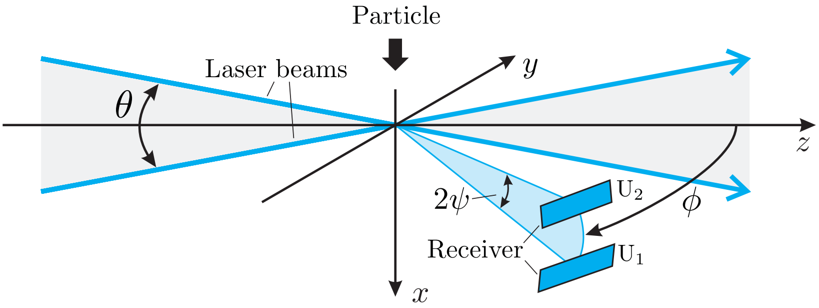

Figure 2.9: Scheme of the standard phase Doppler measurement technique: each particle passing through the measurement volume formed by two intersecting laser beams scatters light, which will be detected by the detector U_1 and U_2 of the receiver. Adapted from Albrecht et al. (2013).

If first-order refraction is the dominant scattering order, the drop diameter of the particle d_p can be calculated from the phase difference $\Delta\Phi_{12}$ of the two detector signals according to Tropea (2011):

$$\Delta\Phi_{12} \approx -\frac{4\pi}{\lambda_1} d_p \frac{n_r \sin\psi\,\cos{}^{\theta}\!/_{2}}{k_\Phi\sqrt{1+n_r^2-n_r k_\Phi}}, \qquad k_\Phi = \sqrt{2+\cos\psi\,\cos\phi\,\cos{}^{\theta}\!/_{2}}. \quad (2.10)$$

Here n_r is the relative refractive index, while ψ and ϕ are the elevation and off-axis angle of the receiving probe. Consequently, the relevant drop characteristics (velocity and size) can be estimated from the received detector signals, according to Eqs. (2.9) and (2.10). A more detailed description of the phase Doppler measurement technique is given in Tropea (2011) and Albrecht et al. (2013).

In the present thesis a dual-mode phase Doppler measurement system is used. The dual-mode configuration provides the data of the diameter and two components of the velocity vector simultaneously. In addition to the standard configuration shown in Fig. 2.9, a second set of laser beams and detectors is used. It is placed in the yz-plane and known as planar phase Doppler configuration. With the combination of a standard and planar phase Doppler system (therefore called dual-mode configuration), it is also possible to validate the sphericity of the particles, which further increases the accuracy of measurement (Tropea et al., 1996).

Table 2.2: Optical parameters of the dual-mode phase Doppler system used in the present thesis for the characterization of fine secondary droplets.

Parameter	Value
Laser system	DPSS laser
Laser power	80 mW
Beam spacing	60 mm
Transmitter focal length	500 mm
Wavelength 1	$\lambda_1 = 532\,\text{nm}$
Wavelength 2	$\lambda_2 = 561\,\text{nm}$
Frequency shift	80 MHz
Fringe direction	U-/V+
Refractive index water	1.33
Receiver focal length	500 mm
Mask	A
Slit	100 μm
Scattering angle	29°
Maximum phase	260°
Phase ratio validation	15 %

The used phase Doppler system has been equipped with a *DANTEC* Flow Explorer with two 300 mW DPSS lasers at wavelengths of $\lambda_1 = 532\,\text{nm}$ and $\lambda_2 = 561\,\text{nm}$ to measure two velocity components (axial u_x and tangential u_y) of the secondary droplets. As receiving optics a 112 mm dual-PDA receiver is used. The systems is carefully aligned to achieve high validation rates and reliable results. An overview of the optical parameters of the system are shown in Table 2.2.

With the given optical parameters of the laser system a maximum drop diameter of $d_{\text{max}} \approx 120\,\mu\text{m}$ can be measured. The data acquisition of the dual-mode phase Doppler measurement system operates in cyclic mode to repeat several drop impacts in sequence. It is repeatedly triggered by a laser light barrier which detects the falling drop. All phase Doppler measurements are accompanied by the simultaneous observations of the high-speed video system, which allows to associate the phase Doppler data with the observed phenomena.

3 Regimes of drop impact at different substrate temperatures

In the present chapter the various regimes of drop impact at different substrate temperatures are shown. Section 3.1 provides the main observations of the non-isothermal drop experiments. A qualitative description of the observed microscopic thermodynamic and hydrodynamic phenomena is given. Section 3.2 shows a quantitative regime classification in terms of a regime map for different substrate temperatures and impact conditions. Parts of the following sections have been published in Breitenbach et al. (2017a,b, 2018a,b) and in Roisman et al. (2018). Furthermore, parts of the experimental investigations have been described in the theses of Kissing (2017) and v. Kieckebusch (2018).

3.1 Observations of non-isothermal drop impact

Outcomes of the drop impact onto a hot substrate are accompanied by thermal effects. Hence, the observations of the non-isothermal drop impact lead to a qualitative classification into various thermodynamic phenomena (thermodynamic perspective) and impact outcomes regimes (hydrodynamic perspective). In the following sections a description of the phenomena are given:

Microscopic thermodynamic phenomena

The thermodynamic phenomena during drop impingement can be categorized into the commonly known boiling regimes. Figure 3.1 pictures various microscopic boiling regimes which have been observed in the experiments: (a) single phase cooling, (b) nucleate boiling, (c) transition boiling, and (e) film boiling. The same phenomena have been observed before (Bernardin et al., 1997). Recent observations from the present thesis added also the thermal atomization regime, depicted in Fig. 3.1(d).

Single phase cooling occurs if the drop impact is not accompanied by boiling. No bubbles can be observed within the drop due to phase change at the solid/liquid interface and the drop vaporizes slowly on its liquid/gas interface and three-phase contact line (Batzdorf, 2016). The heat transfer at the solid/liquid interface is limited due to convection. This behavior is observed until some critical value $\Delta T_{\mathrm{w}} \lesssim 5\,^{\circ}\mathrm{C}$ lying slightly above the saturation temperature T_{sat}, where $\Delta T_{\mathrm{w}} = T_{\mathrm{w0}} - T_{\mathrm{sat}}$ is the superheated wall temperature. Up to this critical value the substrate temperature is insufficient to initiate bubble, therefore the fluid flow and heat transfer are mainly influenced by the change of the material properties of the liquid and of the wall. Consequently, the physical mechanisms determining the outcome of drop impact in the single phase cooling regime are the same as for drop impact under isothermal conditions, *e.g.* at normal room temperature.

At higher surface temperatures the drop impact is accompanied by boiling and the flow within the drop can be significantly influenced by the phenomena related to boiling near the wall. For temperatures $\Delta T_{\mathrm{w}} \gtrsim 5\,^{\circ}\mathrm{C}$ slightly exceeding the saturation temperature, evaporation is mainly caused by nucleate boiling. During nucleate boiling an array of small growing bubbles appears on the substrate as a result of heterogeneous nucleation. Due to some delay time (waiting time), during drop spreading some superheating of the liquid occurs before the bubbles emerge onto the heated substrate surface (Carey, 1992).

The bubbles are characterized by a growth rate and by the residence time before they collapse. They detach from the substrate surface, ascend through the drop and possibly coalesce with other bubbles. When the bubbles break through the liquid/gas interface they collapse and fine secondary droplets are produced.

A particular case of nucleate boiling is foaming. This has been observed only for water drops within a limited temperature range. It is exemplary shown in Fig. 3.2. In the foaming phenomena the vapor bubbles grow much larger, no coalescence and no separation from the liquid/gas interface is observed. In this subcategory of nucleate boiling, the entire drop starts to foam and seems to inflate, c.f. Fig. 3.2 (d)-(g) . This phenomenon is not yet fully understood (Craig et al., 1993). An explanation is that small amounts of dissolved ionic salt in the double distilled water prevent bubble coalescence due to electrostatic effects and changes of surface tension. The influence of

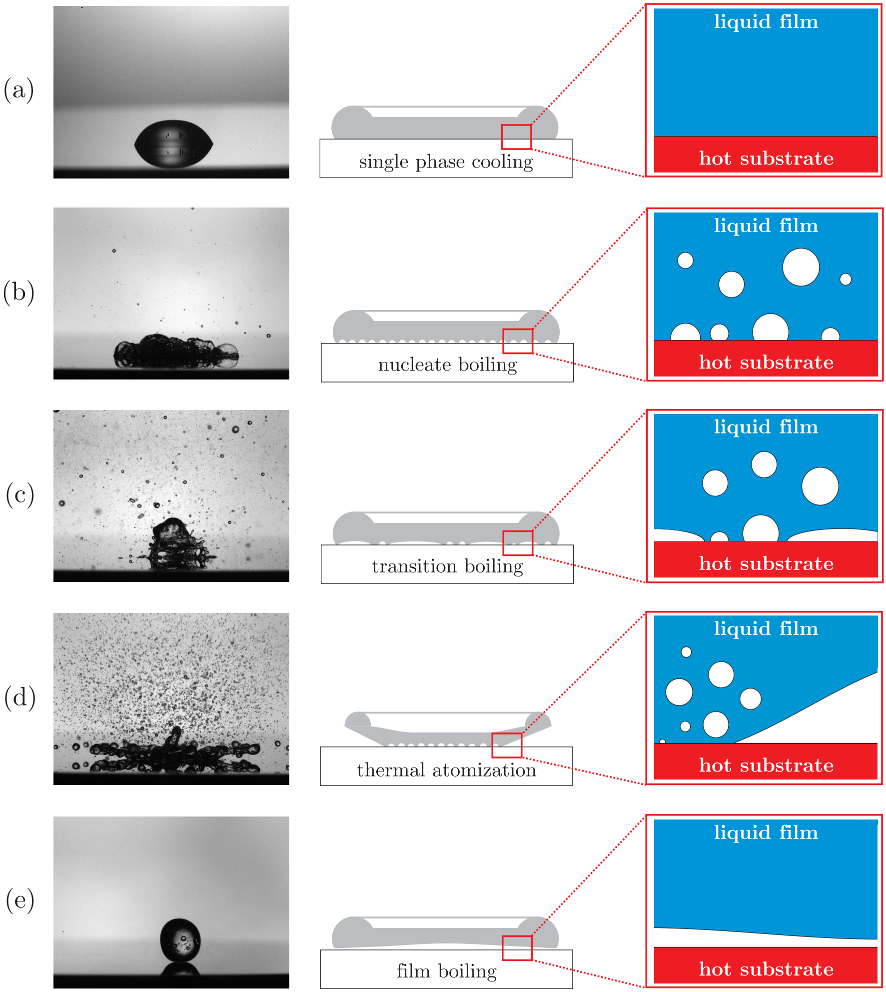

Figure 3.1: Microscopic thermodynamic boiling phenomena: (a) single phase cooling, (b) nucleate boiling, (c) transition boiling, (d) thermal atomization and (e) film boiling.

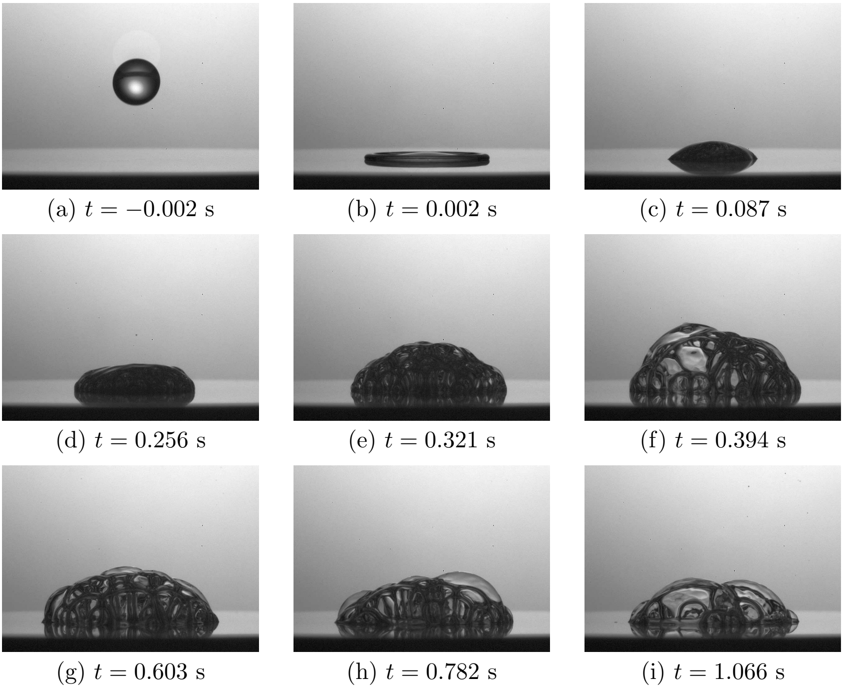
(a) $t = -0.002$ s (b) $t = 0.002$ s (c) $t = 0.087$ s

(d) $t = 0.256$ s (e) $t = 0.321$ s (f) $t = 0.394$ s

(g) $t = 0.603$ s (h) $t = 0.782$ s (i) $t = 1.066$ s

Figure 3.2: Foaming phenomena for different time instants: drop impact with initial substrate temperature $T_{\mathrm{w}0} = 115\,^{\circ}\mathrm{C}$, drop diameter $D_0 = 2.2\,\mathrm{mm}$ and impact velocity $U_0 = 1.3\,\mathrm{m/s}$.

the dissolved ionic salt on boiling water drops was shown in Cui et al. (2003). The presence of electrical charge on the bubble surface due to ionic salts produces a repulsive force, preventing the bubbles from approaching each other (Keitel & Onken, 1982). Some theories also claim that during boiling the dissolved salt cannot diffuse quickly enough and the local salt concentration in the thinning liquid layer increases; therefore the surface tension increases, the coalescence of the bubbles is delayed and the water drop foams (Marrucci, 1969).

Transition boiling is an intermediate regime between nucleate and film boiling. It is observed for surface temperatures higher than $\Delta T_{\mathrm{w}} \gtrsim 50\,^{\circ}\mathrm{C}$. The vapor bubble generation rate rises quickly, caused by the high wall tem-

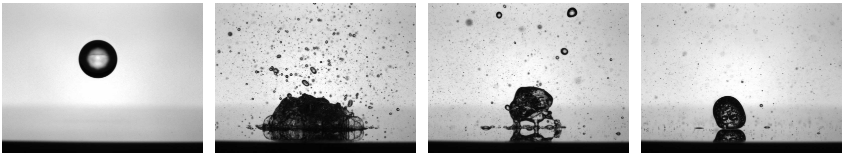

(a) $t = -2.0$ ms (b) $t = 9.8$ ms (c) $t = 59.2$ ms (d) $t = 116.4$ ms

Figure 3.3: Transient phenomena: drop impact with initial substrate temperature $T_{\mathrm{w0}} = 160\,^{\circ}\mathrm{C}$, drop diameter $D_0 = 2.2\,\mathrm{mm}$ and impact velocity $U_0 = 1.5\,\mathrm{m/s}$.

perature. Consequently, bubbles coalesce and form a vapor layer over some portions of the area between the drop and the surface, while the rest of the drop wets the surface. The transition regime is very unstable and liquid layers frequently collapse with the generation of secondary droplets. The drop appears to be dancing on the surface.

Thermal atomization is a particular case of transition boiling. It occurs for higher substrate temperatures and only during drop impact. During thermal atomization a central part of the drop lamella is in contact with the substrate. Within this central part bubbles appear at the solid/liquid interface. But the peripheral part of the lamella levitates in a fast vapor stream ejected near the contact line leading to the dewetting of the substrate. A more detailed description of the phenomena related with thermal atomization is given in section 5.2.

By further increasing the surface temperature to the Leidenfrost point the heat flux transferred to the water drop reduces (Quéré, 2013), since the water vapor is ineffective for heat conduction. After reaching the Leidenfrost temperature, film boiling occurs. At this condition the substrate surface is covered with a full vapor layer and the drop does not wet the surface anywhere; heat flux and friction between the drop and the surface decrease. The pressure induced in the vapor layer by the flow suspends the impacting drop above the surface (Leidenfrost, 1966). As a consequence, the drop lifetime (time until the complete drop is evaporated) increases significantly for a sessile drop. As already discussed in section 1.2.2, the Leidenfrost temperature of an impinging drop (compared to a sessile drop) is not a constant, but rather a dynamic value known as the dynamic Leidenfrost temperature which is strongly influenced by the impact velocity (Rein, 2002).

Noteworthy is the fact, that the entire boiling process is transient and not only controlled by the initial substrate temperature T_{w0}. The boiling modes of a single drop can switch during drop evaporation due to the change of drop size, liquid properties or surface temperature. This phenomenon is exemplary shown in Fig. 3.3. It is obvious that after the drop impact different boiling phenomena occur: after an initial nucleate boiling stage (b) the drop starts to switch to transition boiling (c), while after a significant drop mass loss due to secondary atomization, the drop is in the film boiling stage (d) and it is not longer in contact with the hot substrate.

Impact outcome regimes

The observations of the drop impact allow to classify various impact outcome regimes (hydrodynamic perspective). In Fig. 3.4 the major thermally induced hydrodynamic impact outcomes observed in the experiments are shown: (a) drop deposition, (b) drop dancing, (c) thermal atomization, and (d) drop rebound. Some of the impact regimes are commonly known and have been identified in various previous studies (Bernardin et al., 1997; Staat et al., 2015; Bertola, 2015).

In the drop deposition regime no rebound or breakup is observed; the drop completely wets the surface over the whole impact process and the entire drop lifetime. After the drop impact the drop starts to evaporate and the heat transfer at the solid/liquid interface is mainly associated with convection or nucleation, depending on the initial substrate temperature. Therefore, this impact regime corresponds to single phase cooling and nucleate boiling heat transfer phenomena.

The drop dancing regime is mainly characterized by instantaneous transition boiling. It is a transient regime with less heat transfer rates compared to the drop deposition regime (accompanied by nucleate boiling). After an initial splash the drop seems to dance on the hot substrate, explained by the numerous vapor bubbles and liquid layers frequently growing and collapsing. Due to high initial substrate temperatures, the bubbles appear within the spreading drop at the solid/liquid interface a short time after the first instant of contact. In this regime the liquid near the substrate is initially superheated and bubbles appear at the interface after a certain waiting time t_{w} (Carey, 1992). In the present experiments the waiting time $t_{\mathrm{w}} < 100\,\mu\mathrm{s}$

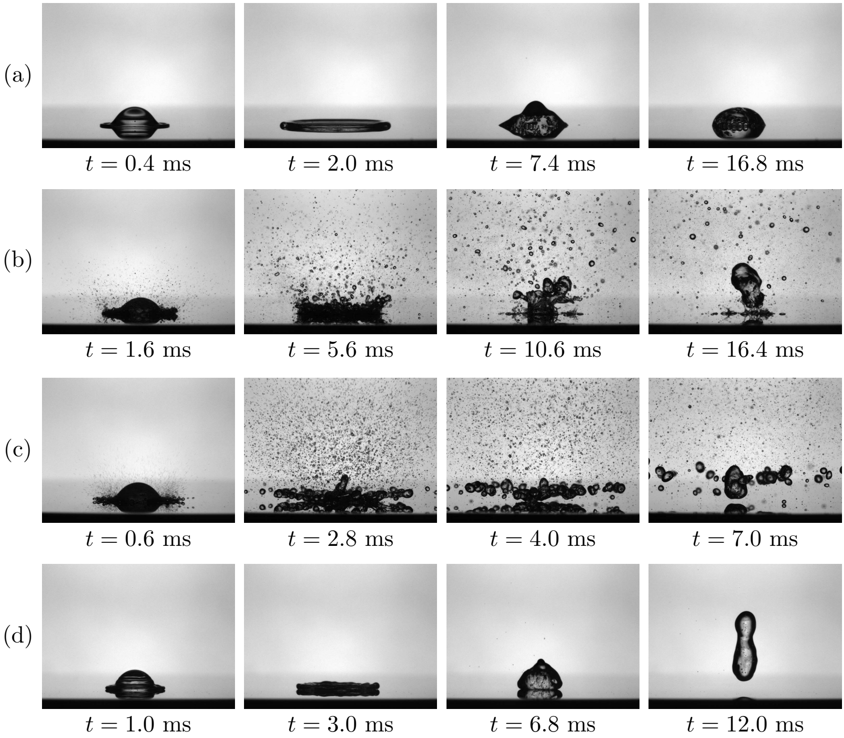

$t = 0.4$ ms $t = 2.0$ ms $t = 7.4$ ms $t = 16.8$ ms

$t = 1.6$ ms $t = 5.6$ ms $t = 10.6$ ms $t = 16.4$ ms

$t = 0.6$ ms $t = 2.8$ ms $t = 4.0$ ms $t = 7.0$ ms

$t = 1.0$ ms $t = 3.0$ ms $t = 6.8$ ms $t = 12.0$ ms

Figure 3.4: Major thermally induced hydrodynamic impact outcomes of the non-iosthermal drop impact, which have been observed in the experiments: (a) drop deposition ($T_{\mathrm{w0}} = 120\,^\circ\mathrm{C}$, $D_0 = 2.2$ mm, $U_0 = 1.5$ m/s), (b) drop dancing ($T_{\mathrm{w0}} = 170\,^\circ\mathrm{C}$, $D_0 = 2.2$ mm, $U_0 = 0.7$ m/s), (c) thermal atomization ($T_{\mathrm{w0}} = 260\,^\circ\mathrm{C}$, $D_0 = 2.2$ mm, $U_0 = 1.7$ m/s), and (d) drop rebound ($T_{\mathrm{w0}} = 280\,^\circ\mathrm{C}$, $D_0 = 2.2$ mm, $U_0 = 1.5$ m/s). (Reprinted from Breitenbach et al. (2018b), with permission of Springer Nature. © 2018 Springer Nature.)

is very short and consequently much shorter than the typical time of drop spreading. Accompanying the vapor bubbles are numerous massive secondary droplets, generated when the bubbles burst through the liquid/gas interface above the drop. After a significant drop mass loss due to evaporation and generation of secondary droplets, the residual liquid mass often recoils.

Thermal atomization regime is related to the corresponding boiling regime. It is described by thermally induced dewetting of the substrate, which is characterized by intensive lamella evaporation, initiation of lamella levitation, and finally drop disintegration. An intensive vapor flow leads to a generation of a fast vertical spray of fine droplets induced by the lamella evaporation and a number of larger drops formed as a result of the drop disintegration and rim breakup. The drop disintegration is due to instabilities in the lamella leading to the emerge of expanding holes. Both processes take place in a very short time period, mainly within the first few milliseconds after initial contact of the impinging drop with the hot impact substrate. The duration of contact, the contact time, of the impinging drop before rebound and complete disintegration is determined by the time of the thermal dewetting. Therefore the regime is called thermal atomization. Inertia induced drop breakup (Lv et al., 2016; Tsai et al., 2009) is not considered as thermal atomization in this study.

The drop rebound regime is mainly associated with the film boiling phenomena. In this regime the entire drop bounces after the spreading and receding phase of the drop; this phenomenon is caused by a vapor layer between the drop and hot substrate. The vapor layer reduces energy dissipation (dissipated by viscous effects) during drop spreading onto the hot substrate, so that in the end there is still some kinetic energy left for bouncing (Biance et al., 2006; Bertola, 2015). Furthermore, another mechanism is the formation of high pressures within the thin vapor layer gap, which cause a force onto the impinging drop (Rein, 2002).

Even so, drop rebound can also be observed in addition with secondary droplets. In such case additionally bubbles within the drop are clearly visible. This phenomena is caused by some partial wetting of the drop with the hot substrate during drop spreading or receding. In this advance stage of transition boiling phenomena the vapor layer is not yet fully developed during drop impact. Since fine secondary drops arise from the drop lamella and rim, this type of rebound is called wet rebound. By definition the wet rebound has

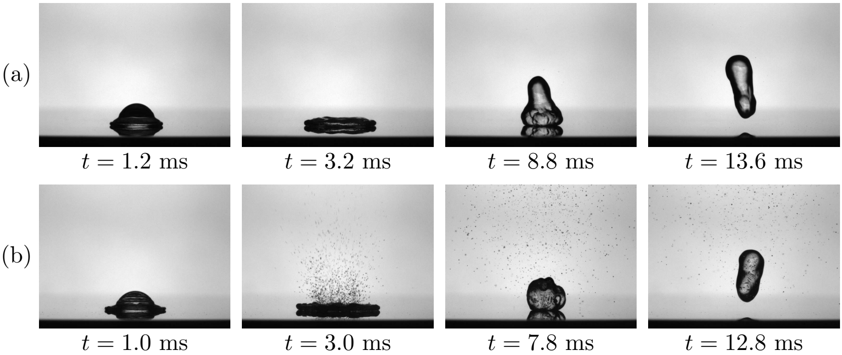

Figure 3.5: (a) Dry rebound without secondary droplets in comparison to (b) wet rebound with secondary droplets. The parameters are (a) $T_{\mathrm{w0}} = 320\,^\circ\mathrm{C}$, $D_0 = 2.2$ mm, $U_0 = 0.7$ m/s and (b) $T_{\mathrm{w0}} = 220\,^\circ\mathrm{C}$, $D_0 = 2.2$ mm, $U_0 = 0.7$ m/s.

to be related to the transition boiling phenomena (since some partial contact occurs), while the dry rebound is related to the film boiling phenomena. This an important fact, since in literature film boiling is often characterized only by drop rebound. The observation of a dry rebound and a wet rebound is exemplary shown in Fig. 3.5. It is obvious that in both cases the contact time of the drop with the hot substrate is relatively short and they are only slightly different. This indicates that the partial wetting has minor effects on the drop spreading and rebound dynamics.

3.2 Maps of drop impact outcomes

The observations of various impact regimes for different impact conditions lead to a quantitative classification into a map of drop impact outcomes, also known as impact regime map. In literature the maps of the different thermodynamic regimes or drop impact regimes are usually illustrated using the initial substrate temperature and the impact Weber number (Bernardin et al., 1997; Tran et al., 2012; Khavari et al., 2015; Bertola, 2015). However, the Weber number can only capture the isothermal, inertia dominated effects. Hence, the data in the present thesis has intentionally be left dimensioned, because it illustrates clearly that the impact outcomes are dependent both on hydrodynamic and thermodynamic quantities.

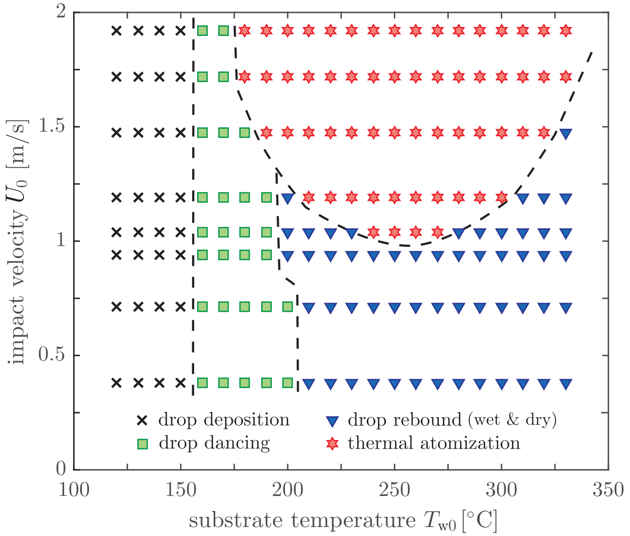

Figure 3.6: Map of drop impact outcomes for different impact velocities and initial substrate temperatures. The initial drop diameter is $D_0 = 2.2$ mm with a fluid temperature $T_{d0} \approx 25\,°\mathrm{C}$. (Reprinted from Breitenbach et al. (2018a). © 2018 Elsevier.)

An impact regime map for various impact velocities and substrate initial temperature is shown in Fig. 3.6. By changing the impact conditions the outcome significantly changes. It is important to mention, that no sharp boundary interface between the different impact regimes can be seen, but rather a diffuse interface due to stochastic effects of the experimental outcome. Consequently, the boundaries between the different impact regimes are essentially qualitative and should be interpreted in a probabilistic sense (Bertola, 2015).

For lower surface temperatures only drop deposition has been observed. The impact outcome switches to drop dancing if the initial substrate temperature increases, due to the change of the boiling phenomena from nucleate boiling to transition boiling. Based on this shift, the averaged heat flux from the hot substrate to the drop decreases and consequently the time until the whole drop is evaporated significantly increases.

If the substrate temperature gets closer to Leidenfrost conditions the portion of the vapor layer increases. At a certain point, this phenomenon leads to the rebound of the impinging drop (c.f. Fig. 3.6, transition from square □ → triangle ▽). As already indicated in the previous section, the drop rebound can be seen with as wet or dry rebound. For lower temperatures, only the wet rebound is observed. After reaching the Leidenfrost temperature the vapor layer is fully developed and a dry rebound occurs without any secondary droplet. The threshold between wet and dry rebound (which is the Leidenfrost point) is influenced by the impact velocity since the dynamic Leidenfrost temperature is velocity dependent (c.f. section 1.2.2)

A common correlation for the dynamic Leidenfrost temperature T_{dL} for different impact parameters can be found in literature (Yao & Cai, 1988; Rein, 2002; Bertola, 2015) in the form of

$$T_{\mathrm{dL}} = T_{\mathrm{sL}} + [C_1 \mathrm{We}^n] \ {}^\circ\mathrm{C}, \tag{3.1}$$

where T_{sL} is the static Leidenfrost temperature for a sessile drop in the film boiling regime, while C_1 and n are empirical coefficients determined by the experimental results. It becomes obvious, that for the limit $U_0 \to 0\,\mathrm{m/s}$ the value approaches to the static Leidenfrost temperature.

Figure 3.7 shows a map of the two different rebound outcomes in comparison with the correlation (3.1). The map is a detailed section of the drop rebound regime shown in Fig. 3.6. In the present thesis the dynamic Leidenfrost temperature can be found for $C_1 = 30$ and $n = 0.45$ with a static Leidenfrost temperature $T_{\mathrm{sL}} = 172\,^\circ\mathrm{C}$ for a water drop onto a polished aluminum substrate (Bernardin & Mudawar, 1999). The obtained coefficients are close to the values shown in Bertola & Sefiane (2005). Furthermore, the results indicate, that the impact velocity has almost a linear influence onto the dynamic Leidenfrost temperature.

Thermal atomization regime occurs only for high surface temperatures and fast impact velocities, as shown in Fig. 3.6. This leads to the assumption that due to the intensive lamella evaporation higher levels of heat transfer are needed for thermal atomization. The higher impact velocity leads to a thinner residual lamella (Roisman, 2009). The boundary between thermal atomization and drop rebound is not monotonic, but dependent in a more complex manner on the operation parameters. However, the present experiments indicate that if the impact velocity is high enough, part of the solid

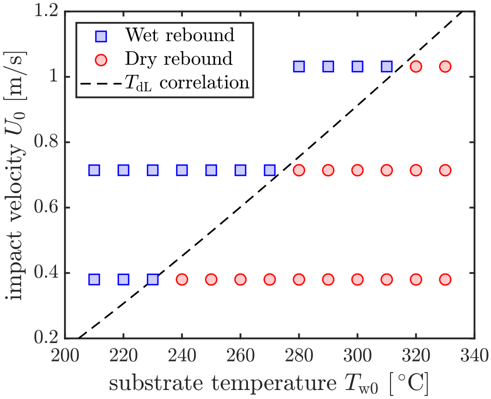

Figure 3.7: Map of rebound outcomes: dry rebound without secondary drops (film boiling) and wet rebound with secondary droplets (transition boiling) in comparison with the correlation (3.1). The map is a detailed section of the drop rebound regime shown in Fig. 3.6. The initial drop diameter is $D_0 = 2.2\,\mathrm{mm}$ with a fluid temperature $T_{d0} \approx 25\,^\circ\mathrm{C}$.

surface is wetted. This phenomenon leads to strong local overheating of the liquid and intensive evaporation at the contact line, fast irregular dewetting, breakup and levitation. It will be shown in the present thesis (c.f. section 5.2), that the Weber number is not relevant for the description of the threshold between thermal atomization and drop rebound. It becomes clear that the conventional school of using the Weber number of classifying outcomes of drop/wall interaction at elevated temperatures cannot be fundamentally correct. This assumption is supported by the fact that the Weber number does not account for thermal effects.

4 Drop impact without boiling

In the present chapter the non-isothermal drop impact not accompanied by boiling is investigated, *i.e.* drop impact in the single phase cooling regime. After a short motivation section 4.1.1 illustrates the main observations of the phenomena. Section 4.1.2 provides a theoretical model for the heat transfer during drop spreading and receding. Furthermore, in section 4.1.3 the heat transfer during simultaneous impact of two drops is calculated. Parts of the following sections have been published in Breitenbach et al. (2018b) and in Batzdorf et al. (2017). Furthermore, parts of the experimental investigations have been described in the thesis of v. Kieckebusch (2018).

4.1 Single phase cooling regime

Since drop impact in the single phase cooling regime is not accompanied by boiling the heat transfer rates between the drops and the wall are relatively low compared to regimes accompanied by boiling. For this very reason, drop impact and spray cooling without boiling is not in the main focus of the heat transfer literature in comparison to impact accompanied by boiling, *e.g* nucleate or film boiling. Nevertheless, drop impact in the single phase cooling regime is rather important for instance in cooling applications for high-performance computer chips (Tilton et al., 1994; Fabbri et al., 2005; Bar-Cohen et al., 2006). Already in the early nineties, chip cooling has been performed in a prototype of the SS-1 supercomputer (Ing et al., 1993) and it has been later used by default in the CRAY X-1 supercomputer (Kim, 2007).

As discussed in section 1.2.1, theoretical predictions in literature for heat transfer during drop impact in single phase cooling are often neglecting internal fluid motion since they are only based on heat conduction in the fluid. The main subject of the present section is the the introduction of a predictive theoretical model which accounts for the internal motion of the fluid. Furthermore, the model is extended for simultaneous impact of two drops.

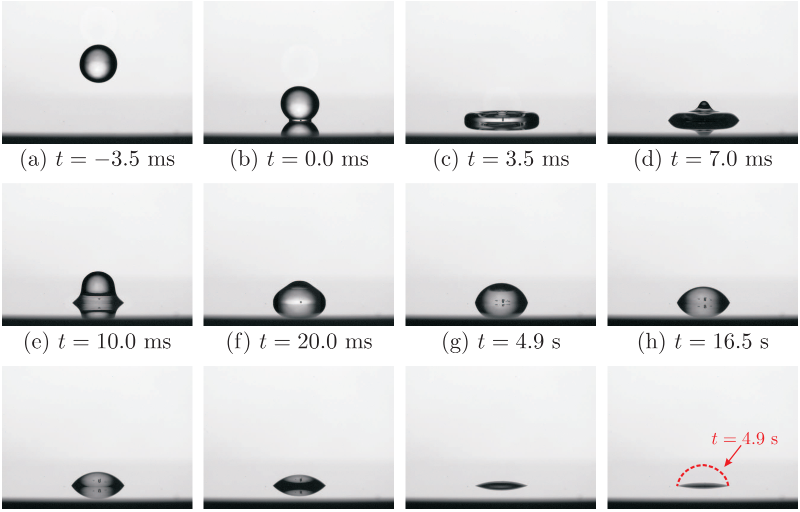

(a) $t = -3.5$ ms (b) $t = 0.0$ ms (c) $t = 3.5$ ms (d) $t = 7.0$ ms

(e) $t = 10.0$ ms (f) $t = 20.0$ ms (g) $t = 4.9$ s (h) $t = 16.5$ s

(i) $t = 24.3$ s (j) $t = 32.5$ s (k) $t = 47.8$ s (l) $t = 50.7$ s

Figure 4.1: Drop impact in the single phase cooling regime at different time instant: after spreading (c) and receding phase (d)-(f) the drop is in contact with the hot surface for a long time (g)-(l). In picture (l) the drop shape of time instant $t = 4.9\,\mathrm{s}$ is additionally shown as a dashed red line. The conditions are: initial fluid temperature $T_{d0} = 30\,^{\circ}\mathrm{C}$, substrate temperature $T_{\mathrm{w}0} = 85\,^{\circ}\mathrm{C}$, drop diameter $D_0 = 2.2\,\mathrm{mm}$ and impact velocity $U_0 = 0.6\,\mathrm{m/s}$.

4.1.1 Observations

The drop impact in the single phase cooling regime is exemplary shown in Fig. 4.1. After the spreading (c) and receding (d)-(f) the drop is in contact with the hot surface for a long time (g)-(l). During the whole evaporation process the contact area stays almost constant, thus the contact angle significantly decreases during evaporation. This is exemplary shown in Fig. 4.1(l) by the dashed red line, which represents the drop shape at the time instant $t = 4.9\,\mathrm{s}$. Since the substrate temperature in Fig. 4.1 is below to the saturation temperature $T_{\mathrm{w}0} < T_{\mathrm{sat}}$, the drop evaporates very slowly on its liquid/gas interface and contact line only due to diffusion into the gas atmosphere (Maxwell, 1877). This occurs when the gas atmosphere is unsaturated and until the water and gas will come to a thermodynamic equilibrium (Lewis, 1922).

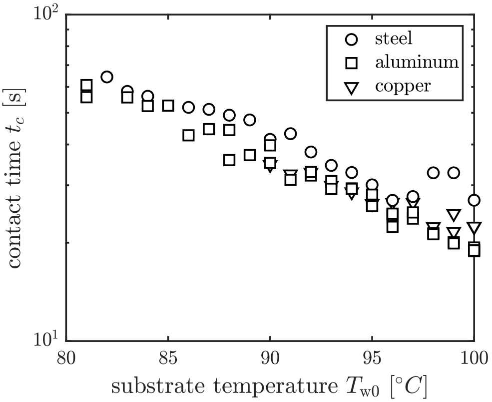

Figure 4.2: Drop contact for various substrate temperatures and materials. The initial fluid temperature $T_{d0} = 30\,^\circ\mathrm{C}$, drop diameter $D_0 = 2.2\,\mathrm{mm}$ and impact velocity $U_0 = 0.6\,\mathrm{m/s}$ are constant for all cases.

After a long time ($t \sim 10^2\,\mathrm{s}$) the drop has completely evaporated. Consequently, the required latent heat has been absorbed from the gas atmosphere but also from the hot substrate, even if the substrate temperature is below the boiling onset. Nonetheless, compared to evaporation due to boiling the complete evaporation process occurs over a long time period. The duration of contact (time until total drop evaporation) is shown in Fig. 4.2 for different substrate materials and temperatures. It can bee seen, that the drop contact time hardly differs for the various materials even if their thermal properties are significantly different. This can be explained by the evaporation mechanism since the time of evaporation is mainly controlled by the diffusion into the gas atmosphere. Therefore the flow and the properties of the surrounding gas atmosphere are of higher relevance compared to the thermal properties of the metal substrates.

During the drop spreading and receding process the heat transfer from the hot substrate to the drop is only governed by heat conduction in the wall and heat convection in the liquid. Directly at the moment of impact, a viscous boundary layer develops in the spreading drop. If the temperature of the substrate is different to the initial drop temperature, additionally a thermal boundary layer develops within the substrate and the liquid, leading to an equilibrium contact temperature on the solid/liquid interface. Since the

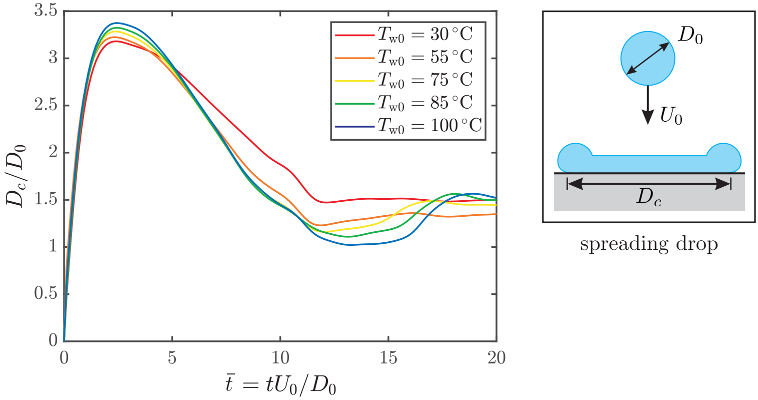

Figure 4.3: Dimensionless contact diameter for various initial substrate temperatures in the single phase cooling regime. The initial fluid temperature $T_{d0} = 25\,^\circ\mathrm{C}$, drop diameter $D_0 = 2.3\,\mathrm{mm}$, impact velocity $U_0 = 1.6\,\mathrm{m/s}$ are constant for all cases.

material properties depend on the temperature, the evaluation of the drop spreading radius is influenced by the change of the material properties of the liquid at the solid/liquid interface, *e.g.* viscosity and surface tension. Figure 4.3 shows the dimensionless contact diameter for various initial substrate temperatures. A definition of the contact diameter D_c, also known as spreading diameter, is shown in the right column. The initial fluid temperature $T_{d0} = 25\,^\circ\mathrm{C}$, drop diameter $D_0 = 2.3\,\mathrm{mm}$, and impact velocity $U_0 = 1.6\,\mathrm{m/s}$ are constant for all cases. It is obvious, that the maximum contact diameter increases for an increasing substrate temperature. Moreover, the drop leads to overshoot at the end of the receding phase. These phenomena can be explained by the decreasing fluid viscosity for higher substrate temperatures, leading to less energy dissipation by viscous effects during spreading.

4.1.2 Evaluation of heat transfer during drop impact

At the initial phase of drop spreading the temperature and the heat flux at the solid/liquid interface can be estimated considering the heat conduction in the substrate, heat convection in the spreading drop and the boundary conditions at the interfaces. In the absence of phase change at the interface these boundary conditions are described by the continuity of the temperature and of the heat flux in the solid and liquid regions at the interface.

The heat conduction in the solid substrate occurs in a thermal boundary layer. The thickness of the thermal boundary layer $\delta_\mathrm{w} \sim \sqrt{\alpha_\mathrm{w} t}$ increases in time, where α_w is the thermal diffusivity of the substrate material. In the liquid region the problem is determined by the viscous boundary layer of thickness $\delta_{\nu l} \sim \sqrt{\nu t}$ and the thermal boundary layer of thickness $\delta_l \sim \sqrt{\alpha_l t}$, which is influenced by the flow in the spreading drop. The flow compresses the thermal boundary layer in the liquid region, leading to an increase in heat flux in comparison to the case in a stagnant medium. Here ν and α_l are the kinematic viscosity and thermal diffusivity of the liquid drop material, respectively.

An exact solution of this problem has been obtained in Roisman (2009, 2010) by considering the mass balance, the axial momentum balance, and the energy balance equations for the fluid flow and heat transfer during drop impact onto the solid substrate. The expressions for the temperature distribution $T_\mathrm{w}(z,t)$ and for the heat flux $\dot{q}(z,t)$ within the solid substrate during the development of the thermal boundary layers are obtained for $z < 0$ in the form of

$$T_\mathrm{w}(z,t) = T_{\mathrm{w}0} + \frac{e_l (T_{d0} - T_{\mathrm{w}0})}{e_l + e_\mathrm{w} \mathscr{I}(\mathrm{Pr}_l)} \operatorname{erfc}\left[-\frac{z}{2\sqrt{\alpha_\mathrm{w}(t-t_0)}} \right], \tag{4.1}$$

$$\dot{q}(t) = -\lambda_\mathrm{w} \frac{\partial T}{\partial z} = \frac{e_l e_\mathrm{w} (T_{\mathrm{w}0} - T_{d0})}{\sqrt{\pi}[e_l + e_\mathrm{w} \mathscr{I}(\mathrm{Pr}_l)]\sqrt{t-t_0}} \exp\left[\frac{-z^2}{4\alpha_\mathrm{w}\,(t-t_0)} \right], \tag{4.2}$$

where t_0 is the inception instant of the thermal boundary layers, T_{d0} and $T_{\mathrm{w}0}$ are the initial temperatures of the drop and substrate, λ_w is the thermal conductivity of the wall, and $e_l = \lambda_l/\alpha_l^{0.5}$ and $e_\mathrm{w} = \lambda_\mathrm{w}/\alpha_\mathrm{w}^{0.5}$ are the thermal effusivities of the liquid and wall materials, respectively. The dimensionless function $\mathscr{I}(\mathrm{Pr}_l)$ is a function of the liquid Prandtl number $\mathrm{Pr}_l = \nu/\alpha_l$ which accounts for the influence of the fluid flow during drop spreading onto the heat transfer.

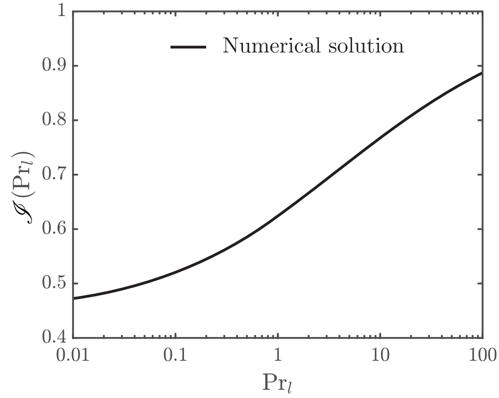

Figure 4.4: Function $\mathscr{I}(\mathrm{Pr}_l)$ for the liquid phase as a function of the Prandtl number, computed in Roisman (2010). Reprinted (adapted) with permission from Cambridge University Press.

The temperature at the liquid/solid interface $z = 0$, known as the contact temperature T_c, stays constant as long as the solutions (4.1) and (4.2) are valid. It can be evaluated by setting $z = 0$ in Eq. (4.1):

$$T_c = \frac{e_l T_{d0} + e_{\mathrm{w}} \mathscr{I}(\mathrm{Pr}_l) T_{\mathrm{w}0}}{e_l + e_{\mathrm{w}} \mathscr{I}(\mathrm{Pr}_l)}, \tag{4.3}$$

while the expression for the transferred heat flux at the liquid/solid interface is obtained from Eq. (4.2)

$$\dot{q}(t) = \frac{e_l e_{\mathrm{w}} \left(T_{\mathrm{w}0} - T_{d0}\right)}{\sqrt{\pi}\left[e_l + e_{\mathrm{w}} \mathscr{I}(\mathrm{Pr}_l)\right] \sqrt{t - t_0}}. \tag{4.4}$$

The numerically calculated values of the dimensionless function $\mathscr{I}(\mathrm{Pr}_l)$ obtained in Roisman (2010) are shown in Figure 4.4 for various liquid Prandtl numbers. In the plotted range the dimensionless function is always smaller than one. For technical purpose, the function can be approximated by fitting the predicted values by a power law function:

$$\mathscr{I}(\mathrm{Pr}_l) \approx 0.17 + 0.47\,\mathrm{Pr}_l^{0.1}, \quad \mathrm{Pr}_l < 100. \tag{4.5}$$

It is obvious that in the limit $\mathrm{Pr}_l \to \infty$ the value of the dimensionless function approaches to $\mathscr{I}(\mathrm{Pr}_l) = 1$ and the solution in (4.1) and (4.2) reduces to the well-known form of the heat conduction problem of two semi-infinite solid bodies (Myers, 1987), which has been already shown by Eq. (1.24) and Eq. (1.25) in section 1.2.1.

If the thickness of the thermal boundary layer is much smaller than the spreading diameter $D_c(t)$, the heat flux in the radial direction is much smaller than the heat flux in the axial direction. The thickness of the thermal boundary layer is of the order $\sqrt{\alpha t} \sim \sqrt{\alpha D_0/U_0}$, whereas the spreading diameter is of the order of D_0. Therefore, the radial heat flow in the liquid and in the wall can be neglected as long as $D_0 U_0/\alpha_l \gg 1$ and $D_0 U_0/\alpha_\mathrm{w} \gg 1$. Since the thermal diffusivity $\alpha_\mathrm{w} \gg \alpha_l$, the stated conditions are fulfilled for:

$$\gamma \,\mathrm{Re}\,\mathrm{Pr}_l \gg 1, \quad \text{with}: \quad \gamma = \frac{\alpha_l}{\alpha_\mathrm{w}}. \tag{4.6}$$

At each radius r, the boundary layer starts to develop at the time $t_0(r)$, when the contact line reaches the position r. The function $t_0(r)$ is the inverse function of radius $R_d(t)$ during the spreading phase. The total heat removed from the substrate during drop spreading is

$$Q(t) = 2\pi \rho_\mathrm{w} c_{\mathrm{p,w}} \int_0^{R_d(t)} \int_{-\infty}^{0} r\,(T_{\mathrm{w}0} - T)\,\mathrm{d}z\mathrm{d}r. \tag{4.7}$$

Equations (4.1) and (4.7) yield the following expression for the total heat

$$Q(t) = \frac{4\sqrt{\pi} e_l e_\mathrm{w} (T_{\mathrm{w}0} - T_{d0})}{e_l + e_\mathrm{w} \mathscr{I}(\mathrm{Pr}_l)} \int_0^{R_d(t)} r\sqrt{t - t_0(r)}\mathrm{d}r, \tag{4.8}$$

which can be differentiated with respect to time, yielding

$$\dot{Q}(t) \equiv \frac{\mathrm{d}Q}{\mathrm{d}t} = \frac{2\sqrt{\pi} e_l e_\mathrm{w} (T_{\mathrm{w}0} - T_{d0})}{e_l + e_\mathrm{w} \mathscr{I}(\mathrm{Pr}_l)} \int_0^{t} \frac{R_d(t_0)\dot{R}_d(t_0)}{\sqrt{t - t_0}}\mathrm{d}t_0. \tag{4.9}$$

The integral in Eq. (4.9) can be evaluated numerically if the evolution of the drop radius $R_d(t)$ is known. However, it becomes singular as long as $t_0 \to t$. An accurate and precise numerical method has to be chosen to evaluate this singular integral. As an alternative, an engineering approximation for the value of the heat $Q(t)$ in Eq. (4.8) is obtained by approximating the evolution of the spreading radius $R_d(t)$

$$R_d(t) \approx R_{\max}\sqrt{1-\left(1-\frac{t}{t_{\max}}\right)^2}, \tag{4.10}$$

where $R_{\max}$ is the maximum spreading radius and $t_{\max}$ is the corresponding time. Equation (4.10) is obtained by fitting the experimental data from Rioboo et al. (2002) for a wide range of impact parameters. It allows the integral in Eq. (4.9) to be expressed in an explicit form for known values of $R_{\max}$ and $t_{\max}$. Consequently, substituting Eq. (4.10) in Eq. (4.9) yields

$$\dot{Q}_{\mathrm{spr}}(t) \approx \frac{4\sqrt{\pi}R_{\max}^2}{t_{\max}}\frac{e_l e_{\mathrm{w}}(T_{\mathrm{w}0}-T_{d0})}{e_l+e_{\mathrm{w}}\mathscr{I}(\mathrm{Pr}_l)}\left(1-\frac{2t}{3t_{\max}}\right)\sqrt{t}, \tag{4.11}$$

which is valid for the spreading phase $0 \le t \le t_{\max}$ of drop impact.

In the receding phase $t > t_{\max}$, the heat associated with the change of the spreading radius of the drop can be neglected. The expression for the heat flow, obtained by the integration of the heat flux over contact area of the receding drop, is derived with the help of Eqs. (4.2) and (4.10):

$$\dot{Q}_{\mathrm{rec}}(t) = \int_0^{R_d(t)} 2\pi r\dot{q}\,\mathrm{d}r \approx \frac{4\sqrt{\pi}e_l e_{\mathrm{w}}(T_{\mathrm{w}0}-T_{d0})}{e_l+e_{\mathrm{w}}\mathscr{I}(\mathrm{Pr}_l)}\frac{R_{\max}^2}{3\sqrt{t_{\max}}}\bar{A}(t), \tag{4.12}$$

where the dimensionless function $\bar{A}(t)$ is defined as

$$\bar{A}(t) = (3-2\chi)\chi^{1/2} + (2\chi-2-\zeta)\sqrt{\zeta+\chi-1}, \tag{4.13a}$$

$$\chi \equiv \frac{t}{t_{\max}}, \quad \zeta \equiv \sqrt{1-\frac{R_d(t)^2}{R_{\max}^2}}. \tag{4.13b}$$

Figure 4.5 shows a comparison of the theoretical predictions, presented in Eq. (4.11) and Eq. (4.12), with some results of numerical simulations for the heat flow $\dot{Q}$ and cumulative heat Q transported from the wall to the fluid. The numerical simulations have been performed in Batzdorf (2016) for a single fluorocarbon drop impacting in the single phase cooling regime. The agreement between the theory and the numerical simulations is very good for the spreading and the receding phase of the impinging drop. This confirms the negligible effect of evaporation for the chosen drop impact conditions and times. In Fig. 4.5(a) the maximum heat flow in the theoretical prediction

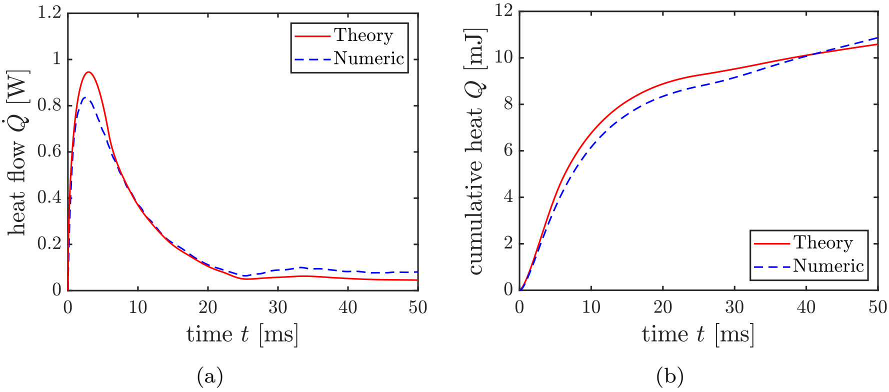

Figure 4.5: (a) Heat flow $\dot{Q}$ and (b) cumulative heat Q during impact of a single fluorocarbon drop in the single phase cooling regime as a function of time. Comparison of the theoretical prediction (solid lines) with results of numerical simulations (dashed lines) obtained in Batzdorf (2016). The impact conditions are: $D_0 = 0.977$ mm, $U_0 = 0.584$ m/s, $T_{\mathrm{w}0} = 74\,^\circ$C, $T_{d0} = 56\,^\circ$C, $\mathrm{Re} = 1500$, $\mathrm{Pr}_l = 9.54$. (Reprinted (adapted) from Batzdorf et al. (2017). © 2017 Elsevier.)

is around 13% higher than the numerical results. The cumulative heat in Fig. 4.5(b) varies less than 3% at the time instant $t = 50\,\mathrm{ms}$.

The developed theoretical model does not take into account the effect of drop evaporation on the overall heat transport. Therefore, the prediction is only valid during drop impact if the heat transport rate due to evaporation is small compared to the heat transfer due to convection. Since the role of convection increases with increasing Peclet number $\mathrm{Pe} = \mathrm{Re}\,\mathrm{Pr}_l$, it can be suggested that, if the Reynolds number is fixed, the theoretical model is more accurate for liquids with high Prandtl number. In order to verify this presumption, the scaled heat is introduced:

$$E^* = \frac{6Q}{\pi \rho_l D_0^3 L}. \tag{4.14}$$

Here L is the latent heat of evaporation. The heat E^* relates the heat transferred to the drop to the maximum possible heat. This maximum amount is the necessary heat to evaporate the drop completely.

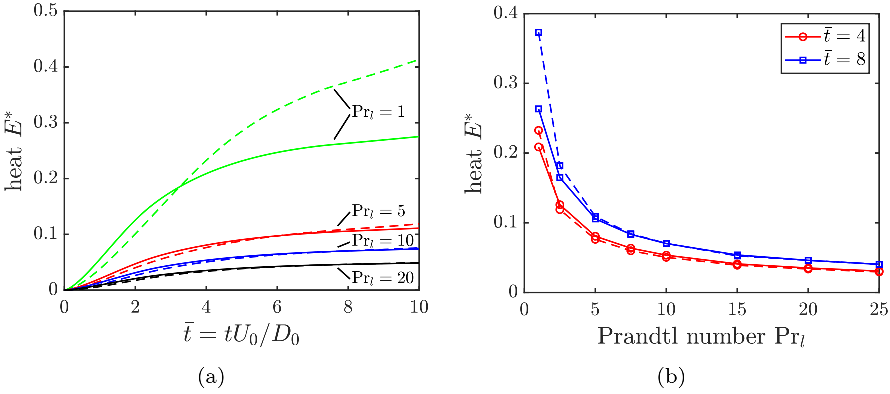

Figure 4.6: Dimensionless heat E^* as (a) a function of the dimensionless time $\bar{t}$ at different values of the liquid Prandtl number Pr_l and (b) a function of the liquid Prandtl number Pr_l at two instants of time $\bar{t}$. Comparison of the theoretical prediction (solid lines) with results of numerical simulations (dashed lines) obtained in Batzdorf (2016). The impact conditions are: $D_0 = 1.021$ mm, $U_0 = 0.2739$ m/s, $T_{\mathrm{w}0} = 66\,^\circ\mathrm{C}$, $T_{d0} = 56\,^\circ\mathrm{C}$, $\mathrm{Re} = 735$. (Reprinted (adapted) from Batzdorf et al. (2017). © 2017 Elsevier.)

In Fig. 4.6(a) the scaled heat E^* is depicted as a function of the dimensionless time $\bar{t} = tU_0/D_0$ for various liquid Prandtl numbers Pr_l, and Fig. 4.6(b) demonstrates the scaled heat E^* as a function of Pr_l for the fixed values $\bar{t} = 4$ and $\bar{t} = 8$. The theoretical prediction is shown as solid line, while the results of numerical simulations (Batzdorf, 2016) are depicted by a dashed line. It is obvious that the results of the theoretical prediction agree very well with the numerical simulation for $\mathrm{Pr}_l \geq 5$ over the entire range of $\bar{t}$. Only for smaller Prandtl numbers of the order unity, the deviations between both results are quite high, especially at high values of $\bar{t}$. This is confirmed by the numerical simulations, showing that for the same impact parameters and initial temperatures used for the theoretical predictions, at $\mathrm{Pr}_l = 1$ approximately 40% of the drop mass evaporates before the time instant $\bar{t} = 10$. Compared to this high value, for $\mathrm{Pr}_l \geq 5$ the total evaporation of the drop (until the same time) is smaller than 10% (Batzdorf, 2016). This indicates that the theoretical prediction is valid for Prandtl numbers $\mathrm{Pr}_l \geq 5$, which means that the effect of drop evaporation is small compared to the heat convection.

After the validation of the theoretical model in the previous part, the heat transfer during drop impact in the single phase cooling regime can be estimated from the experimental observations, as long as the conditions mentioned above are fulfilled. Figure 4.7 shows the results of the theoretical prediction for five different drop impact cases, which have been shown in section 4.1.1. It is obvious, that they differ widely in heat transfer due to the increasing contact temperature of the five different cases. Nevertheless, the main heat is transferred during the spreading phase of drop impact. This implies that the rising maximum spreading diameter for higher initial substrate temperatures (c.f. Fig. 4.3) also accounts for a large part of the increasing heat transfer. A further reason is the increasing temperature difference between initial substrate and contact temperature (which strongly influences the heat transfer) for a higher substrate temperature, as shown in Fig. 4.7(a).

4.1.3 Heat transfer during the simultaneous impact of two drops

The developed theoretical model from the previous section can be extended to estimate the heat transfer during the simultaneous impact of two drops. An sketch is exemplary shown in Fig. 4.8 for two drops impacting onto a hot substrate with a constant distance b, correspondingly with the spacing parameter $e = b/D_0$. In this case the heat transfer rate for each drop is first calculated with Eqs. (4.11) and (4.12). Afterwards, the result is corrected by excluding the heat transfer from the area where the wetted regions overlap, produced by the two spreading drops. For simplicity it is assumed, that the average heat flux transferred in the overlapped region is equal to the average heat flux over the wetted region, since the overlapping of the two regions do not occur in the initial time steps. As a result, the heat transfer rate computed by Eqs. (4.11) and (4.12) is multiplied with a transient area ratio factor η which accounts for the drop interaction

$$\dot{Q}_{\text{multi}} = 2\,\eta(t)\,\dot{Q}_{\text{single}}, \tag{4.15}$$

$$\eta(t) = \frac{A_e}{A_{e\to\infty}}, \tag{4.16}$$

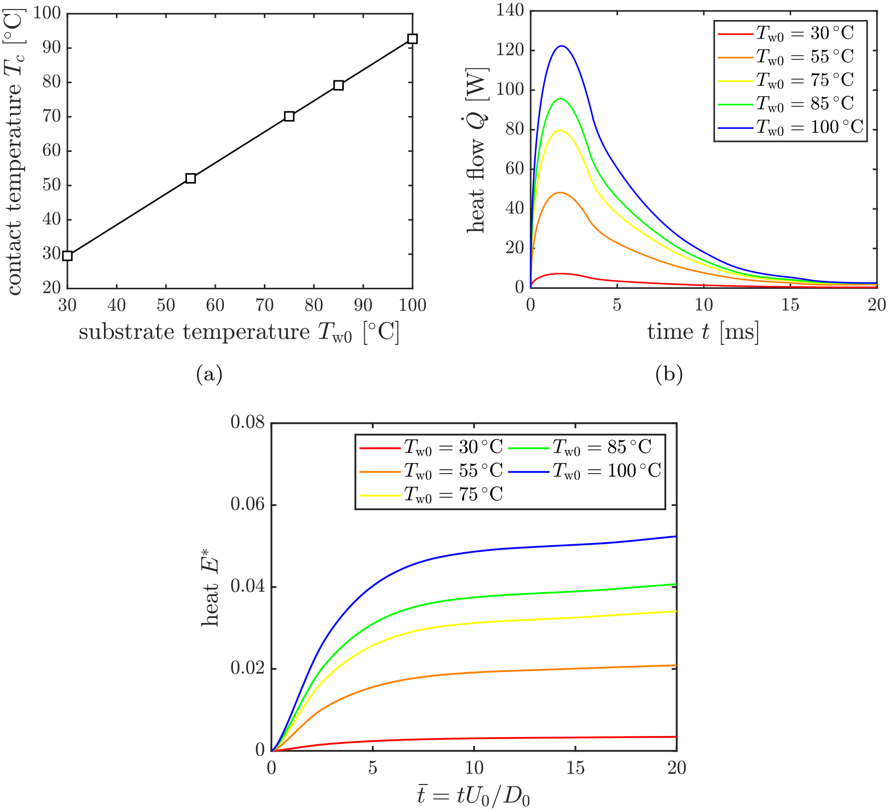

(a) (b)

(c)

Figure 4.7: Results of the theoretical prediction (4.11)-(4.12) for the five different experimental cases shown in section 4.1.1: (a) estimated contact temperature, (b) heat flow $\dot{Q}$ as a function of time and (c) scaled heat E^* as function of time. The initial fluid temperature $T_{d0} = 25\,°\mathrm{C}$, drop diameter $D_0 = 2.3\,\mathrm{mm}$, impact velocity $U_0 = 1.6\,\mathrm{m/s}$, Reynolds number Re, liquid Prandlt number $\mathrm{Pr}_l = 6.2$ is constant for all cases.

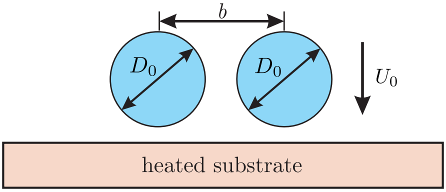

Figure 4.8: Sketch of the simultaneous impact of two drops with the important parameters.

where $A_{e\to\infty} = 2\pi R_d^2(t)$ is the instantaneous wetted area produced by two drops which are far away from each other ($e \to \infty$) and do not coalesce. The area A_e is the cumulative wetted area produced by two drops which coalesce for the case $R_{\max} > b/2$. In the present thesis, this area has been estimated by the relation

$$A_e = \begin{cases} A_{e\to\infty}, & R_d(t) < b/2, \\ 2R_d^2(t)\arccos\left[\frac{b}{2R_d(t)}\right] - \frac{b}{2}\sqrt{4R_d^2(t) - b^2}, & R_d(t) > b/2. \end{cases} \tag{4.17}$$

In order to validate the predicted approach, a representative numerical case for the simultaneous impact of two fluorocarbon drops has been taken from Batzdorf (2016). Since the radius over time is necessary for the evaluation of Eqs. (4.11)-(4.17), the spreading radius $R_d(t)$ has been taken from a numerical simulation for a similar single drop impact. Figure 4.9(a) shows the results of the theoretical prediction, whereas the results of numerical simulations are demonstrated in Fig. 4.9(b). The results are presented for three different spacing ratios e. The qualitative agreement between the numerical simulations and the theoretical predictions is good. Similar to the single drop case (c.f. Fig. 4.5), the maximum heat flow is overestimated in the theoretical prediction. In the case $e = 1.5$ the theoretical prediction overestimates the numerical value of a maximum heat flow by 18%.

The equivalent cumulative heat Q of the simultaneous impact of two drops for the theoretical prediction and the numerical simulation are shown in Fig. 4.10(a) and Fig. 4.10(b) for the three different spacing ratios. Both, theoretical results and results of numerical simulations, predict that the heat flow is not influenced by the presence of a second drop as long as the drops do not touch each other. As soon as the drops start to coalesce, the heat transfer

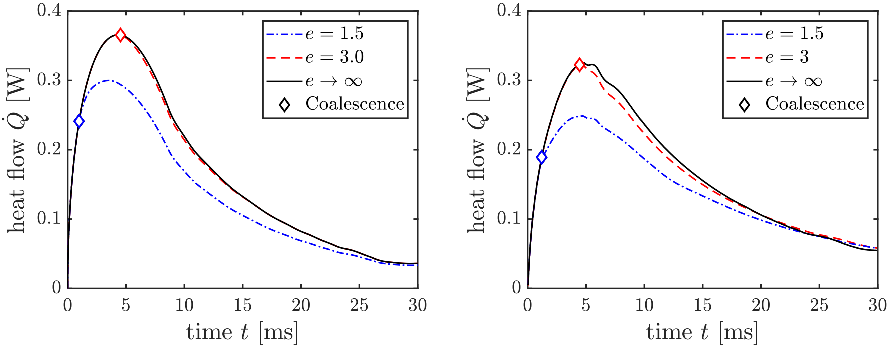

(a) (b)

Figure 4.9: Total wall heat flow $\dot{Q}$ for two simultaneously impinging drops as function of time t for different spacing ratios e: (a) theoretical prediction vs. (b) results of numerical simulations obtained in Batzdorf (2016). The diamonds symbolize the coalescence events for the various cases. The impact parameters are $D_0 = 0.977\,\mathrm{mm}$, $U_0 = 0.2861\,\mathrm{m/s}$, $T_{\mathrm{w}0} = 66\,°\mathrm{C}$, $T_{d0} = 56\,°\mathrm{C}$, $\mathrm{Re} = 700$, $\mathrm{Pr}_l = 9.54$. (Reprinted (adapted) from Batzdorf et al. (2017). © 2017 Elsevier.)

decreases in comparison with the case of two drops spreading independently from each other. The decrease of heat transport (for the set of parameters chosen in this case) can be attributed to the decrease of the cumulative solid/liquid contact area compared with the area which can be occupied by two independently spread drops. It will be suggested that at later stages, when the flow in the liquid completely vanishes, the thermal boundary layers are completely developed and evaporation becomes the major mechanism of heat transfer, a second reason for decreasing the heat transfer rate due to drop coalescence appears. Namely, the cumulative length of the contact line is reduced due to coalescence. Since the high evaporation rates near the contact line contribute significantly to the overall heat transfer at the last stages of evaporation (Herbert et al., 2013), it can be expected that at these stages the reduction of heat flow due to drop coalescence would be significant.

The results and methods presented in the present section can be applied to prediction of the influence of drop coalescence following multiple drop impact onto a hot surface and finally for a prediction of the heat transfer

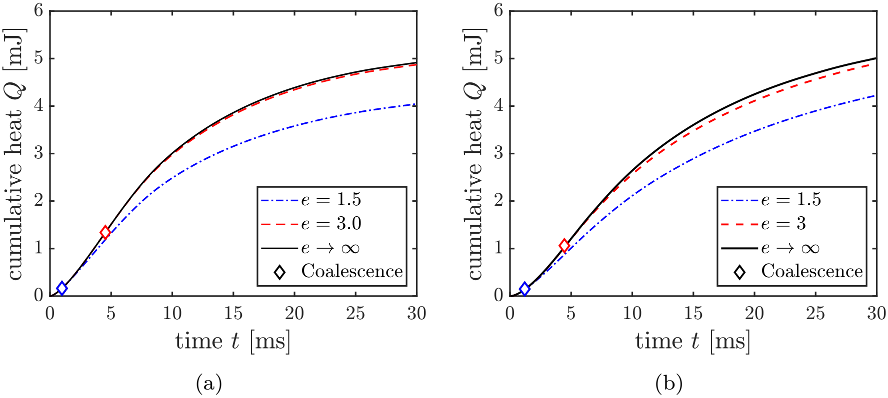

Figure 4.10: Cumulative heat Q for two simultaneously impinging drops as function of time t for different spacing ratios e: (a) theoretical prediction vs. (b) results of numerical simulations obtained in Batzdorf (2016). The case is similar to Fig. 4.9. (Reprinted (adapted) from Batzdorf et al. (2017). © 2017 Elsevier.)

during spray impact. In the long term the distribution of drop diameters, velocities, impact frequency and the spatial distribution of drops in spray will be tailored in order to optimize the spray cooling efficiency.

In the present thesis the values for the spreading radius $R_d(t)$ of the impinging drop are used from the numerical computations only to validate the applicability of the theory in Roisman (2010). However, for practical purposes of spray cooling modeling, existing models for these values should be used. The model for the maximum spreading diameter from Roisman (2009) is recommended, since it is based on the exact solution for the residual film thickness and it is already validated by comparison with the experimental results from various groups (Visser et al., 2015; Wildeman et al., 2016).

An approximate semi-analytical solution for the drop radius $R_d(t)$ during spreading and receding can be found in Roisman et al. (2002) for the cases $\mathrm{Re} \gg 1$ and $\mathrm{We} \gg 1$. The evolution of the droplet radius is estimated for several liquid/wall systems and impact parameters and compared with experimental data from the literature to validate their theoretical analysis. In order to demonstrate the application of the theoretical solution described in the previous parts, two cases have been chosen to investigate the influence of the spacing parameter e on heat transfer during simultaneous impact of two droplets: (a) $D_0 = 3.7\,\mathrm{mm}$ & $U_0 = 1.58\,\mathrm{m/s}$ and (b) $D_0 = 3.7\,\mathrm{mm}$ & $U_0 = 3.76\,\mathrm{m/s}$.

In Fig. 4.11(a) the heat Flow $\dot{Q}$ and in Fig. 4.11(b) the cumulative heat Q for two simultaneously impinging drops as a function of time t for different spacing ratios e and impact velocities U_0 are shown. The drop radius during spreading and receding has been calculated using the solution in Roisman et al. (2002). It is obvious that the heat flow $\dot{Q}$, and consequently the cumulative heat Q, increase for higher spacing ratios e since the drop coalescence will be delayed. Noteworthy is the fact, that the maximum heat flow $\dot{Q}$ also increases for a higher impact velocity, despite the fact that the drop coalescence event occurs earlier for an increasing impact velocity. This can be explained by an increasing R_{max} and a decreasing t_{max} for higher impact velocities (Roisman et al., 2002). This results in a much faster contact line velocity and development of the thermal boundary layer.

In Fig. 4.11(c) the cumulative heat Q for various spacing ratios e and impact velocities U_0 has been divided by the cumulative heat $Q_{e\to\infty}$ for the case of two independently spreading drops. It is shown that the effective heat $Q/Q_{e\to\infty}$ decreases for higher impact velocity and furthermore the drop coalescence occurs much earlier. This indicates an contrarily behavior in comparison to Fig. 4.11(a) and (b): even if the heat flux $\dot{Q}$ and cumulative heat Q increase for a higher impact velocity, the effectiveness of the heat transfer during simultaneous impact of two drops onto a hot solid substrate, expressed with the effective heat $Q/Q_{e\to\infty}$, decreases.

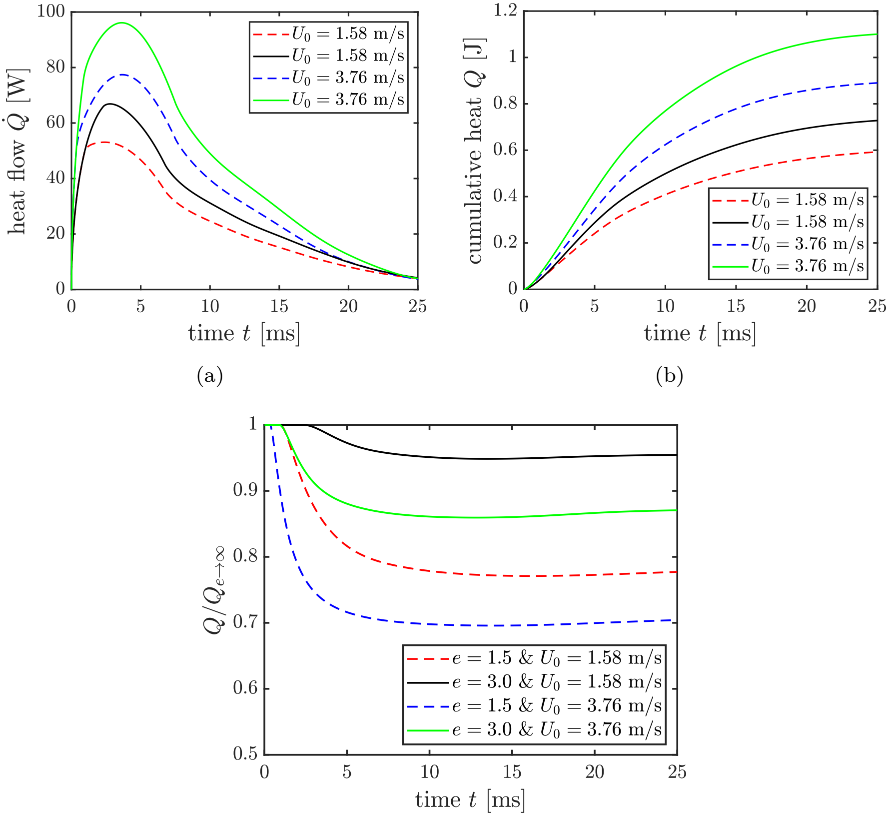

(a)

(b)

(c)

Figure 4.11: (a) Heat flow $\dot{Q}$, (b) cumulative heat Q and (c) effective heat $Q_e/Q_{e\to\infty}$ for two simultaneously impinging drops as function of time t for different impact velocities U_0. The spacing ratios are $e = 1.5$ (dashed line) and $e = 3$ (solid line). Further constant parameters are $D_0 = 3.7\,\text{mm}$, $T_{\text{w}0} = 40\,^\circ\text{C}$ K, $T_{d0} = 20\,^\circ\text{C}$, $\text{Pr}_l = 7.0$. The drop radius has been calculated using the approximation solution in (Roisman et al., 2002). (Reprinted (adapted) from Batzdorf et al. (2017). © 2017 Elsevier.)

5 Drop impact accompanied by boiling

In the present chapter the non-isothermal drop impact accompanied by boiling is investigated, *i.e.* section 5.1 describes the drop impact in the nucleate boiling regime, section 5.2 the drop impact in the thermal atomization regime, and section 5.3 the drop impact in the film boiling regime. After a short introduction, each section illustrates the main observations of the various phenomena. Furthermore, the different sections provide various investigations and theoretical descriptions of the observed phenomena.

5.1 Nucleate boiling regime

At surface temperatures above the boiling onset drop evaporation is caused by nucleate boiling. During nucleate boiling small vapor bubbles frequently form at the drop/wall surface, detach from the surface, ascend through the drop and possibly coalesce with other bubbles. However, as already discussed in section 1.2.2, the physics of drop impact accompanied with boiling are rather complicated, therefore mainly experimental research has been performed in the past, leading to various boiling curves and empirical correlations for the heat transfer or the critical heat flux.

In the present section the main observations for a drop impact in the nucleate boiling regime are shown. Furthermore the heat transfer in the solid substrate under the sessile drop is analyzed theoretically. The sessile drop is considered since the time scale of spreading is three orders of magnitude smaller than the time scale of drop evaporation. This analysis allows the prediction of the amount of heat transferred from the substrate to the drop and the estimation of the typical time of drop evaporation, two quantities of paramount importance for spray cooling applications. Parts of this section have been published in Breitenbach et al. (2017a, 2018b). Furthermore, parts of the experimental investigations have been described in the thesis of v. Kieckebusch (2018).

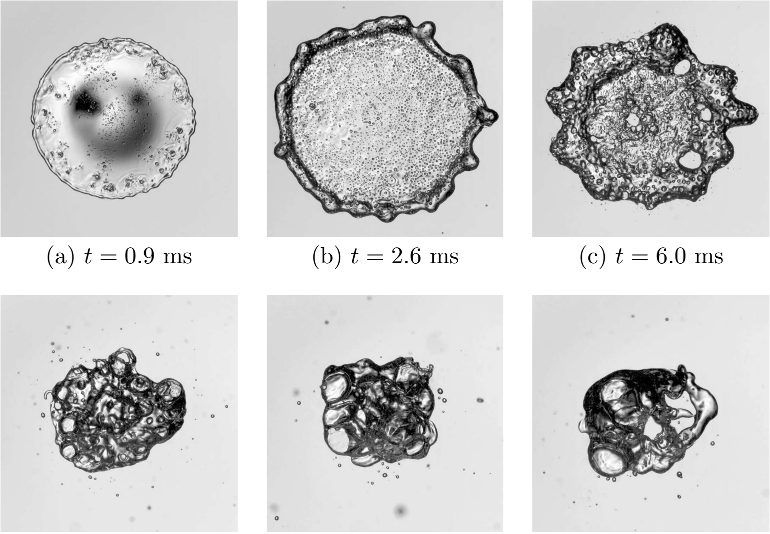

(a) $t = 0.9$ ms (b) $t = 2.6$ ms (c) $t = 6.0$ ms

(d) $t = 12.1$ ms (e) $t = 34.1$ ms (f) $t = 61.7$ ms

Figure 5.1: Exemplary bottom view through a transparent sapphire substrate on a drop impact during nucleate boiling ($T_{\mathrm{w0}} = 160\,^{\circ}\mathrm{C}$). Note that sapphire is used as impact target and the temperature threshold for nucleate boiling can be different to the aluminium substrate. (Reprinted (adapted) from Breitenbach et al. (2017a), with permission of the American Physical Society. © 2017 American Physical Society.)

5.1.1 Observations

A bottom view through a transparent sapphire target on a drop impact in the nucleate boiling regime is shown exemplary in Fig. 5.1. In this typical example the contact area of the drop is completely covered by vapor bubbles, already after $3 - 6$ ms. This time is much shorter than the overall time of drop contact with the hot substrate wall, which is in the order of seconds. The phenomenon is caused by the well-known fact that drop impact initiates creation of numerous micro-bubbles (Bankoff, 1958; Mehdi-Nejad et al., 2003; Thoroddsen et al., 2005), which lead to further bubble nucleation.

After the impact onto the sapphire substrate the drop first spreads and then starts to recede. The duration of drop spreading and receding is in the order of $t_i = D_0/U_0$. At longer times $t > 10$ ms the size of the wetted area

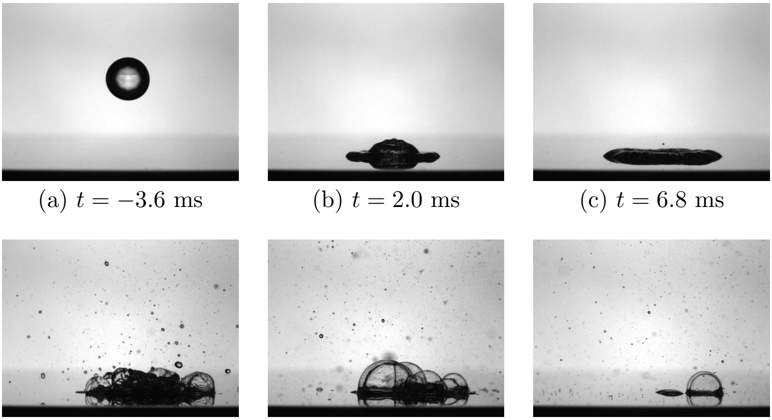
(a) $t = -3.6$ ms (b) $t = 2.0$ ms (c) $t = 6.8$ ms

(d) $t = 30.4$ ms (e) $t = 160$ ms (f) $t = 290$ ms

Figure 5.2: Impinging water droplet in the nucleate boiling regime at initial substrate temperatures $T_{\mathrm{w0}} = 140\,^{\circ}\mathrm{C}$ for the impact parameters $D_0 = 2.2\,\mathrm{mm}$ and $U_0 = 0.7\,\mathrm{m/s}$. (Reprinted (adapted) from Breitenbach et al. (2017a), with permission of the American Physical Society. © 2017 American Physical Society.)

does not change significantly, despite the mass reduction of the drop caused by an intensive evaporation and creation of secondary drops. This has been observed for all cases. The contact line remains almost pinned during the major part of drop evaporation. This is an interesting observation, since the contact area is related to the rate of heat flow. The contact line pinning is explained by the continuous generation of the bubbles, which prevents the receding of the contact line even if the drop volume decrease due to the drop evaporation. Exemplary, Fig. 5.2 shows the side-view of an impinging drop onto a aluminum substrate at initial substrate temperatures $T_{\mathrm{w0}} = 140\,^{\circ}\mathrm{C}$. Similar to the bottom-view observations, the wetted area is almost constant over a long time during evaporation. Only at the end, right before the drop is nearly fully evaporated, the wetted area starts to decrease.

During nucleate boiling some drop mass is lost due to the generation of small secondary drops. The mass of the secondary drops is significant in the transition boiling regime, when the drop seems to dance onto the hot substrate surface and liquid layers, as well bubbles frequently collapse. In the nucleation boiling regime considered in this section, the total mass of

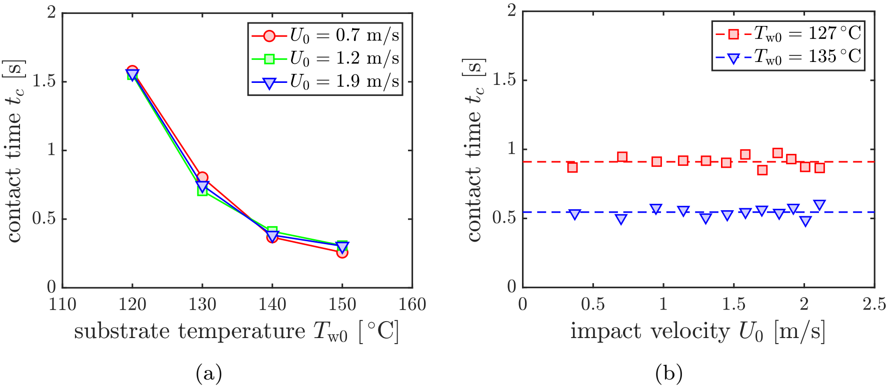

Figure 5.3: Contact times in the nucleate boiling regime: (a) experimental data as a function of the initial wall temperature for different impact velocities (Reprinted (adapted) from Breitenbach et al. (2017a), with permission of the American Physical Society. © 2017 American Physical Society.). (b) Experimental data as a function of the impact velocity for different substarte temperatures. The dashed lines represent the arithmetic mean value, while the standard deviation is less than 8%. The impact diameter is $D_0 = 2.2\,\text{mm}$ for all cases.

the secondary drops usually does not exceed 10% of the initial drop mass. Therefore, the assumption can be made that in the nucleate boiling regime most of the heat from the substrate goes into drop vaporization through intensive bubble creation.

5.1.2 Contact time of an impacting drop

The duration of contact between the drop and the hot substrate, the contact time, is an important quantity which strongly influences the heat removed by the impacting drop from the substrate. As such, this quantity is a necessary element of any spray cooling model since it can help to estimate the heat flux between the substrate. In Fig. 5.3(a) an example contact time in the nucleate boiling regime is shown as a function of the initial surface temperature T_{w0} for various impact velocities U_0. The time is measured until complete drop evaporation on the hot substrate.

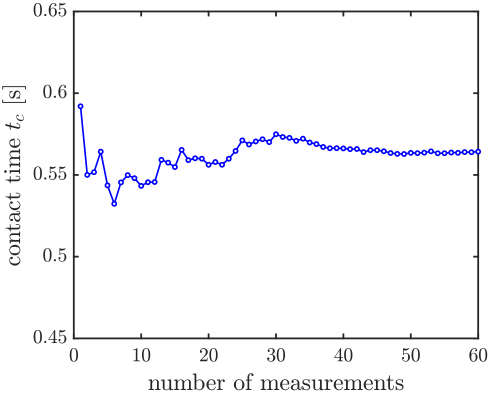

Figure 5.4: Convergence of the cumulative contact time t_c over the number of measurements taken into account. The impact conditions are constant: initial substrate temperature $T_{\mathrm{w0}} = 135\,^{\circ}\mathrm{C}$, impact diameter $D_0 = 2.2\,\mathrm{mm}$ and impact velocity $U_0 = 0.6\,\mathrm{m/s}$.

In the nucleate boiling regime the contact time reduces with increasing surface temperature, since the transferred heat flux rises. The dependence of the contact time t_c on the temperature is expressed well by the relation

$$t_c \sim (T_{\mathrm{w0}} - T_{\mathrm{sat}})^{-1.92}, \tag{5.1}$$

obtained by fitting of the experimental data. Existing models for the heat transfer during nucleate boiling (Rohsenow, 1962; Forster & Zuber, 1955; Bernardin & Mudawar, 2004, 2002; Carey, 1992) are not applicable for the description of the phenomenon considered in the present thesis. However, the contact time is not influenced by the impact velocity of the impinging drop. This is shown in Fig. 5.3(b) and can be explained by the much smaller timescale of the drop impact time $t_i \sim D_0/U_0$ in comparison to the overall time of evaporation. The dashed lines represent the arithmetic mean value, while the standard deviation is less than 8%. Some fluctuations of the measured contact time are common due to stochastic effects of the boiling process, *e.g.* nucleation and mass loss due to secondary droplets. Therefore, the convergence of the cumulative contact time t_c is shown in Fig. 5.4 over the number of measurements taken into account.

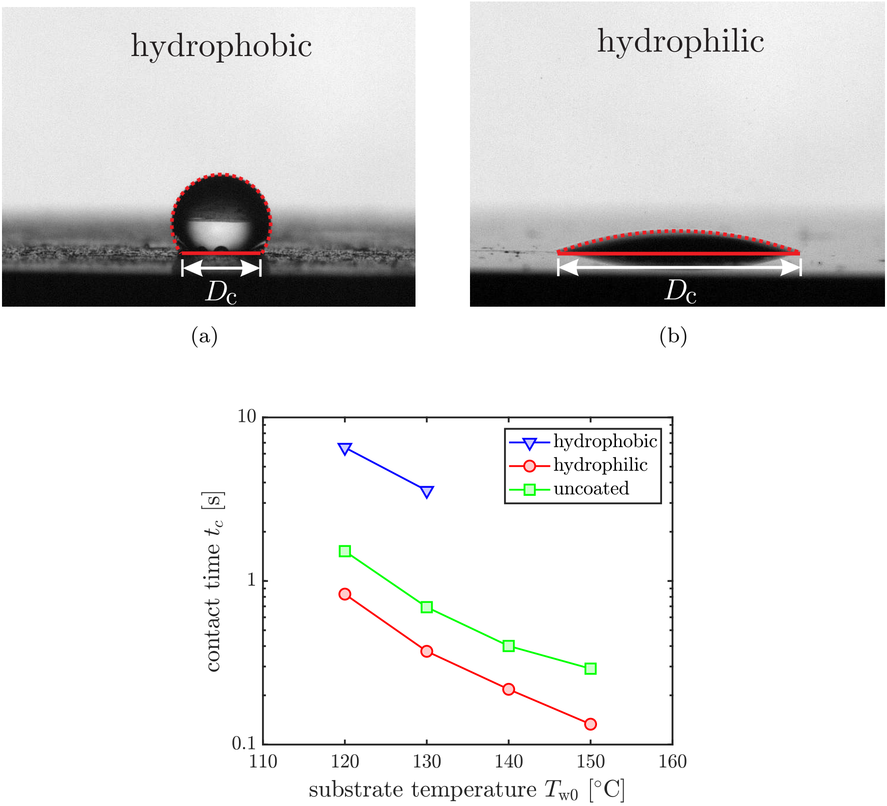

(a)

(b)

(c)

Figure 5.5: Drop impact onto a hot coated surfaces in the nucleate boiling regime: contact area of the drop with the hot substrate for a (a) highly hydrophobic and (b) highly hydrophilic coated surface. (c) The contact time as a function of the initial substrate temperature for various surface conditions. The time decreases for a larger contact area of the drop with the hot substrate. The impact conditions are $D_0 = 2.2\,\text{mm}$ and $U_0 = 1.4\,\text{m/s}$ for all cases. For the hydrophobic case, temperatures $T_{w0} > 135\,^\circ\text{C}$ lead to rebound.

By changing the surface wettability of the substrate the contact time of the drop can be significantly influenced. This is exemplary shown in Fig. 5.5 for different surface wettabilities: highly hydrophilic and highly hydrophobic coated in comparison to an uncoated aluminum substrate. To influence the surface wettability of the surface, a polished aluminum substrate (contact angle $\theta_c \approx 80^\circ$) has been coated with polymer nanoparticles (Synytska et al., 2014): the hydrophobic surface is coated with 800 nm PDMS (polydimethylsiloxane) particles, while the hydrophilic surface is coated with 800 nm PEG (polyethyleneglycol) particles. It is obvious that the contact time significantly decreases for the hydrophilic surface, while for the hydrophobic case the contact time increases. This can be explained by the change of contact angle and consequently by the change of the wetted area. The time of drop evaporation strongly depends on the rate of heat flow $\dot{Q}$ from the substrate to the drop. Since the heat flow increases for increasing contact area A_c, the contact time can be scaled as $t_c \sim 1/A_c$. A picture of the different contact diameters D_c for the hydrophobic and hydrophilic surface is shown in Fig. 5.5(a) and (b). The diameter of the hydrophobic case is roughly three times less compared to the hydrophilic case, which leads to a nine times less contact area. This difference is in excellent agreement with the lag in contact time between hydrophobic and hydrophilic case, shown in Fig. 5.5(c).

An approximate model for the heat transfer which accounts for only main physical influencing factors and is able to predict the contact time of a drop in the nucleate boiling regime will be described in the following section.

5.1.3 Evaluation of heat transfer during drop evaporation

Heat transfer during the waiting time

During a very short time interval after drop collision the bubbles created by the drop impact are very small. Their sizes are comparable with the roughness of the substrate which is in the order of 1 μm. The relative area of the wetted substrate occupied by bubbles is initially very small. In the present experiments, shown exemplary in Fig. 5.1, the waiting time for bubble nucleation is approximately 1 ms and the typical time for complete saturation of the wetted area by bubbles is 3 ms.

At the initial phase of drop spreading, during the absence of evaporation, the temperature at the solid/liquid interface can be described by the well known contact temperature (Myers, 1987; Roisman, 2010). It can be estimated considering the heat conduction in the substrate, heat convection in the spreading drop and the boundary conditions at the interfaces. The expressions for the contact temperature and for the heat flux density at the interface are obtained in section 4.1.2 in the form

$$T_c = \frac{\mathscr{I}(\mathrm{Pr}_l) e_\mathrm{w} T_{\mathrm{w}0} + e_l T_{d0}}{\mathscr{I}(\mathrm{Pr}_l) e_\mathrm{w} + e_l}, \tag{5.2}$$

$$\dot{q}(t) = \frac{e_l e_\mathrm{w} (T_{\mathrm{w}0} - T_{d0})}{(e_l + \mathscr{I}(\mathrm{Pr}_l) e_\mathrm{w}) \sqrt{\pi} \sqrt{t}}, \tag{5.3}$$

where T_{d0} and $T_{\mathrm{w}0}$ are the initial temperatures of the drop and of the substrate, Pr_l is the Prandtl number for the drop liquid, e_l and e_w are the corresponding thermal effusivities of the liquid and the solid substrate, respectively. The function $\mathscr{I}(\mathrm{Pr}_l)$ can be calculated with the liquid Prandtl number according to Eq. (4.5). However, during nucleate boiling the waiting time for the inception of the bubble growth is three orders of magnitude smaller than the drop evaporation time. The solution (5.2)-(5.3) therefore has no significant influence on the final expression for the evaporation time or the overall heat flow.

Single bubble formation

The phenomena of bubble nucleation and growth in nucleate boiling regime have been already discussed in section 1.2.2. For the present experiments, the characteristic size of the bubbles in the drop are in the order of 1 mm, already after 10 ms, as seen in Fig. 5.1. At this time the thickness of the thermal boundary layer in the liquid $\sqrt{\alpha_l t}$ is approximately $40\,\mu$m. The bubble size is much larger than the thickness of the thermal boundary layer. For this very reason, bubble evaporation occurs only in the region in the close vicinity of the wall, near the contact line and in a thin wall film (c.f. Fig. 1.5). This means that the bubble growth is caused solely by the evaporation in the evaporating microlayer. This conclusion is supported by the fact that the predictions of the drop evaporation time based on the models of Stephan & Hammer (1994) and Bernardin & Mudawar (2002) do not agree well with the present experimental data obtained.

In the present thesis the value of the factor β in the expression for the bubble radius in Eq. (1.35) is $\beta \sim 10^{-3}\,\mathrm{m/s^{0.5}}$, which is estimated by fitting the radius evolution of the observed bubbles. Therefore, the estimated thickness of the evaporating layer is $h_{l0} \sim 10^{-2} R_B$. For an typical heat flux density $\dot{q} \sim 10^6\,\mathrm{W/m^{-2}}$ (estimated in the present thesis) and the average bubble radius $R_B \sim 0.5\,\mathrm{mm}$, for which $h_{l0} \approx 4\,\mu\mathrm{m}$, the temperature deviation at the interface is approximately 7 °C. A static microlayer of the thickness h_{l0} at this heat flux evaporates in approximately 10 ms. This time is comparable with the observed bubble growth time before its departure or collapse. Therefore, the evaporating layer exists during the entire process of bubble growth.

Nucleate boiling in an impacting drop

Drop collision with the hot substrate initiates the start of heat transfer in the solid and liquid regions. In the solid wall, heat is transferred by conduction. In the liquid region, heat convection is determined by the rather complicated flow in the drop during its spreading, influenced by the expansion and motion of the vapor bubbles.

The overall energy balance of heat transfer from the evaporating sessile drop and the heat flux from the substrate is given by

$$\int_0^{t_c} A_c(t)\dot{q}(t)\,\mathrm{d}t \approx \rho_l L^* \frac{\pi D_0^3}{6}, \tag{5.4}$$

where A_c is the contact area, $\dot{q}$ is the heat flux density at the solid/liquid interface, D_0 is the initial drop diameter, ρ_l is the density of the liquid, and $L^* = L + \Delta H_0$ is the sum of the latent heat of evaporation L and the enthalpy difference ΔH_0 between the initial drop and saturated liquid. Equation (5.4) is based on the assumption that the energy goes entirely into drop evaporation. This assumption is only valid for the cases of nucleate boiling, for which the relative mass of fine secondary droplets, generated during drop boiling, is small. In the absence of drop rebound the ejected mass ratio in the nucleate boiling regime, estimated in our experiments, is less than 10%.

At the first instant of drop contact a thermal boundary layer develops in the substrate. The thickness of the thermal boundary layer is $\delta_\mathrm{w} \sim \sqrt{\alpha_\mathrm{w} t}$, where α_w is the thermal diffusivity of the wall material. Since the thickness of the

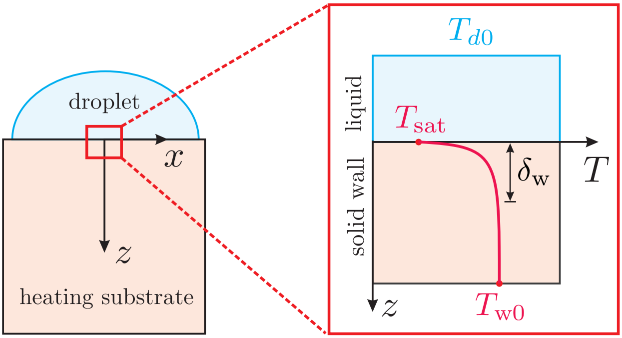

Figure 5.6: Sketch of the assumed temperature distribution within the solid material due to contact of the liquid with the substrate. The solid/liquid interface is located at $z = 0$. (Reprinted (adapted) from Breitenbach et al. (2017a), with permission of the American Physical Society. © 2017 American Physical Society.)

boundary layer is much smaller than the drop diameter, the heat conduction in the substrate can be approximated by a one-dimensional model. The temperature at the solid/liquid interface is not uniform. It is influenced by the appearance and growth of the bubbles initiated by heterogeneous nucleation at the substrate surface. As mentioned in the previous section, the temperature of the wall beneath the bubble and at the substrate in the relaxation layer outside the bubble is close to the saturation temperature T_{sat}, since it is determined by the liquid evaporation in the thin evaporation microlayer.

Moreover, as seen in the bottom view of the boiling drop exemplary shown in Fig. 5.1, the relative area of the bubbles on the substrate during the long phase of drop evaporation (at times larger than the time of drop spreading, 9 ms) is rather high, above 90%. Therefore, as a rough approximation a nearly uniform interface temperature T_{sat} of the substrate can be assumed.

The geometry and the definition of the coordinate system are shown schematically in Fig. 5.6. At $t = 0$ the liquid is placed in contact with a semi-infinite wall $z > 0$ at the initial temperature T_{w0}. The heat conduction equation in the wall

$$\frac{\partial T_{\text{w}}}{\partial t} - \alpha_{\text{w}} \frac{\partial^2 T_{\text{w}}}{\partial z^2} = 0, \tag{5.5}$$

has to be solved subject to the boundary conditions

$$T_\mathrm{w} = T_\mathrm{sat} \quad \text{at} \quad z = 0; \quad T_\mathrm{w} \to T_\mathrm{w0} \quad \text{at} \quad z \to \infty, \tag{5.6}$$

where $T_\mathrm{w}(z,t)$ is the temperature in the wall region. The similarity solution of Eqs. (5.5)-(5.6) is well-known (Roisman, 2010):

$$T_\mathrm{w}(z,t) = T_\mathrm{sat} + (T_\mathrm{w0} - T_\mathrm{sat})\,\mathrm{erf}\left(\frac{z}{2\sqrt{\alpha_\mathrm{w} t}}\right). \tag{5.7}$$

The heat flux density at the solid/liquid interface can be expressed with the help of Eq. (5.7) as

$$\dot{q}(t) \equiv \lambda_\mathrm{w} \frac{\partial T_\mathrm{w}}{\partial z}\bigg|_{z=0} = \frac{e_\mathrm{w} \Delta T_\mathrm{w}}{\sqrt{\pi}\sqrt{t}}, \tag{5.8}$$

where λ_w is the thermal conductivity of the wall material, e_w is the thermal effusivity, and $\Delta T_\mathrm{w} = T_\mathrm{w0} - T_\mathrm{sat}$ is the overall temperature difference in the wall (c.f. Fig. 5.6).

The contact area $A_c(t)$ changes during drop spreading and receding. However, since the contact time t_c in the nucleate boiling regime is much longer than the impact time $t_i \sim D_0/U_0$ and contact line pinning has been observed during evaporation, the contact area can be estimated in the form

$$A_c \approx k_\mathrm{w} \pi D_0^2, \tag{5.9}$$

where the coefficient k_w is determined primarily by the surface structure and wettability. The coefficient k_w accounts also for the effective drop growth due to bubble expansion, for the mass loss during atomization and for some small deviation of the interface temperature from the saturation temperature. This coefficient is of order unity and can be determined from the experiments in Fig. 5.3(a). Substituting expressions (5.7), (5.8), and (5.9) in the energy balance equation (5.4) yields

$$t_c = \pi \left(\frac{\rho_l L^* D_0}{12 k_\mathrm{w}\, e_\mathrm{w} \Delta T_\mathrm{w}}\right)^2. \tag{5.10}$$

It is important to note that the obtained dependence $t_c \sim \Delta T_\mathrm{w}^{-2}$ is in good agreement with the empirical correlation, obtained in Eq. (5.1). Introducing the scaled wall temperature and dimensionless time in the form

$$\Theta = \frac{T_\mathrm{w0} - T_\mathrm{sat}}{T_\mathrm{sat} - T_{d0}}, \quad \bar{t} = \frac{t}{\pi}\left[\frac{12\, e_\mathrm{w}\ (T_\mathrm{sat} - T_{d0})}{\rho_l L^* D_0}\right]^2, \tag{5.11}$$

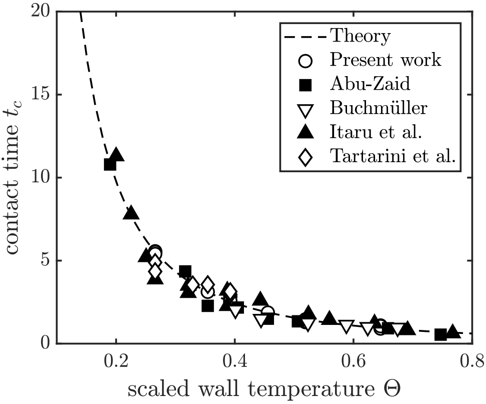

Figure 5.7: Dimensionless contact time of a water drop from the present thesis and existing literature data (Abu-Zaid, 2004; Itaru & Kunihide, 1978; Tartarini et al., 1999; Buchmüller, 2014) as a function of the scaled wall temperature, in comparison with the theoretical prediction (5.12). The initial drop diameter in the experiments ranges from 2.1 to 4.6 mm and the wall materials are polished aluminum, carbon steel, and stainless steel. (Reprinted (adapted) from Breitenbach et al. (2017a), with permission of the American Physical Society. © 2017 American Physical Society.)

for the nucleate boiling regime allows the contact time to be given in dimensionless form:

$$\bar{t}_c = \frac{1}{k_\mathrm{w}^2\,\Theta^2}. \tag{5.12}$$

The contact times from the present thesis and those found in literature from Abu-Zaid (2004), Buchmüller (2014), Itaru & Kunihide (1978), and Tartarini et al. (1999) are compared with the theoretical prediction (5.12) in Fig. 5.7 and Fig. 5.8. The initial drop diameter in the experiments ranges from 2.1 to 4.6 mm for various wall materials. The agreement is good for all the cases. For the data shown in Fig. 5.7 (for ambient pressure conditions) the coefficient $k_\mathrm{w} = 1.6$ is determined by fitting to the experimental data. This parameter is the same for all the substrates used in the experiments, since their wettability properties are similar (Faghri & Zhang, 2006). Noteworthy is the fact, that the estimated value of the coefficient $k_\mathrm{w} = 1.6$ is very close to the value obtained from the experiments.

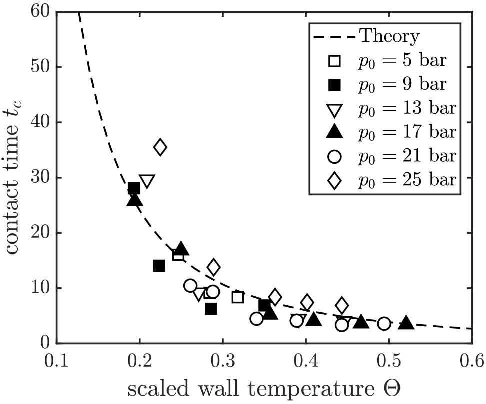

Figure 5.8: Dimensionless contact time of a water drop on aluminum surface at various ambient pressures from Buchmüller (2014) as a function of the scaled wall temperature, in comparison with the theoretical predictions (5.12). The ambient pressure ranges from 5 to 25 bar. (Reprinted (adapted) from Breitenbach et al. (2017a), with permission of the American Physical Society. © 2017 American Physical Society.)

At the elevated pressure conditions shown in Fig. 5.8 the best fit to the experimental data from Buchmüller (2014) yields $k_\mathrm{w} = 1.0$. Some difference between the values of k_w can be caused by the conditions at the target surface (some sediments have been observed in the experiments shown in Buchmüller (2014)) and by the increase of the contact angle with the ambient pressure (Siemons et al., 2006), leading to the decrease of the contact area of the drop.

With Eq. (5.8) and Eq. (5.10) the time averaged heat flux of the drop evaporation can be expressed as:

$$\langle \dot{q} \rangle_c = \frac{24 k_\mathrm{w}\, e_\mathrm{w}^2 \Delta T_\mathrm{w}^2}{\rho_l \pi L^* D_0}. \tag{5.13}$$

Note that the impact velocity is no longer a governing parameter of the heat flux for the drop impact in the in the nucleate boiling regime, in accordance with Eq. (5.10) and the experimental observations shown in Fig. 5.3(b).

Figure 5.9 shows the estimated time averaged heat flux for the data provided in Fig. 5.3(a). This value is important for the development of a spray cooling model in the nucleate boiling regime. In Fig. 5.9 the averaged heat flux is estimated as $\langle \dot{q} \rangle_c = 1/t_c \int_0^{t_c} \dot{q}\, \mathrm{d}t$, where $\dot{q}$ is defined in Eq. (5.8), and

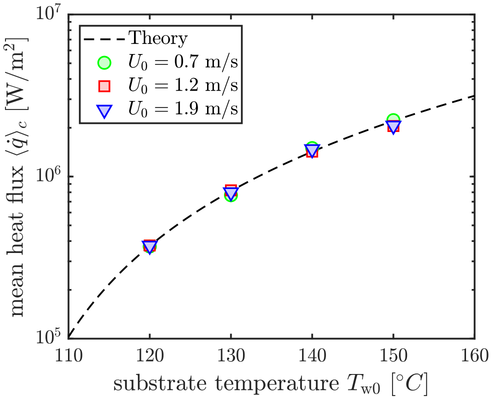

Figure 5.9: Time averaged heat flux for different impact parameters, calculated using the measured contact times. The theoretical prediction (5.13) is also shown for the substrate temperature range from 110 to 160 °C. (Reprinted (adapted) from Breitenbach et al. (2017a), with permission of the American Physical Society. © 2017 American Physical Society.)

the contact time t_c is measured in the experiments for different impact parameters and initial substrate temperatures. Additionally, the theoretical prediction (5.13) is shown to extend the range of the surface temperatures from 110 to 160 °C.

For the drop diameter used in the experiments, the average heat flux is in the range of 10^5 to $2 \times 10^6\,\mathrm{W/m^2}$. In many cases these values are much larger than heat flux densities achieved by steady sprays (Lin & Ponnappan, 2003; Hsieh et al., 2004), because intensive sprays create a continuous water film, which reduces the heat flux density significantly. The ideal spray for cooling purposes can be envisioned for the condition that all the impacting drops have just enough time to evaporate on the wall before the next drop arrives, i.e. all drops impact onto a dry substrate. This means that the wetted surface ratio, $\pi D_0^2 t_c \dot{N} \approx 1$, has to be in the order of unity. Here $\dot{N}$ is the spray number density. The optimum mass flux density of the spray can thus be estimated from

$$j_m \approx \frac{\rho_l D_0}{6\, t_c}. \tag{5.14}$$

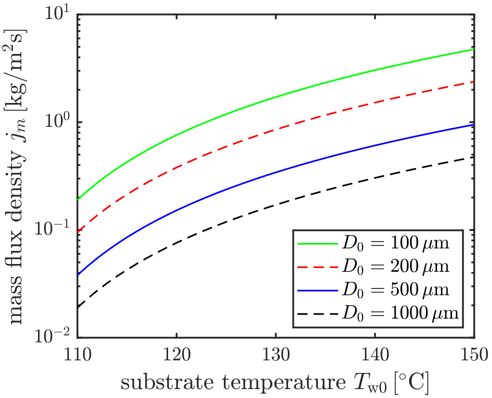

Figure 5.10: Optimum mass flux density in dependency of the initial substrate temperature T_{w0} for various drop diameter D_0 of the spray, calculated with the theoretical prediction (5.14) for a stainless steel surface.

The optimum mass flux density $\dot{m}$ of the spray can be determined using expression (5.12) for the contact time in the nucleate boiling regime. However, practically, such optimal sprays can be applied only for a finite temperature range, since the contact time t_c depends on the substrate temperature. In a first approximation, Fig. 5.10 shows the optimum mass flux density from Eq. 5.14 in dependency of the initial substrate temperature T_{w0} for various drop diameters D_0 of the spray. For polydisperse sprays the mean arithmetic diameter can been used. It is obvious from Fig. 5.10, that high-performance spray cooling in the nucleate boiling regime is quite challenging since there are multiple aspects which have to be taken into account. For instance, since the optimum mass flux density strongly depends on the temperature the flux has to decrease significantly during a cooling cycle. Otherwise the sprays would create a continuous water film on the surface during the cooling cycle. Furthermore a very fine spray has to be choose, since the mass flux densities are quite low for bigger droplets. For a dense spray, however, drop interaction and water film accretion have to be taken into account.

5.2 Thermal atomization regime

Drop impact in the thermal atomization regime results in drop disintegration and the generation of various fine secondary droplets, as already shown in Fig. 3.4(d). Several studies have been performed in the past investigating the drop impact outcome onto very hot substrates (Bertola, 2015; Tran et al., 2012; Staat et al., 2015; Liang et al., 2016) leading to drop breakup and secondary droplets. In many of these studies only the Weber number is used for describing of the outcome and breakup threshold. This results from the assumption that during impact onto very hot substrates contact between the liquid and solid regions is absent and viscous effects are negligibly small.

However, the drop breakup is often accompanied by the generation of multiple secondary droplets. Their characteristics (number, size and velocity) are quite important parameters in numerous industrial processes, *e.g.* internal combustion engines, where they affect mixture formation and coke residues during combustion process. It is known that the surface properties and the impact conditions significantly influence the characteristic size of those secondary droplets and the conditions determining when drop breakup occurs (Cossali et al., 2005; Moreira et al., 2007; Cossali et al., 2008). A comprehensive overview of various studies related to the characterization of secondary atomization during drop impact onto a very hot surfaces can be found in Moreira et al. (2010) and Liang & Mudawar (2017a).

The present section is focused on the mechanisms of thermal atomization of an impacting drop and the characterization of the resulting fine spray of secondary droplets. The fast vertical spray of fine secondary droplets and the final drop disintegration are not induced by inertia, but rather by thermal effects. Only this type of atomization is considered in the present section and for this very reason the regime is called thermal atomization. A typical time of contact is estimated theoretically and introduced as a relevant threshold value bounding thermal atomization and rebound regimes. Additionally, a characterization of secondary droplets generated during the drop impact has been performed, leading to a theoretical model for the secondary droplet velocity over time. Parts of the section have been published in Roisman et al. (2018) and Breitenbach et al. (2018a,b). Furthermore, parts of the experimental investigations have been described in the thesis of Kissing (2017).

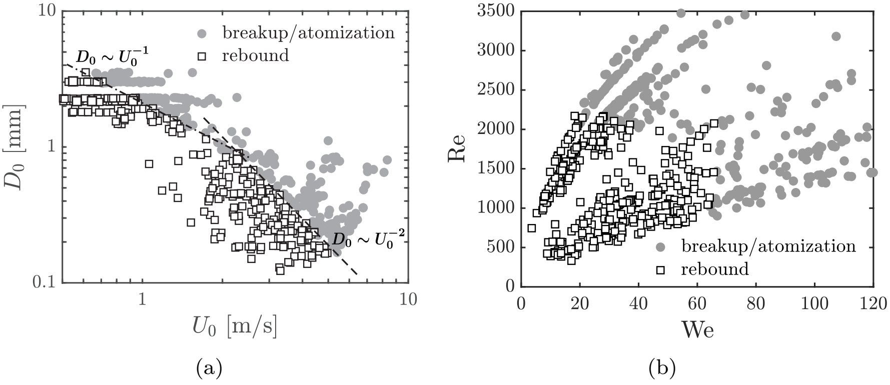

(a) (b)

Figure 5.11: Map of drop impact parameters leading to drop thermal atomization or drop rebound. The wall temperature is the same for all the experiments, $T_{w0} = 250$ °C. The same data are plotted in the form (a) D_0 vs. U_0 and in the form (b) Re vs. We. (Reprinted (adapted) from Roisman et al. (2018), with permission of Cambridge University Press. © 2018 Cambridge University Press.)

5.2.1 Thermal atomization threshold: not described by the Weber number

In order to identify the parameters or dimensionless groups governing the thermal atomization process, a number of experiments have been performed with the same initial wall temperature $T_{w0} = 250\,°\mathrm{C}$ but different drop impact velocities U_0 and diameters D_0. The experimental data is shown in Fig. 5.11. For impact velocities $U_0 < 2\,\mathrm{m/s}$ the critical drop diameter corresponding to the drop atomization is approximately $D_{\mathrm{atom}} \sim U_0^{-1}$. For this threshold the Weber number is not relevant, since inertial forces are very small. This is a very important result, since the Weber number is used rather widely for describing various phenomena arising from drop impact onto a very hot substrate. One of the assumptions leading to the extensive use of the Weber number is that intensive evaporation near the hot substrate prevents direct contact and wetting and therefore the effect of the liquid viscosity is negligibly small. It appears from our results however, that this assumption is not universal.

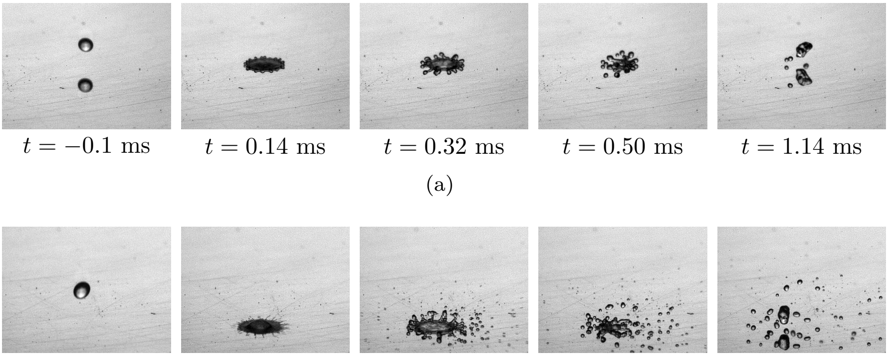

$t = -0.1$ ms $t = 0.14$ ms $t = 0.32$ ms $t = 0.50$ ms $t = 1.14$ ms

(a)

$t = -0.1$ ms $t = 0.04$ ms $t = 0.21$ ms $t = 0.32$ ms $t = 0.65$ ms

(b)

Figure 5.12: Inertia induced rim breakup for high Weber number and small drop diameters: (a) receding breakup, $D_0 = 340\,\mu$m, $U_0 = 4.0\,$m/s, $T_{\mathrm{w}0} = 220\,^\circ$C, and (b) prompt splash combined with receding breakup, $D_0 = 360\,\mu$m, $U_0 = 6.8\,$m/s, $T_{\mathrm{w}0} = 250\,^\circ$C. Thermal effects do not influence the breakup. (Reprinted (adapted) from Roisman et al. (2018), with permission of Cambridge University Press. © 2018 Cambridge University Press.)

For larger impact velocities $U_0 > 2$ m/s where inertial forces begin to dominate, the critical diameter for breakup scales well with $D_{\mathrm{break}} \sim U_0^{-2}$. This result indicates that a critical Weber number can be used for modeling the drop breakup threshold in this regime, but only in this regime.

In summary, the Weber number, which is defined as the ratio of the inertial forces to surface tension, does not account for thermal effects. This parameter can therefore describe only drop breakup governed by inertia. To examine this hypothesis a breakup map has been plotted for drops of diameter much smaller than 1 mm. According to the results shown in Fig. 5.11, these drops atomize at a definite Weber number. They break up due to the rim instabilities during the drop spreading or receding, since the rim receding velocity is higher than the velocity of dewetting. In this regime a prompt splash and a receding breakup can be observed, as shown in Fig. 5.12. The breakup mechanism is very similar to drop receding breakup on hydrophobic substrates (Rioboo et al., 2001), which is often observed on cold substrates. The breakup threshold in these experiments is We = 65. This value is sim-

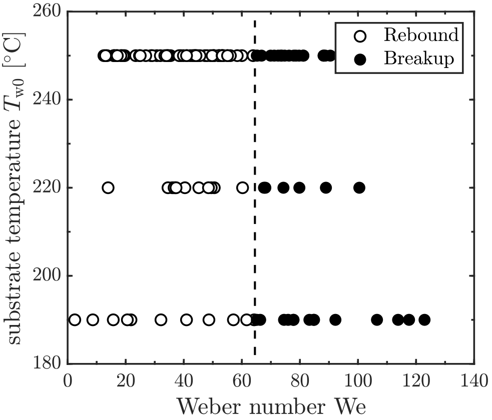

Figure 5.13: Breakup regime map for various substrate temperatures and Weber numbers for drop diameters smaller than 1 mm. The breakup is inertia induced and therefore independent of the surface temperature. (Reprinted (adapted) from Roisman et al. (2018), with permission of Cambridge University Press. © 2018 Cambridge University Press.)

ilar to the breakup threshold of We = 53 in Lv et al. (2016) or We = 90 in Tsai et al. (2009) for impacts onto dry, superhydrophobic substrates at room temperature. Furthermore, for a drop impact onto a hot surface far above the Leidenfrost temperature, Wachters & Westerling (1966) identify a critical threshold We = 80 for a breakup governed by inertia. Since there is no wetting of the spreading droplet with the surface in the film boiling regime, the spreading conditions are similar to those of superhydrophobic substrates.

The regime map, shown in Fig. 5.13, demonstrates that the threshold Weber number for such small drops does not depend on the initial target temperature. This type of drop breakup regime is not considered as thermal drop atomization in the present study.

This difference of the inertial breakup (occurring at the Weber numbers above a certain critical $\mathrm{We}_{\mathrm{crit}}$ value) and thermal atomization (at the Reynolds numbers exceeding a certain critical $\mathrm{Re}_{\mathrm{crit}}$ value), can be clearly seen in Fig. 5.11(b), where the same experimental data are presented as a function of Reynolds number and Weber number. For the specific conditions of shown in Fig. 5.13, the critical Reynolds number is approximately $\mathrm{Re} \approx 2000$.

Our experiments unequivocally show that the Weber number is not an appropriate parameter for quantitatively describing the thermal atomization threshold. The Reynolds number alone also does not capture the thermal effects involved in the impact. In order to predict the thermal atomization threshold the physical processes accompanying thermal atomization have to be considered in more detail and alternative dimensionless numbers for the thermal atomization threshold have to be developed. First suggestions for such new dimensionless numbers will be discussed in the following sections.

5.2.2 Mechanism leading to thermal atomization

Substrate wetting and irregular dewetting

A typical scenario of drop impact in the thermal atomization regime is shown in the top-view time sequence in Fig. 5.14. In all the observed cases an intensive thermal atomization is accompanied by the lamella breakup. The spreading lamella breaks up by an expansion of several holes, nucleated at several points on the lamella periphery where the lamella is at its thinnest. The expansion of the holes is caused mainly by capillary forces (Taylor, 1959), assisted also by the aerodynamic forces associated with the vapor flow from below, induced by intensive evaporation.

Different regions of the lamella are defined in Fig. 5.15. For this sketch a drop image at the instant $t = 2.3\,\mathrm{ms}$ in Fig. 5.14 is used. Drop spreading in the thermal atomization regime is always accompanied by partial lamella detachment and its breakup. Lamella detachment leads to the separation of the lamella region into a wetted lamella region and a free levitated lamella. The wetted region of the spreading lamella is seen as a matt, dark part of the image. This optical effect is caused not only by the contact with the substrate but also by the appearance of a large number of small bubbles, nucleated at the wetted substrate surface. The nucleation of such bubbles and their expansion can be observed on a transparent target, which has been shown in Fig. 5.16.

There is no doubt that the intensive heterogeneous nucleation observed from above as a dark region is a wetted region of the substrate. Such phenomena have been observed in Chaze et al. (2017) using infrared thermography. They have detected a drastic drop of the temperature and an increase

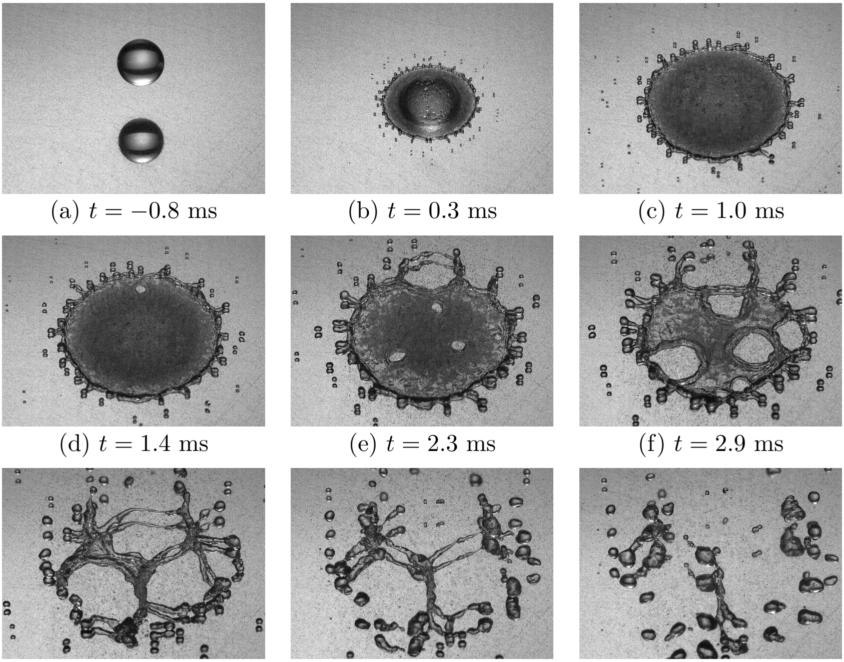

(a) $t = -0.8$ ms (b) $t = 0.3$ ms (c) $t = 1.0$ ms

(d) $t = 1.4$ ms (e) $t = 2.3$ ms (f) $t = 2.9$ ms

(g) $t = 3.7$ ms (h) $t = 4.6$ ms (i) $t = 5.7$ ms

Figure 5.14: Top view of the drop impact onto a hot surface in the thermal atomization regime: the impact parameters are $D_0 = 2.2\,\mathrm{mm}$, $U_0 = 2.5\,\mathrm{m/s}$, and the initial wall temperature $T_{\mathrm{w0}} = 330\,^\circ\mathrm{C}$. (Reprinted (adapted) from Roisman et al. (2018), with permission of Cambridge University Press. © 2018 Cambridge University Press.)

of the heat flux density at the substrate surface on the wetted region, which indicates contact between the superheated liquid and the wall.

Additionally, the extension of the holes within the lamella is not uniform. It can be seen, that the extension of the holes is much higher in the direction to the levitated region, due to no wetting (consequently higher capillary forces) on the levitated region of the cavity rim. These observations support the assumption of a central wetted area.

The evolution of the radius of the wetted spot can be very roughly estimated by measuring the profile of the dark region. The results of these qualitative measurements are illustrated in Fig. 5.17. It is shown that the

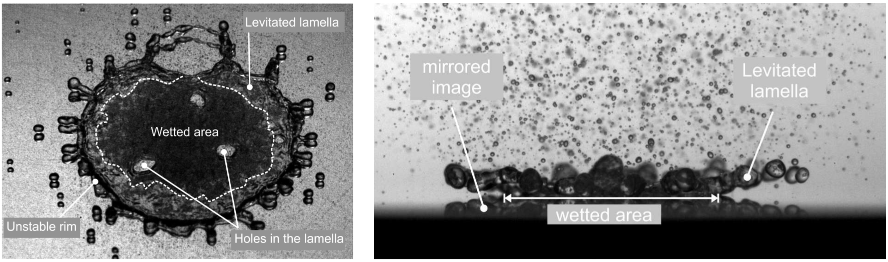

Figure 5.15: Drop spreading and breakup in the atomization regime. In the left image (view of the spreading drop from above) the wetted part of the substrate, where the lamella is in contact with the wall, is a dark region, whereas the light grey region corresponds to the levitated part of the lamella. The wetted part in contact with the wall, and the levitated part of the lamella are clearly seen in the side view (right image). (Reprinted from Roisman et al. (2018), with permission of Cambridge University Press. © 2018 Cambridge University Press.)

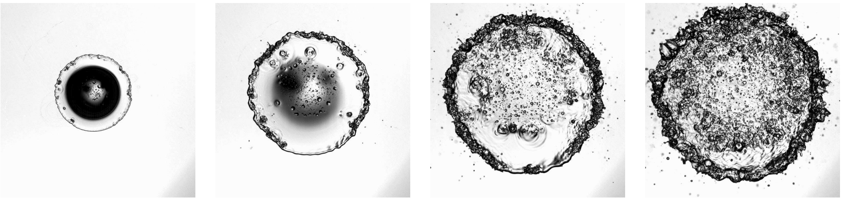

(a) $t = 0.3$ ms (b) $t = 0.8$ ms (c) $t = 1.9$ ms (d) $t = 2.9$ ms

Figure 5.16: Heterogeneous nucleation and fast bubble growth during drop spreading on sapphire glass at the initial wall temperature $T_{\mathrm{w0}} = 190\,^{\circ}\mathrm{C}$. (Reprinted from Roisman et al. (2018), with permission of Cambridge University Press. © 2018 Cambridge University Press.)

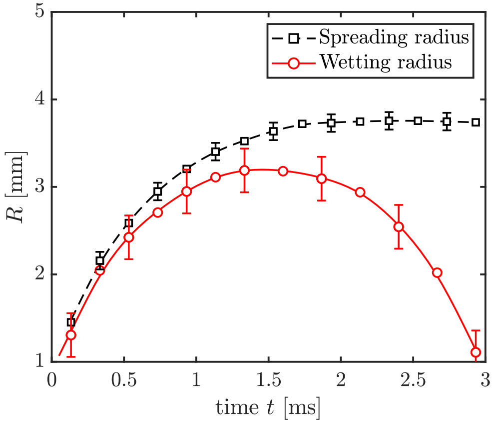

Figure 5.17: Evolution of the average drop spreading radius and of the radius of the wetted region in thermal atomization regime obtained from the images. The error bars indicate the uncertainty of the image analysis. The impact parameters are $D_0 = 2.2\,\mathrm{mm}$, $U_0 = 2.5\,\mathrm{m/s}$, and the initial wall temperature $T_{\mathrm{w}0} = 330\,^\circ\mathrm{C}$.

the radius initially increases after drop impact. This is caused by the increase of the region of high pressure of the order of $p \sim \rho_l U_0^2$, produced by the impacting drop (Roisman, 2009). This pressure rapidly reduces in time and at large times after impact, quickly approaches the outer pressure. Starting at these times the dewetting process is possible. The radius of the dark region during spreading is always slightly smaller than the spreading radius. This is explained by the delay time for bubble creation during heterogeneous nucleation (Carey, 1992).

Lamella levitation: contact time of an impacting drop

In the wetted region a viscous boundary layer develops, leading to the thickening of the lamella. When the thickness of the viscous boundary layer equals the thickness of the lamella, the spreading is strongly damped by viscosity (Roisman, 2009). If the Reynolds number $\mathrm{Re} = U_0 D_0/\nu_0$ is defined on the basis of the viscosity at room temperature ν_0, the residual lamella thickness h_{res} in the wetted region is estimated from Roisman (2009)

$$h_{\mathrm{res}} \approx 0.79 D_0 (\nu/\nu_0)^{2/5} \mathrm{Re}^{-2/5}, \tag{5.15}$$

where ν is the kinematic viscosity of the heated liquid. The thickness of thermal boundary layer in the liquid can be estimated as $\delta_l \approx k_l\sqrt{\alpha_l t}$, where k_l is a dimensionless constant of order of unity. At the initial stages the heat flux from the hot substrate goes mainly into the heating of the liquid in the expanding thermal boundary layer. At some time instant the thermal boundary layer reaches the free surface of the lamella, leading to its fast heating and initiation of intensive evaporation. The heat flux in the liquid region quickly reduces, since the heat exchange between the free surface of the lamella with the surrounding gas is relatively small. In this region most of the heat from the substrate goes towards the liquid evaporation. The bubbles grow much faster and coalesce, forming a continuous vapor layer between the spreading lamella and the substrate. As a result the outer part of the lamella levitates. Further reasons for the lamella levitation are possible Marangoni effects. The surface tension jumps rapidly from its high values, corresponding to those at room temperature at the central, thicker regions of the lamella, to low values at the remote thin regions of the lamella, which are much hotter. In consequence, Marangoni effects, in combination to the intensive evaporation, lead to the detachment of the spreading lamella near the edge, which is schematically shown in Fig. 5.18.

As can be seen in Fig. 5.15(a), the boundary between the central wetted region and the levitated region of the lamella is not smooth. This shape is a result of the unstable evaporation of a superheated liquid in the lamella, similar to corresponding observations in van Limbeek et al. (2016) and Khavari et al. (2015).

The substrate temperature at the dewetting front approaches the saturation temperature since it is in contact with the moving evaporating liquid/vapor interface. Therefore, the heat flux in this region is maximal. This effect leads to very intensive evaporation, leading to the generation of small bubbles in the lamella and a subsequent spray of fine secondary droplets. This phenomena has been observed in Cossali et al. (2005).

The phenomenon of liquid film detachment and levitation on a very hot surface is not new. Expansion of a wetted region during stationary liquid jet impact onto very hot surfaces has been observed in Piggott et al. (1976); Hammad et al. (2004) and Karwa et al. (2011). In these experiments the expansion of the wetting front has been observed with a relatively slow velocity of millimeters per seconds. The propagation is caused by the local

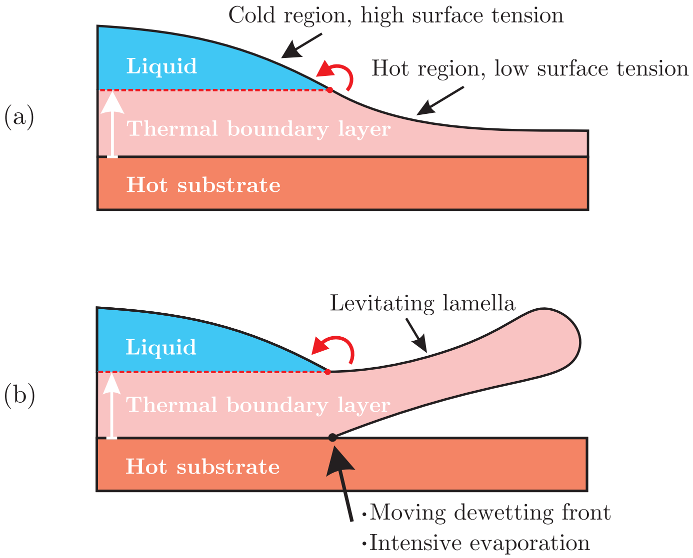

Figure 5.18: Schematic sketch of the levitation phenomena: Marangoni effects, in combination to intensive evaporation near the dewetting front lead to the detachment of the spreading lamella.

substrate cooling in the wetted region. Aktershev & Ovchinnikov (2011) studied experimentally and modeled theoretically intensive dewetting of a heated substrate caused by the dynamic effects associated with the pressure in a bubble created on the substrate due to evaporation.

To characterize the velocity of the dewetting in the present experiments, the contact time of a spreading drop is measured. The contact time of the drop on the substrate corresponds to the instant when the entire lamella detaches from the wall surface. As shown in Fig. 5.19(a) and (b), the contact time does not depend strongly on the initial wall temperature, but is determined by the Reynolds number $\mathrm{Re} = D_0 U_0/\nu_0$. The best fit of the experimental data yields $t_c \sim \mathrm{Re}^{-0.79}$ for the drop contact time.

This time differs from the typical time $t_\sigma \sim \sqrt{D_0^3 \rho_l/\sigma}$ of capillary oscillations which does not depend on the impact velocity and is often used for the description of the time of drop deformation caused by collision (Willis & Orme, 2000).

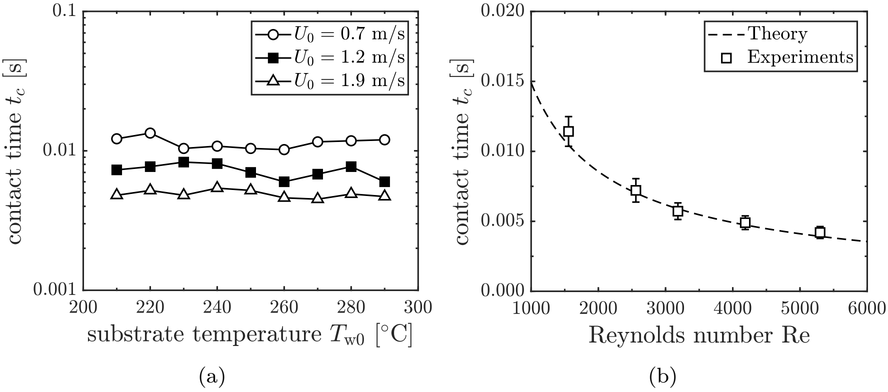

Figure 5.19: Contact times t_c for impinging drops onto a hot wall for thermal atomization and rebound regimes: (a) for various initial wall temperatures and (b) averaged values (for various temperatures) as a function of the impact Reynolds number in comparison with the theoretical prediction (5.17) with $k_l = 1.0$ (dashed line). The error bars indicate standard deviation of the averaged values. Drop diameter is $D_0 = 2.2$ mm. Reynolds number is based on the liquid viscosity at the room temperature. (Reprinted from Roisman et al. (2018), with permission of Cambridge University Press. © 2018 Cambridge University Press.)

Since the lamella levitation is associated with the growth of the thermal boundary layer within the lamella, the entire lamella has to be detached when the thermal boundary layer reaches the top of the free surface of the lamella. Equating the residual lamella thickness with the thickness of thermal boundary layer

$$h_{\mathrm{res}} \sim \delta_l, \tag{5.16}$$

yields a theoretical estimation of the contact time

$$t_c = \frac{0.6 D_0^2}{k_l^2 \alpha_l \mathrm{Re}^{4/5}} \frac{\nu^{4/5}}{\nu_0^{4/5}}. \tag{5.17}$$

The value of $\nu^{4/5}/\alpha_l \approx 20.0\ \mathrm{s}^{1/5}\mathrm{m}^{-2/5}$ depends only very weakly on the temperature of superheated water. The power of the Reynolds number $-4/5$ estimated in Eq. (5.17) is very close to the experimentally determined power,

-0.79. The predictions for the contact time are compared with the experimental data in Fig. 5.19(b) for $k_l = 1.0$. The fact that the k_l-value is comparable with unity confirms the main physical assumptions used above to explain the mechanism of drop detachment.

The evolution of the wetting radius can be predicted if the evolution of the lamella thickness is known. It is known that in the case of high Reynolds and high Weber number impacts the dimensionless lamella thickness is universal (Roisman et al., 2009). The observed evolution of the lamella profile can be approximated by

$$\bar{h}_l = \frac{0.39}{(\bar{t}+0.25)^2} \exp\left[-\frac{2.34\bar{R}^2}{(\bar{t}+0.25)^2}\right], \tag{5.18}$$

with

$$\bar{h}_l \equiv \frac{h_l}{D_0}, \quad \bar{R} \equiv \frac{R}{D_0}, \quad \bar{t} \equiv \frac{tU_0}{D_0}. \tag{5.19}$$

Equating the lamella thickness with the thickness of the thermal boundary layer yields an expression for the radius of the wetted spot

$$\bar{R}_{\text{wet}} \approx 0.65(\bar{t}+0.25)\sqrt{\ln\left[\frac{\sqrt{\bar{t}_c}(\bar{t}_c+0.25)^2}{\sqrt{\bar{t}}(\bar{t}+0.25)^2}\right]}. \tag{5.20}$$

The predicted value of the dimensionless wetted radius $\bar{R}_{\text{wet}}$ is compared in Fig. 5.20. The agreement between theory and experiment is rather good, which further confirms the hypothesis about the mechanism of dewetting governed by the propagation of the thermal boundary layer and its interaction with the free surface of the spreading lamella.

Parameters influencing the atomization threshold

A dimensionless number, characterising the thermal atomization regime, can be defined as $\mathscr{R} \sim t_c U_0/D_0$, which is the ratio of the contact time t_c, defined in Eq. (5.17), to the typical drop spreading time:

$$\mathscr{R} = \text{Pr}_l\,\text{Re}_H^{1/5}, \quad \text{Re}_H \equiv \frac{D_0 U_0}{\nu}, \quad \text{Pr}_l \equiv \frac{\nu}{\alpha_l}, \tag{5.21}$$

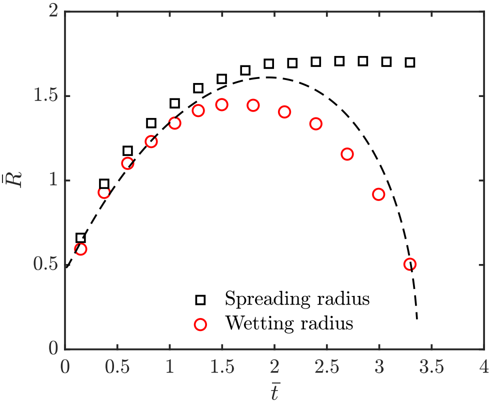

Figure 5.20: Evolution of the average dimensionless drop spreading radius and of the radius of the wetted region in thermal atomization regime in comparison to the theoretically predicted values from Eq. (5.20).The impact parameters are $D_0 = 2.2\,\mathrm{mm}$, $U_0 = 2.5\,\mathrm{m/s}$, and the initial wall temperature $T_{\mathrm{w}0} = 330\,^\circ\mathrm{C}$. (Reprinted (adapted) from Roisman et al. (2018), with permission of Cambridge University Press. © 2018 Cambridge University Press.)

where the Reynolds number Re_H is based on the viscosity of the hot liquid and Pr_l is the Prandtl number. As previously shown in Fig. 5.11, the threshold for thermal atomization is $\mathscr{R} \approx 5.8$ for $T_{\mathrm{w}0} = 250\,^\circ\mathrm{C}$. Since for superheated water the variation of the term $\nu^{4/5}/\alpha_l$ is weak, the dimensionless number can be scaled as $\mathscr{R} \sim D_0^{1/5} U_0^{1/5}$.

The regime maps existing in the literature are influenced significantly by the substrate properties. Comparison of the maps in Bertola (2015) and Tran et al. (2012) leads to the conclusion that the temperature alone cannot describe the threshold, even for the same liquid on different surfaces. The main parameter governing the phenomenon of drop vaporization and possible atomization is the characteristic heat flux. At the contact line, i.e. the region of intensive evaporation, the substrate temperature is close to the saturation temperature. The heat flux between the wall and the spreading drop occurs mainly in the expanding thermal boundary layers, whose thickness increases as the square root of time. The solution for heat transfer in such systems is well-known (Roisman, 2010). Heat conduction in the solid wall is described by an expanding thermal boundary layer near the wall surface. The char-

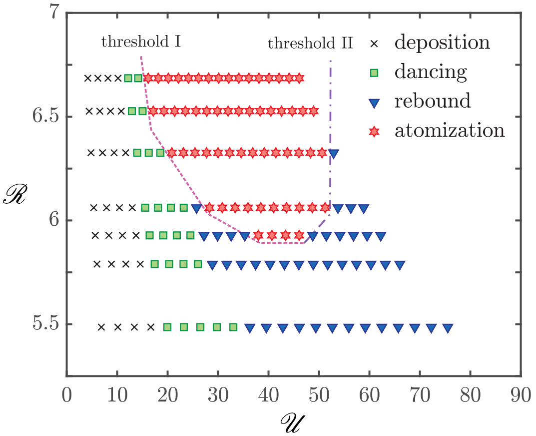

Figure 5.21: Regime map for the dimensionless contact time $\mathscr{R}$ and dimensionless heat flux $\mathscr{U}$ of a drop. (Reprinted from Roisman et al. (2018), with permission of Cambridge University Press. © 2018 Cambridge University Press.)

acteristic heat flux associated with vaporization is expressed for the typical time of drop impact $t_i = D_0/U_0$ in the form

$$\langle \dot{q} \rangle = \frac{e_\mathrm{w}(T_\mathrm{w0} - T_\mathrm{sat})}{\sqrt{t_i}} = \frac{e_\mathrm{w}(T_\mathrm{w0} - T_\mathrm{sat})\sqrt{U_0}}{\sqrt{D_0}}, \tag{5.22}$$

The ratio of the drop impact velocity and the velocity associated with the drop vaporization is

$$\mathscr{U} = \frac{\langle \dot{q} \rangle}{\rho_\mathrm{v} L U_0} = \frac{e_\mathrm{w}(T_\mathrm{w0} - T_\mathrm{sat})}{\rho_\mathrm{v} L \sqrt{D_0 U_0}}, \tag{5.23}$$

where L is the latent heat of evaporation and ρ_v is the density of the water vapor.

A final regime map for different initial values of the dimensionless heat flux $\mathscr{U}$ and the dimensionless contact time $\mathscr{R}$ is shown in Fig. 5.21. It should be noted that experimental data for drop atomization from Bertola (2015) also coincide with the results presented in Fig. 5.21. Two branches of the atomization threshold can be identified in Fig. 5.21. They are illustrated by the curves *threshold I* and *threshold II*. At lower substrate temperatures (lower values of $\mathscr{U}$) the threshold impact velocity, leading to thermal atomization, reduces if the wall temperature increases. This is an expected result. The characteristic time of lamella breakup t_{break} reduces at higher substrate temperatures. The curve *threshold I* corresponds to the situation when t_{break} is equal to the contact time. The impact velocity corresponding to the *threshold II* surprisingly increases when the substrate temperature is higher. This transition is probably associated with such intensive evaporation that the dynamic pressure in the vapor flow is comparable with the dynamic pressure produced by drop impact. Such vapor flow therefore prevents the expansion of the wetted spot even at the initial stages of drop impact and spreading.

5.2.3 Characterization of the secondary atomization

Detailed side-view images of drop atomization and spray generation are shown in Fig. 5.22 for different time instants. It can be seen, that in the first initial moment of drop impact, even far before the spreading of the drop is finished, first secondary droplets arise from the outer lamella between the portion of the initial drop that is not fully spread and the rim. For time instances from $t = 1\,\mathrm{ms}$ onwards, the region of the lamella where secondary droplets are ejected from, enlarges to the center of the impact spot while the location of the highest droplet ejection rate shifts towards the center. From $t > 3\,\mathrm{ms}$ the production of fine secondary droplets ejected in axial direction suddenly stops in the region of the levitating lamella and the outer rim forms finger-like jets. Furthermore, the jets start to disintegrate and form very large drop fragments. The overall generation of secondary droplets from the lamella stops as soon as the dewetting is complete and the entire lamella is detached. At $t = 8\,\mathrm{ms}$ after initial contact between the drop and the surface, the drop fragments are separated and hover in the air, slightly oscillating above the impact spot. Simultaneously a mist consisting of very fine secondary droplets circulates toroidally above the large fragments.

To characterize the fast vertical spray of fine secondary droplets a dual-mode phase Doppler measurement system has been used. Since the phase Doppler system is a pointwise measurement technique three different radial positions r, all with an axial position $z = 4\,\mathrm{mm}$ above the impact surface, have been measured to describe various regions: center of the lamella $r_1 = 0\,\mathrm{mm}$, rim region $r_3 = 6\,\mathrm{mm}$, and between the center and the rim $r_2 = 2\,\mathrm{mm}$. The positions are fixed for all measurements due to the highly

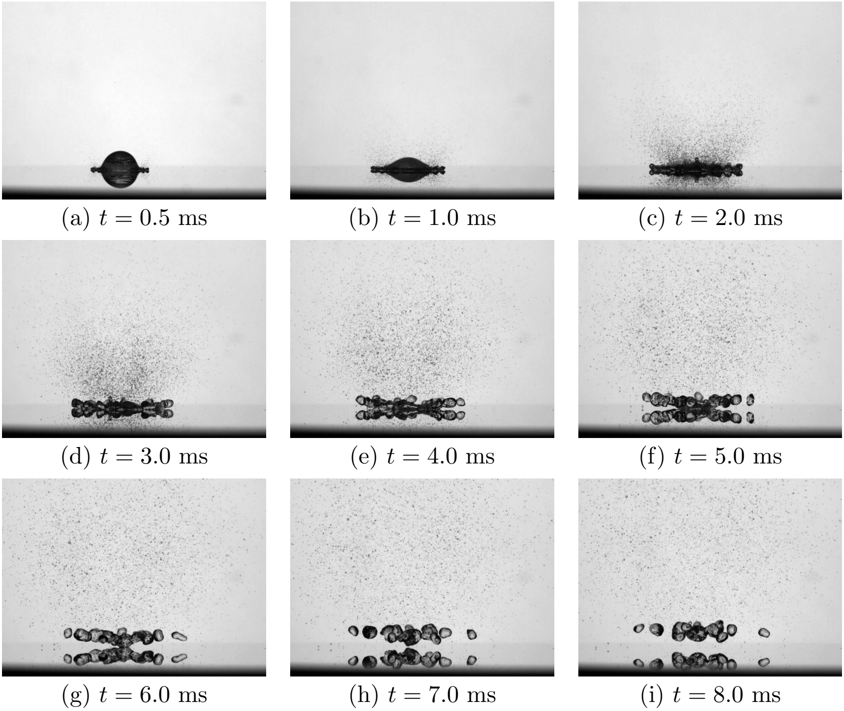
(a) $t = 0.5$ ms (b) $t = 1.0$ ms (c) $t = 2.0$ ms
(d) $t = 3.0$ ms (e) $t = 4.0$ ms (f) $t = 5.0$ ms
(g) $t = 6.0$ ms (h) $t = 7.0$ ms (i) $t = 8.0$ ms

Figure 5.22: Side-view images of the drop impact onto a hot surface in thermal atomization regime at different time instants. The parameters are initial drop diameter $D_0 = 2.2\,\mathrm{mm}$, impact velocity $U_0 = 1.5\,\mathrm{m/s}$, and initial wall temperature $T_{\mathrm{w0}} = 300\,^\circ\mathrm{C}$. (Reprinted from Breitenbach et al. (2018a). © 2018 Elsevier.)

dynamic motion of the spreading drop. Figure 5.23 shows a sketch of the different measurement positions. The phase Doppler system is carefully aligned to achieve reliable results. In the measurements shown in the present thesis the validation ratios are always $> 70\%$.

A global drop size and velocity magnitude distribution of the detected secondary droplets during the first 15 ms after impact is shown in Fig. 5.24(a) and (b) for the drop diameter $D_0 = 2.2\,\mathrm{mm}$, impact velocity $U_0 = 1.5\,\mathrm{m/s}$ and substrate temperature $T_{\mathrm{w0}} = 300\,^\circ\mathrm{C}$. These distributions have been calculated according to the DIN SPEC 91325 (2015) from the three different single measurement positions r_1, r_2, and r_3. For the case illustrated in Fig. 5.24,

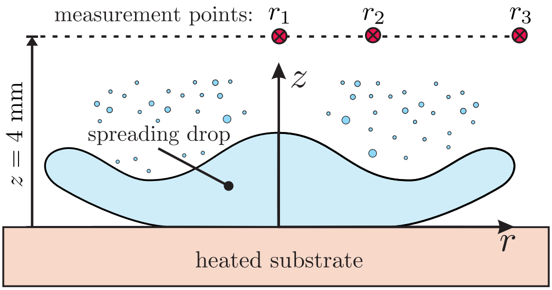

Figure 5.23: Sketch of phase Doppler measurement positions. (Reprinted from Breitenbach et al. (2018a). © 2018 Elsevier.)

the arithmetic mean diameter of the secondary droplets is $d_{10} = 26.1\,\mu$m and the Sauter mean diameter is $d_{32} = 43.6\,\mu$m. It can be seen that the characteristic size of the fine secondary spray is in the region of some tens of microns, while droplets bigger than $d > 80\ \mu$m are very rare. This is in good agreement with prior studies (Cossali et al., 2005; Moreira et al., 2007). Nonetheless, correlations for the Sauter mean diameter shown in Moreira et al. (2010) or Liang & Mudawar (2017a) overpredict the measured value for the Sauter mean diameter.

However, the reason for this is quite simple: compared to previous studies, the few and large drop fragments formed as a result of the drop disintegration and the rim breakup are not considered in the characterization. Therefore, the mean and the Sauter mean diameter as well as the counts shown in the present work are only determined for the dense vertical spray of fine secondary droplets. Moreover, it has to be noted that the phase Doppler system can measure only spherical droplets, so larger, non-spherical droplets will not be detected with the system.

The magnitude of the mean velocity yields $|\vec{u}|_{\mathrm{mean}} = 2.34\,$m/s for the fast vertical spray, but the velocity span extends over a wide range and a maximum velocity of $|\vec{u}| \gtrsim 12\,$m/s has been observed. Figure 5.25 shows a vector plot and a corresponding contour plot of the velocity magnitude of the secondary spray at the time instant $t \approx 4.5\,$ms after drop impact. The data has been obtained by PIV (particle image velocimetry) post-processing of the recorded side-view video data. It can be seen, that the main velocity com-

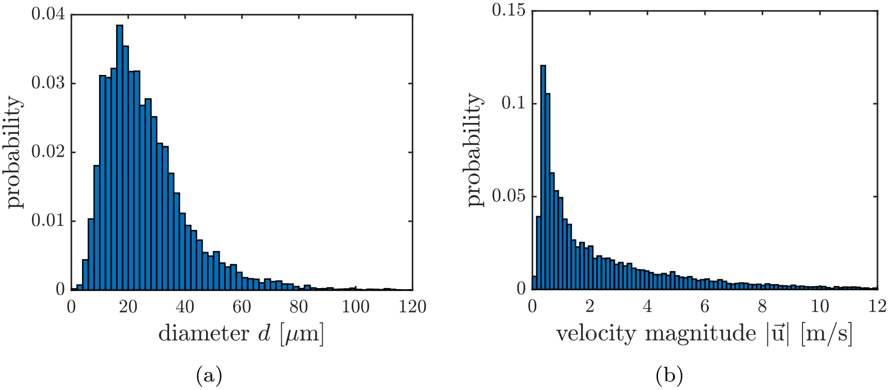

Figure 5.24: Secondary droplets generated during thermal atomization in the first 15 ms after impact: (a) global drop size distribution and (b) global velocity magnitude distribution. The impact parameters are $D_0 = 2.2\,\text{mm}$, $U_0 = 1.5\,\text{m/s}$ with the initial wall temperature $T_{\text{w0}} = 300\,^\circ\text{C}$. (Reprinted (adapted) from Breitenbach et al. (2018a). © 2018 Elsevier.)

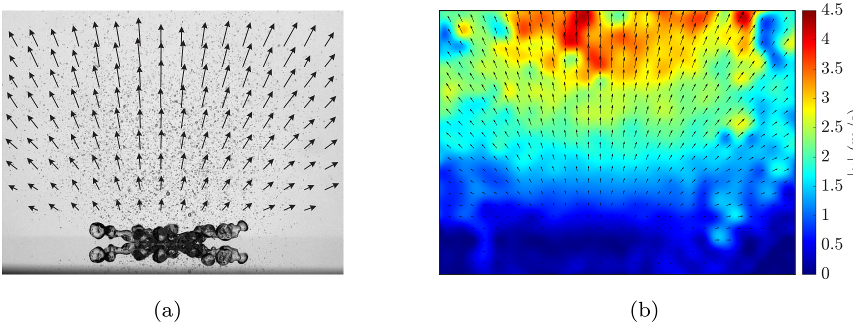

Figure 5.25: (a) Vector plot and (b) the corresponding contour plot of velocity magnitude of the secondary spray at $t \approx 4.5\,\text{ms}$ after drop impact. The length of the vectors are length represent the values. The data has been obtained by PIV (Particle image velocimetry) post-processing of the recorded side-view video data. The impact parameters are $D_0 = 2.2\,\text{mm}$, $U_0 = 1.5\,\text{m/s}$ with the initial wall temperature $T_{\text{w0}} = 300\,^\circ\text{C}$.

ponent of the secondary spray is in the positive z-direction (c.f. Fig. 5.23). Furthermore, the impact velocity decreases over time, since the droplets far from the substrate are much faster compared to droplets which just started.

Spray density and droplet size

In Fig. 5.26(a) the relative counts of the detected secondary droplets for the three measured radial positions are shown as a function of time. The value of the relative counts is related to the number flux density and the detection volume (probe volume) of the phase Doppler instrument. It is determined by the detected counts of each measurement and finally normalized with the maximum number of total counts detected in the measurement for the radial position $r_1 = 0\,\mathrm{mm}$.

The majority of secondary droplets are generated within the thin lamella $r \approx 0 - 4\,\mathrm{mm}$ during the first milliseconds, and the number of counts sharply decreases for $r_3 = 6\,\mathrm{mm}$ as well as for later time instants. This is consistent with the hypotheses of lamella dewetting, characterized by intensive evaporation and consequently by the fact that the heat flux density $\dot{q}(t) \sim t^{-0.5}$ reduces sharply at later time instants. Furthermore, the generation of secondary droplets within the levitating lamella stops as soon as the dewetting of the lamella is complete at $t \approx 7\,\mathrm{ms}$. Some more droplets are still detected after the dewetting is completed, as a consequence of the axial position of the measurement volume and the resulting time delay until the droplets reach the detection volume. It can also be seen in Fig. 5.26(a), that during drop spreading the first secondary droplets arise from the outer lamella $r_2 = 2\,\mathrm{mm}$ between the portion of the initial drop (that is not yet spread) and the rim. In this region the lamella is at its thinnest (Roisman, 2009). At further moments, the region where secondary droplets are ejected from enlarges to the center of the lamella, since the dewetting front moves towards it.

In Fig. 5.26(b) the mean diameter d_{10} is shown as a function of time. Each data point for the mean diameter is calculated for a set of $n = 350$ detected droplets. Therefore, the number of dots and their horizontal spacing are indicators for the counts of secondary droplets. It is obvious that the time-dependent mean diameter as well the counts are almost equal for the positions r_1 and r_2 within the lamella. Only in the rim region at r_3 does the mean diameter increase, while the data rate is considerably lower. Up to the rim

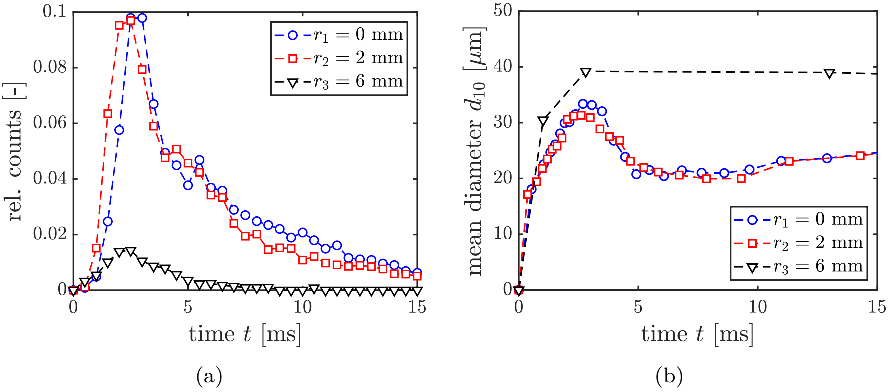

(a) (b)

Figure 5.26: Secondary droplets generated during thermal atomization in the first 15 ms after impact for various radial positions: (a) relative counts of the measured droplets as a function of time and the (b) corresponding mean diameter. Each data point for the mean diameter is calculated for a set of $n = 350$ detected droplets. The impact parameters are $D_0 = 2.2$ mm, $U_0 = 1.5$ m/s, and the initial wall temperature $T_{w0} = 300\,°$C. (Reprinted (adapted) from Breitenbach et al. (2018a). © 2018 Elsevier.)

region r_3, the evolution of the curves exhibit a peak in the first first few milliseconds before approaching a minimum and leveling again to their final overall mean diameter. This overall trend has been reported before (Moita & Moreira, 2009; Cossali et al., 2008). For the thermal atomization regime, this behavior is typical for the region above the lamella and has been observed for all investigated cases.

In Fig. 5.27(a) and (b) the mean diameter d_{10} measured at the center r_1 is shown as a function of time for various wall temperatures and impact velocities. Again, each data point for the mean diameter is calculated for a set of $n = 350$ detected droplets. Correspondingly, Table 5.1 summarizes the final overall mean diameter d_{10} and Sauter mean diameter d_{32} for each case. Again, and as already discussed in the previous section, the Sauter mean diameter is much smaller compared to previous studies for high temperature drop impacts (Cossali et al., 2005; Moita & Moreira, 2009; Moreira et al., 2007).

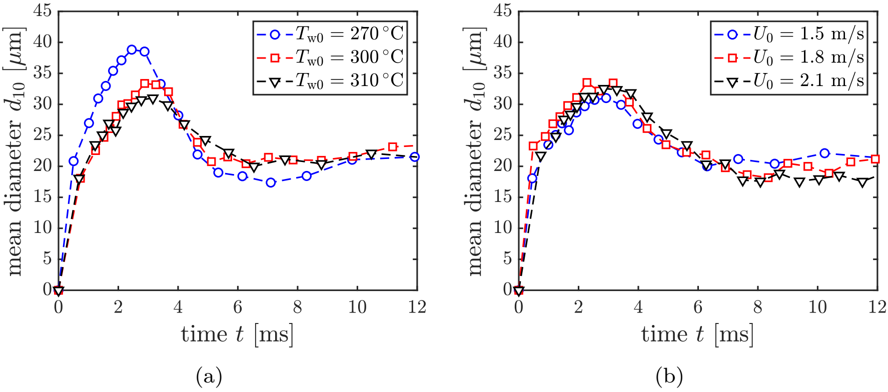

Figure 5.27: Secondary droplets generated during thermal atomization in the first 12 ms after impact at the center r_1: mean diameter as a function of time for (a) various initial substrate temperatures and (b) various impact velocities. Each data point for the mean diameter is calculated for a set of $n = 350$ detected droplets. Further parameters are for (a) $D_0 = 2.2$ mm, $U_0 = 1.5$ m/s and for (b) $D_0 = 2.2$ mm, $T_{w0} = 310$ °C. (Reprinted (adapted) from Breitenbach et al. (2018a). © 2018 Elsevier.)

As shown in Fig. 5.27(a), for various wall temperatures the data rate is roughly the same and only for the lowest surface temperature it slightly decreases. In all cases shown in Fig. 5.27(a), the detected counts decrease considerably after the first few milliseconds. The main differences in the data can be seen in the evolution of the mean diameter and the result of the final overall Sauter mean diameter, which decreases more than 20% in contrast to the value obtained at the lowest temperature. Furthermore, the first peak is less dominant for higher surface temperatures, while for later instants the characteristic size of the droplets is almost the same. For the different cases it can be concluded that the decline of the first peak is the relevant factor for the decrease of the final overall mean and Sauter mean diameter. A reason for the decrease of the characteristic size is the increase of the vapor velocity due to higher surface temperatures. During the atomization process the kinetic energy of the vapor is transferred to the surface energy of the resulting drops. Therefore, the increase of the vapor velocity allows to obtain a larger number of drops from the same volume, but of smaller diameter.

Table 5.1: Final overall mean diameter and Sauter mean diameter of all detected secondary droplets within 15 milliseconds after drop impact in the thermal atomization regime for (a) for various wall temperatures with a constant impact velocity $U_0 = 1.5\,\mathrm{m/s}$ and for (b) various impact velocities with a constant wall temperature $T_{\mathrm{w0}} = 310\,^\circ\mathrm{C}$. (Reprinted from Breitenbach et al. (2018a). © 2018 Elsevier.)

(a)

d_{ij} [μm]	$T_{\mathrm{w0}} = 270\,^\circ\mathrm{C}$	$T_{\mathrm{w0}} = 300\,^\circ\mathrm{C}$	$T_{\mathrm{w0}} = 310\,^\circ\mathrm{C}$
d_{10}	27.05	25.28	24.84
d_{32}	51.45	44.92	40.22

(b)

d_{ij} [μm]	$U_0 = 1.5\,\mathrm{m/s}$	$U_0 = 1.8\,\mathrm{m/s}$	$U_0 = 2.1\,\mathrm{m/s}$
d_{10}	24.84	24.17	23.58
d_{32}	40.22	43.41	43.61

The effect of variation of the impact velocity on the data count is shown in Fig. 5.27(b). No influence of the impact velocity on the mean diameter has been observed. This conclusion is supported by the data in Table 5.1(b) for the overall mean and Sauter mean diameter. Only the data rate increases slightly for an increasing impact velocity. This result indicates that thermal effects during drop contact with the wall are the main factors determining the properties of secondary spray. The effect of the flow in the spreading drop is negligibly small.

Velocity of the secondary drops

The distribution of the velocity magnitude of secondary drops has been already shown in Fig. 5.24(b), with an arithmetic mean value of the velocity magnitude of $|\vec{u}|_{\mathrm{mean}} = 2.34\,\mathrm{m/s}$. However, the figure clearly shows that velocity span extends over a wide range. A closer look into Fig. 5.28 reveals that the high velocity droplets arise only during the first instants of drop impact. At later time instants the velocity magnitude decreases significantly.

This has been already pointed out in Fig. 5.25(b) by the contour plot of the velocity. Therefore, the mean velocity should be as seen time average value and for a comprehensive analysis the velocity over time has to be considered.

It is assumed that the secondary droplets are driven by the stream of the vapor generated during evaporation of the liquid near the dewetting front. The velocity of the secondary droplets u_d can be calculated by Bernoulli's equation from the vapor flow velocity, similar to analysis for droplet-air collision (Opfer et al., 2014). It can be thus scaled as

$$u_d \sim \frac{\sqrt{\rho_\mathrm{v}}}{\sqrt{\rho_l}} u_\mathrm{v}, \tag{5.24}$$

where ρ_v and ρ_l is the water vapor and water liquid density. The vapor flow velocity near the dewetting front yields

$$u_\mathrm{v}(t) \ \sim \frac{\dot{q}(t)}{\rho_\mathrm{v} L}. \tag{5.25}$$

Here L is the latent heat of evaporation, and $\dot{q}(t)$ is the characteristic heat flux associated with vaporization at liquid/solid interface. Assuming the heat conduction in the solid wall is described by an expanding thermal boundary layer near the wall surface (Roisman, 2010) the characteristic heat flux is determined by

$$\dot{q}(t) = \frac{e_\mathrm{w} \Delta T_\mathrm{w}}{\sqrt{\pi}\sqrt{t}}. \tag{5.26}$$

Here e_w is the thermal effusivity of the solid and $\Delta T_\mathrm{w} = T_\mathrm{w0} - T_\mathrm{sat}$ is the overall temperature difference in the wall. The substrate temperature at the solid/liquid interface near the wetting front approaches the saturation temperature T_sat, since it is in contact with the moving evaporating liquid/vapor interface.

With Eq. (5.24), Eq. (5.25) and Eq. (5.26) the theoretical velocity of the secondary droplets detected by the phase Doppler measurement system becomes

$$u_d(t) \approx k_d \frac{e_\mathrm{w}\left(T_\mathrm{w0} - T_\mathrm{sat}\right)}{\sqrt{\rho_\mathrm{v}}\sqrt{\rho_l} L \sqrt{\pi}\sqrt{t - \tau(t)}}, \tag{5.27}$$

where k_d is an adjustable coefficient which can be obtained by fitting the experimental data. It is important that the value of k_d is in order of unity, which indicates that the main physical mechanisms are well described in

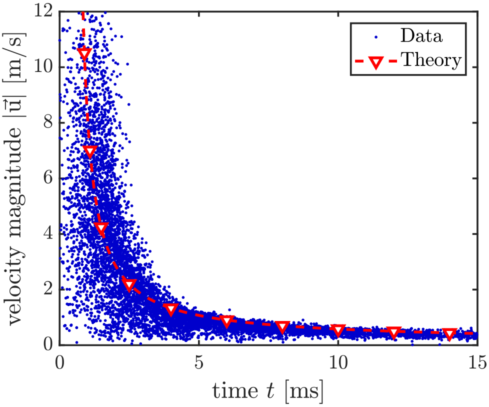

Figure 5.28: Secondary droplets measured at the center of the lamella ($r = 0\,\mathrm{mm}$) generated in thermal atomization regime during the first 15 ms after impact: velocity magnitude of the measured droplets as a function of the time in comparison with the theoretical prediction (5.27). The impact parameters are $D_0 = 2.2\,\mathrm{mm}$, $U_0 = 1.48\,\mathrm{m/s}$, and the initial wall temperature $T_{\mathrm{w0}} = 300\,°\mathrm{C}$. (Reprinted (adapted) from Breitenbach et al. (2018a). © 2018 Elsevier.)

the analysis. The coefficient $\tau(t) = \Delta z/u_d$ accounts for the axial position $\Delta z = 4\,\mathrm{mm}$ of the measurement volume above the impact surface and the resulting time delay in the data acquisition (c.f. Fig. 5.23).

As seen in Fig. 5.28, with $k_d = 0.9$ the theoretical model (5.27) is in excellent agreement with the experimental data for the velocity magnitude. The impact parameters of the data are $D_0 = 2.2\,\mathrm{mm}$ for drop diameter, $U_0 = 1.5\,\mathrm{m/s}$ for impact velocity, and $T_{\mathrm{w0}} = 300\,°\mathrm{C}$ for the initial wall temperature. It is obvious that the velocity of the secondary droplets is well expressed by the theoretical vapor velocity at the solid/liquid interface with a scaling of $u_d(t) \sim t^{-0.5}$.

5.3 Film boiling regime

The drop impact in the film boiling regime has been investigated rather intensive in the past decades (Wachters & Westerling, 1966; Ueda et al., 1979; Yao & Cai, 1988; Chandra & Avedisian, 1991; Bertola, 2009). However, some questions and dependencies still remain unclear and mainly empirical correlations can be found in literature.

The main subject of the present section is the introduction of a predictive theoretical model for heat transfer during drop impact in the film boiling regime. It allows the estimation of the heat collected by an impinging drop during spreading and receding and it accounts for the main physical phenomena. Parts of the section have been published in Breitenbach et al. (2017b, 2018b). Furthermore, parts of the experimental investigations have been supported by the work of Schmidt (2018).

5.3.1 Observations

The drop impact in the film boiling regime at a surface temperature of $T_{\mathrm{w0}} = 330\,^{\circ}\mathrm{C}$ is shown in Fig. 5.29. After the impact the drop first spreads ($t = 1.1\,\mathrm{ms}$) until it reaches some maximum spreading diameter ($t = 3.0\,\mathrm{ms}$), and then starts to recede ($t = 4.1\,\mathrm{ms}$) leading to a rebound ($t = 10.9\,\mathrm{ms}$). During the whole contact time the droplet does not wet the surface, but rather levitates on a thin vapor cushion caused by the film boiling phenomena. Due to the rebound, the time of contact between the drop and the surface is quite short compared to the contact time in other impact regimes. For this purpose the time for heat transfer is limited. This is important for cooling applications since the cooling effectiveness of impinging drops relies on the area of the spreading drop and the duration of contact.

In Fig. 5.30 the drop contact diameter in the film boiling regime is shown for various substrate temperatures onto aluminum substrates. Since the drop levitates on a very thin vapor layer, which is not visible in the observations due to resolving capacity, the contact diameter is defined according to section 4.1 (c.f. Fig. 4.3) from the observed images. Figure 5.30(a) shows drop impacts onto a smooth polished substrate ($R_{\mathrm{a}} \approx 0.05\,\mu\mathrm{m}$), while the experiments in Fig. 5.30(b) have been performed onto a rough sandblasted substrate ($R_{\mathrm{a}} \approx 2.5\,\mu\mathrm{m}$). It is obvious that there is almost no dependence on the initial

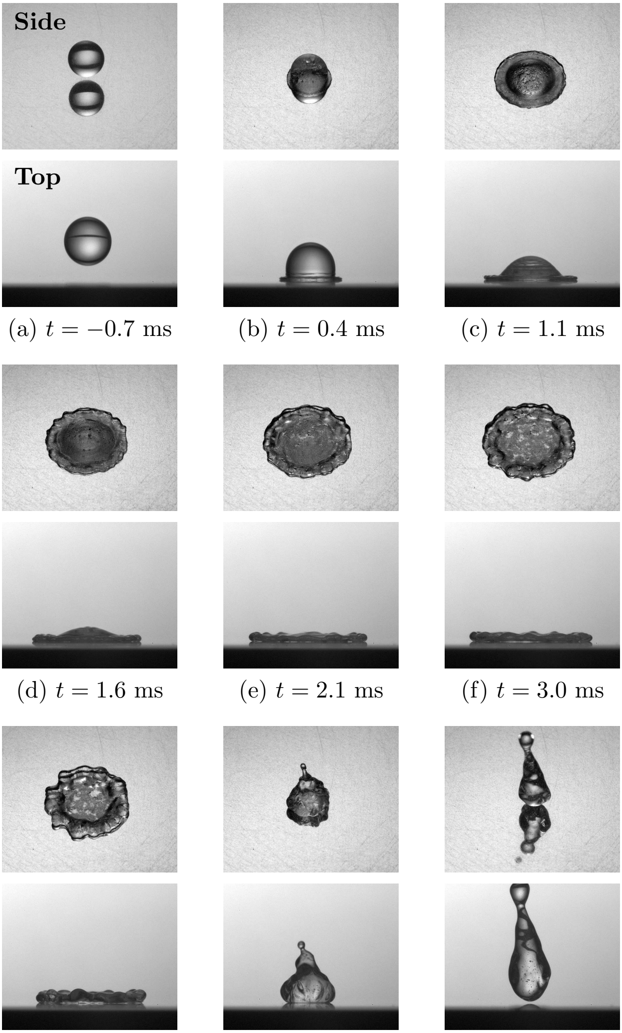

(a) $t = -0.7$ ms (b) $t = 0.4$ ms (c) $t = 1.1$ ms

(d) $t = 1.6$ ms (e) $t = 2.1$ ms (f) $t = 3.0$ ms

(g) $t = 4.1$ ms (h) $t = 7.1$ ms (i) $t = 10.9$ ms

Figure 5.29: Drop impact in the film boiling regime: detailed top- and side-view observation of the impinging drop. The impact parameters are $D_0 = 2.2\,\mathrm{mm}$, $U_0 = 2.4\,\mathrm{m/s}$, and $T_{\mathrm{w0}} = 330\,^\circ\mathrm{C}$. (Reprinted (adapted) from Breitenbach et al. (2017b). © 2017 Elsevier.)

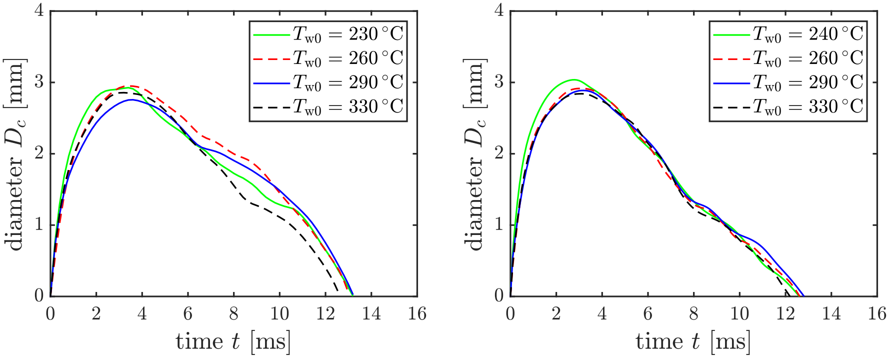

(a)

(b)

Figure 5.30: Drop contact diameter in the film boiling regime for various initial substrate temperatures: (a) smooth aluminum (mirror polished) and (b) rough aluminum (sandblasted). The impact velocities $U_0 = 0.4\,\mathrm{m/s}$ and the drop diameter $D_0 = 2.2\,\mathrm{mm}$ are almost constant for all shown cases.

substrate temperature and roughness on the contact diameter D_c or the final contact time t_c. Minor differences can be explained by small fluctuation of the initial drop diameter and impact velocity. This indicates that the influence of the substrate and the thin vapor layer on the hydrodynamics of the drop spreading is negligibly small. On one side the substrate conditions can influences the onset of film boiling, on the other side, once a vapor layer is fully developed, the drop impact dynamics are independent of the substrate.

By changing the impact velocity of the drop, spreading significantly changes, as seen in Fig. 5.31(a). While the contact time slightly decreases for higher impact velocities, the maximum diameter substantially increases. It can be explained by the rising kinetic energy of the impinging drop, since the kinetic energy is expended by deforming the drop (Chandra & Avedisian, 1991). This is not a novel but an very important finding since it enlarges the liquid/solid heat transfer area.

Several approaches for the maximum spreading diameter can be found in literature using an energy balance, which compares the initial kinetic and surface energy of the falling drop with the surface energy of the spreading lamella in addition with some energy loss (Tran et al., 2012; Chandra &

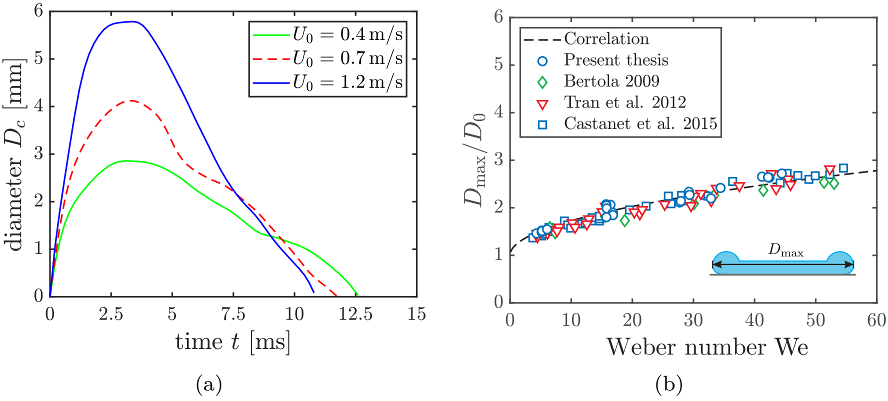

Figure 5.31: (a) Drop contact diameter in the film boiling regime for various impact velocities. The drop diameter $D_0 = 2.2\,\mathrm{mm}$ and substrate temperature $T_{\mathrm{w0}} = 330\,^{\circ}\mathrm{C}$ are almost constant for the various cases. (b) Maximum spreading diameter from the present thesis and existing literature data for various impact Weber number in comparison with the correlation (5.28).

Avedisian, 1991; Rein, 2002). Unfortunately, most of the estimations overestimate the value since the formulation of the energy loss during drop impact is not trivial. The energy loss is usually attributed to viscous dissipation, but Rein (2002) claims that there is also a major loss due to the transfer of kinetic energy to the vapor in the thin gap. Nonetheless, using the energy balance for the drop spreading needs to be critically reviewed since it does not tell something about the drop dynamics or underlying physics in general. However, as already mentioned above, the value of the maximum spreading diameter ratio for an impinging drop in the film boiling regime can be well estimated by using the correlation of Castanet et al. (2015) for low viscous fluids:

$$\frac{D_{\mathrm{max}}}{D_0} = 1 + 0.23\,\mathrm{We}^{0.5}. \tag{5.28}$$

In Fig. 5.31 the correlation is shown in combination with results from the present thesis (smooth and rough aluminum) and those from the literature (Bertola, 2009; Tran et al., 2012; Castanet et al., 2015). It is obvious, that

Eq. (5.28) fits very well for the various conditions. Once again, this result shows that the effect of the substrate is negligibly small, since the surface conditions greatly differ in the studies.

The following section is focused on the heat transfer in the film boiling regime. A predictive theoretical model for heat transfer during drop impact in the film boiling is introduced, which accounts for the main physical phenomena.

5.3.2 Evaluation of heat transfer during drop impact

Consider the impact of a single liquid drop onto a flat solid substrate in the developed film boiling regime. In this regime a vapor layer develops between the liquid and solid regions, as shown schematically in Fig. 5.32. Two thermal boundary layers accrue in the fluid and the solid material. The thermal boundary layers are denoted $\delta_l \sim \sqrt{\alpha_l t}$ for the liquid film and $\delta_\mathrm{w} \sim \sqrt{\alpha_\mathrm{w} t}$ for the wall region, using the thermal diffusivities of the liquid film α_l and the solid wall α_w. Typical values of the thermal diffusivity for metals are between 10^{-5} and $10^{-4}\,\mathrm{m^2/s}$. The thermal diffusivity for water is $10^{-7}\,\mathrm{m^2/s}$. The upper bound for the thermal boundary thickness in an aluminum substrate with the diffusivity $\alpha_\mathrm{w} = 10^{-4}\,\mathrm{m^2/s}$, at the typical time $t_i = D_0/U_0$, is $\delta_\mathrm{w} \sim 10^{-4}\,\mathrm{m}$ for a 1 mm drop impacting with a velocity $U_0 = 1\,\mathrm{m/s}$. In the liquid phase the thickness of the thermal boundary layer is smaller. Since both boundary layers are much smaller than the drop diameter, the heat transfer in the three different regions can be approximated by a one-dimensional model.

The contact temperature T_c at the solid-fluid interface $\vartheta = 0$ is unknown, while the temperature at the liquid interface can be approximated by the saturation temperature T_sat.

The thermal radiation of the wall will be neglected, because it is much smaller than the convective heat transfer (Rein, 2002). Therefore, the overall energy balance equation, which accounts for the energy of liquid vaporization, can be expressed as

$$\dot{q}_1 = \dot{q}_\mathrm{v} = \dot{q}_2 + \rho_l L \frac{\mathrm{d}h}{\mathrm{d}t}, \tag{5.29}$$

where $\mathrm{d}h/\mathrm{d}t$ is the change of vapor layer thickness, ρ_l and L are the density and the latent heat of evaporation of the liquid respectively.

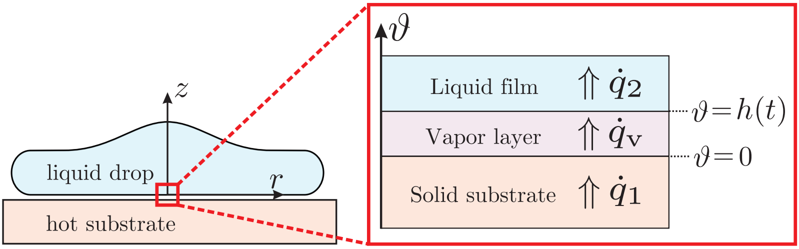

Figure 5.32: Sketch of the heat flow through the different regions: solid material, vapor layer, and liquid film. The solid/liquid interface is located at $\vartheta = 0$ and the liquid/liquid interface is located at $\vartheta = h$. (Reprinted (adapted) from Breitenbach et al. (2017b). © 2017 Elsevier.)

Instationary heat flow in the liquid film

Figure 5.33 shows a sketch of an axisymmetric spreading liquid film during the drop impact. To good approximation, the flow in the drop can be described as an inviscid flow. The expression for the velocity field $\boldsymbol{v}$ is well known from Yarin & Weiss (1995) and Roisman (2010):

$$v_r = \frac{r}{t}, \qquad v_z = -\frac{2z}{t}. \tag{5.30}$$

For constant thermodynamic properties, the energy balance equation in the spreading drop

$$\frac{\partial T_l}{\partial t} + \boldsymbol{v} \cdot \boldsymbol{\nabla} T_l - \alpha_l \boldsymbol{\nabla}^2 T_l = 0, \tag{5.31}$$

can be reduced with the help of Eq. (5.30) to the following expression

$$\frac{\partial T_l}{\partial t} - \frac{2z}{t}\frac{\partial T_l}{\partial z} = \alpha_l \frac{\partial^2 T_l}{\partial z^2}, \tag{5.32}$$

where $T_l(z,t)$ is the temperature distribution in the liquid film.

A self-similar solution of Eq. (5.32) is obtained by introduction of a similarity variable

$$\xi = \frac{z}{\sqrt{\alpha_l t}}, \tag{5.33}$$

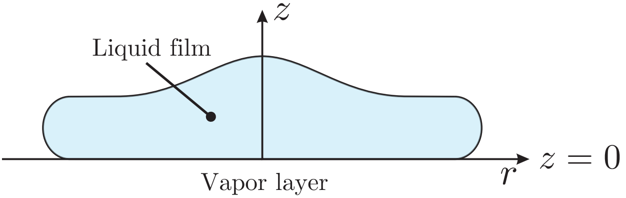

Figure 5.33: Sketch of an axisymmetric spreading film. (Reprinted from Breitenbach et al. (2017b). © 2017 Elsevier.)

which leads to an ordinary differential equation for the temperature field $T_l = T_l(\xi)$:

$$T_l'' + \frac{5}{2}\xi\, T_l' = 0, \tag{5.34}$$

which has to be solved subject to the initial and boundary conditions

$$T_l = T_{\text{sat}} \quad \text{at} \quad \xi = 0; \quad T_l \to T_{d0} \quad \text{at} \quad \xi \to \infty. \tag{5.35}$$

The similarity solution of Eqs. (5.34)-(5.35) is

$$T_l(z,t) = T_{\text{sat}} + (T_{d0} - T_{\text{sat}})\ \text{erf}\left(\frac{\sqrt{5}z}{2\sqrt{\alpha_l t}}\right), \tag{5.36}$$

and the corresponding heat flux at the liquid/liquid interface can be written in the form

$$\dot{q}_2(t) \equiv \lambda_l \frac{\partial T_l}{\partial z}\bigg|_{z=0} = \frac{\sqrt{5}e_l\,(T_{\text{sat}} - T_{d0})}{\sqrt{\pi}\sqrt{t}}, \tag{5.37}$$

where λ_l is the thermal conductivity and e_l is the thermal effusivity of the liquid film.

Instationary heat flow in the solid wall

The geometry and the definition of the coordinate system are shown schematically in Fig. 5.32. At $t = 0$ the vapor layer is in contact with a semi-infinite wall $\vartheta < 0$ at the initial surface temperature T_{w0}. The heat conduction equation in the wall

$$\frac{\partial T_{\text{w}}}{\partial t} - \alpha_{\text{w}} \frac{\partial^2 T_{\text{w}}}{\partial \vartheta^2} = 0, \tag{5.38}$$

has to be solved subject to the boundary conditions

$$T_\mathrm{w} = T_c \quad \text{at} \quad \vartheta = 0; \quad T_\mathrm{w} \to T_\mathrm{w0} \quad \text{at} \quad \vartheta \to -\infty, \tag{5.39}$$

where $T_\mathrm{w}(z,t)$ is the temperature in the wall region and the contact temperature T_c on the solid-fluid interface. The well-known similarity solution of Eqs. (5.38)-(5.39) is

$$T_\mathrm{w}(z,t) = T_c - (T_\mathrm{w0} - T_c) \,\mathrm{erf}\left(\frac{\vartheta}{2\sqrt{\alpha_\mathrm{w} t}}\right). \tag{5.40}$$

The heat flux density at the solid/vapor interface can be expressed as

$$\dot{q}_1(t) \equiv \lambda_\mathrm{w} \frac{\partial T_\mathrm{w}}{\partial \vartheta}\bigg|_{\vartheta=0} = \frac{e_\mathrm{w}\,(T_\mathrm{w0} - T_\mathrm{c})}{\sqrt{\pi}\sqrt{t}}, \tag{5.41}$$

where λ_w is the thermal conductivity and e_w is the thermal effusivity of the solid wall material.

The contact temperature T_c will be determined from the overall energy balance of the spreading drop, considered in the next section.

Dynamics of vapor creation

The dynamics of the vapor flow can be different for various stages of drop impact. We distinguish two main vapor growth regimes: heat transfer-controlled and inertial. In initial stage of drop spreading the pressure in the liquid is determined by the inertial in the liquid phase. The vapor growth in this stage is governed mainly by the heat transfer in the liquid and solid regions. This heat transfer-controlled growth is analogous to the growth of a bubble in a superheated liquid considered in Plesset & Zwick (1954); Scriven (1959) and Prosperetti & Plesset (1978), whose radius increases as square root of time. The thickness in the vapor layer near the rim is much smaller than that in the drop center (as shown schematically in Fig. 5.34), whereas the vapor velocity in this region, computed in Dawi et al. (2013), is relatively high. The pressure in the central vapor region is governed by the pressure loss in the this thin gap near the drop rim.

The pressure in the vapor layer is determined by the inertia in the impacting liquid drop. It is estimated in Roisman et al. (2009):

$$p \approx 1.7 \rho_l U_0^2 \exp[-3.1 t U_0 / D_0]. \tag{5.42}$$

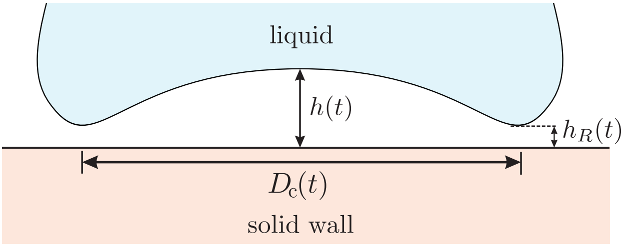

Figure 5.34: Sketch of the geometry of a vapor film. (Reprinted (adapted) from Breitenbach et al. (2017b). © 2017 Elsevier.)

This pressure is significant only during the initial phase of drop impact and deformation $t_i \sim D_0/U_0$. At larger times the pressure influence is minor and the internal stresses in the vapor layer become significant. These stresses govern the drop floating at large time after drop impact and eventual rebound. The inertial regime of vapor growth is analogous to the inertial bubble growth (Rayleigh, 1917). One of the asymptotes of the inertial vapor gap regime is the vapor flow under a static drop in the film boiling regime (Gottfried et al., 1966; Burton et al., 2012; Biance et al., 2003).

The heat transfer between the wall and the drop is inverse proportional to the vapor layer thickness. Therefore, the main part of the heat is transferred during the first stage of drop collision, when the gap thickness is smallest. In the following analysis only the heat transfer during the first heat transfer-controlled growth stage is considered.

The one-dimensional heat flux in the thin vapor layer can be roughly estimated as

$$\dot{q}_v(t) = \frac{\lambda_v}{h(t)} \left(T_c - T_{sat}\right), \tag{5.43}$$

determined by the thermal conductivity λ_v of the vapor, the vapor layer thickness $h(t)$, the saturation temperature T_{sat}, and the contact temperature T_c on the solid-liquid interface. With Eq. (5.29), Eq. (5.41) and Eq. (5.43) the contact temperature is obtained in the form

$$T_c = \frac{\sqrt{\pi}\lambda_v\sqrt{t}\,T_{sat} + e_w h(t)\,T_{w0}}{\sqrt{\pi}\lambda_v\sqrt{t} + e_w h(t)}, \tag{5.44}$$

as a function of time t and vapor layer thickness $h(t)$. Substituting expressions (5.44) and (5.43) into Eq. (5.29) yields an ordinary differential equation for the vapor layer thickness:

$$\frac{e_{\mathrm{w}}\lambda_{\mathrm{v}}\left(T_{\mathrm{w}0}-T_{\mathrm{sat}}\right)}{\sqrt{\pi}\lambda_{\mathrm{v}}\sqrt{t}+e_{\mathrm{w}}h(t)}-\frac{\sqrt{5}e_{l}\left(T_{\mathrm{sat}}-T_{d0}\right)}{\sqrt{\pi}\sqrt{t}}=\rho_{l}L\frac{dh}{dt}. \tag{5.45}$$

The solution of the ordinary differential equation (5.45) is obtained in the following form

$$h(t)=K\frac{e_{\mathrm{w}}\left(T_{\mathrm{w}0}-T_{\mathrm{sat}}\right)}{\rho_{l}L}\sqrt{t}, \tag{5.46}$$

where K is a dimensionless coefficient, determined as

$$K=\sqrt{(B-G)^{2}+\frac{4G}{\sqrt{\pi}}}-B-G, \tag{5.47}$$

where

$$G=\frac{\sqrt{\pi}\lambda_{\mathrm{v}}\rho_{l}L}{2\left(T_{\mathrm{w}0}-T_{\mathrm{sat}}\right)e_{\mathrm{w}}^{2}};\quad B=\frac{\sqrt{5}\left(T_{\mathrm{sat}}-T_{d0}\right)e_{l}}{\sqrt{\pi}\left(T_{\mathrm{w}0}-T_{\mathrm{sat}}\right)e_{\mathrm{w}}}. \tag{5.48}$$

Finally with the help of Eqs. (5.46)-(5.48), the contact temperature is explicitly expressed as

$$T_{\mathrm{c}}=\frac{2G\,T_{\mathrm{sat}}+K\,T_{\mathrm{w}0}}{2G+K}. \tag{5.49}$$

It is obvious from Eq. (5.49) that the contact temperature is not a function of the time and remains constant during drop impact as long as the boundary layer δ_{w} is much smaller than the solid substrate. The heat flux density of an impacting single droplet in the film boiling regime can be calculated using

$$\dot{q}_{1}(t)=\frac{2G\,e_{\mathrm{w}}\left(T_{\mathrm{w}0}-T_{\mathrm{sat}}\right)}{\sqrt{\pi}\left(K+2G\right)\sqrt{t}}. \tag{5.50}$$

Figure 5.35(a) and (b) shows the vapor layer thickness $h(t)$ and the transferred heat flux $\dot{q}_1(t)$ over time for various surface temperatures. The vapor layer thickness increase with the square root of time, while the heat flux decrease antiproportional. Both graphs were calculated with the properties

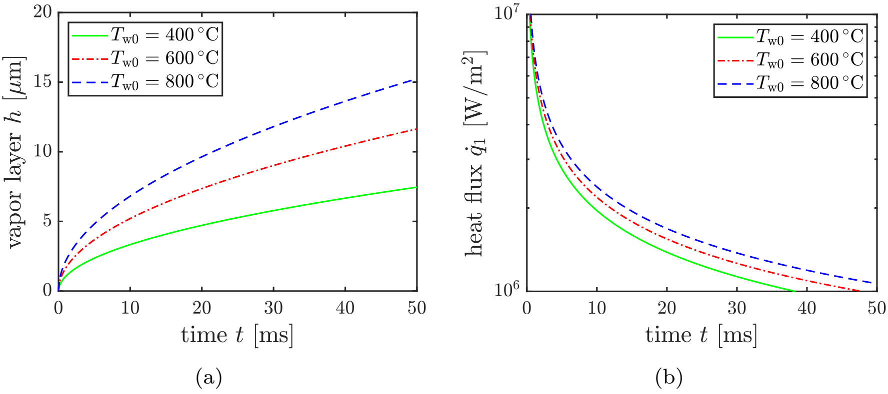

Figure 5.35: (a) Vapor layer thickness $h(t)$ and the (b) heat flux $\dot{q}_1(t)$ over time for various initial substrate temperatures T_{w0}. Both graphs were calculated with the properties of a water drop with $T_l = 25\,°C$ impacting onto a stainless steel surface. (Reprinted (adapted) from Breitenbach et al. (2017b). © 2017 Elsevier.)

of a water droplet impacting on a stainless steel surface. Furthermore, a comparison of the predicted model (5.46) for the vapor layer thickness with experimental data from Chaze (2017) is shown in Fig. 5.36. The experimental data have been obtained for impinging water drops onto a hot sapphire substrate at various impact Weber numbers. The agreement between the data and the model is rather good, although no adjustable constant is used in the model. Noteworthy is the fact, that the theoretical prediction (5.46) for the vapor layer thickness is not influence by the impact velocity of the drop, again in excellent agreement with the experimental results. Furthermore the estimated values are in the same order as experimental results performed by Tran et al. (2012).

The total heat removed by a single impacting drop during the initial time t_i can be therefore estimated using

$$Q_{\text{single}} \approx \int_0^{t_i} \pi \dot{q}_1(t) R_d(t)^2 \mathrm{d}t, \tag{5.51}$$

where $R(t)$ is the instantaneous drop spreading radius. The spreading radius during this initial stage of drop spreading, $R_d(t) \approx 1.4 D_0 \sqrt{t U_0 / D_0}$, has been measured in Rioboo et al. (2002) for a wide range of impact parameters.

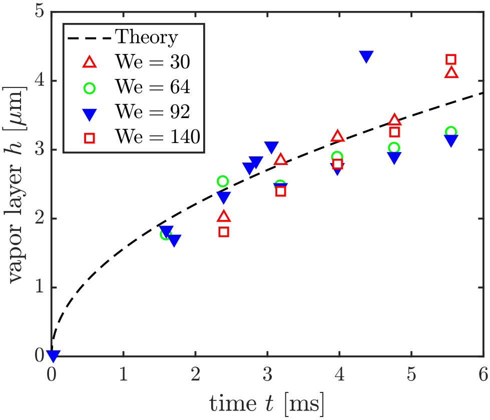

Figure 5.36: Vapor layer thickness $h(t)$ calculated with the theoretical predication (5.46) in comparison with experimental data obtained in Chaze (2017) for an impacting water drop onto a hot sapphire substrate at various impact Weber numbers. The drop diameter is constant for all cases.

By calculating the integral in Eq. (5.51) with the help of Eq. (5.50) leads to an estimation of the total heat removed by a single impacting drop in the film boiling regime:

$$Q_{\text{single}} = \frac{4.63 D_0^{5/2} G \, e_{\text{w}} \, (T_{\text{w0}} - T_{\text{sat}})}{U_0^{1/2} \, (K + 2G)}. \tag{5.52}$$

Noteworthy is the fact, that Eq. (5.52) captures the influence of drop size and drop impact velocity on the total heat removed from a single drop in the same order as correlations from Bolle & Moureau (1982) and Bernardin & Mudawar (1997).

6 Spray cooling in the film boiling regime

In the present chapter the study of the single drop impact is extended for spray cooling in the film boiling regime. The model for spray cooling is based on superposition of the single drop events and accounts for drop interactions. For a dense spray these drop interactions significantly influence the values of heat flux. Section 6.1 provides a theoretical analysis of drop interactions during spray impact. In section 6.2 an expression for the heat transfer coefficient is obtained for spray cooling, which accounts for the heat associated with single drop impact and for drop interactions on the substrate. Parts of the section have been published in Breitenbach et al. (2017b, 2018b).

6.1 Drop interaction analysis

A statistic of drop interactions is essential for the estimation of the effective wetted surface ratio η_{wet}, because it is a measure average heat flux during the spray impact. The main dimensionless parameter determining the level of drop interactions is the cumulative wetted area of the substrate by the spray. This parameter is determined as

$$\lambda_k = \dot{N} \int_0^{\infty} P_D \int_0^{t_c} \frac{\pi D_c(t)^2}{4} \mathrm{d}t \, \mathrm{d}D_0, \tag{6.1}$$

where P_D is the probability density function of the drop diameter in the polydisperse spray, $D_c(t)$ is the contact diameter of a spreading drop, t is the time after first impact for each drop, and $\dot{N}$ is the number flux density. A logarithmic scale of the number flux density $\dot{N}$ over the mass flux densities j_m is shown in Fig. 6.1 for various drop diameters D_0. It is obvious that the number of drops significantly increase for smaller diameters, as well for higher mass flux densities. For instance, already at a mass flux density of $j_m = 1\,\text{kg/m}^2\text{s}$ (for drop diameter $D_0 = 50\,\mu\text{m}$) the number flux density of the spray is in the order of 10^{12}, which means unimaginable billion drops per second and square meter.

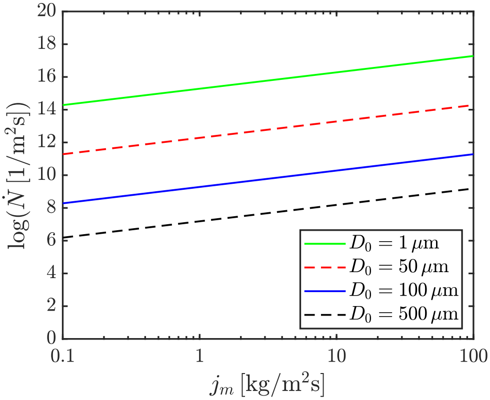

Figure 6.1: Logarithmic scale of the number flux density $\dot{N}$ over the mass flux densities j_m for various mean arithmetic diameters D_0 of the spray.

Expression (6.1) can be simplified by using the average value of drop diameter D_0 in the polydisperse spray and expressing the result in terms of the mass flux density

$$\lambda_k \approx \frac{3j_m}{2\rho_l D_0^3}\int_0^{t_c} D_c(t)^2 \mathrm{d}t. \tag{6.2}$$

Since the surface temperature is above Leidenfrost temperature, the contact time of the drop is finite; it is determined by the flow in the drop (c.f. Fig. 5.30). The evolution of the drop diameter can be roughly approximated by a parabola

$$D_c(t) = 4\,D_{\max}\left(\frac{t}{t_\mathrm{c}} - \frac{t^2}{t_\mathrm{c}^2}\right), \tag{6.3}$$

where $D_{\max}$ is the maximum spreading diameter of the drop during the impact. Figure 6.2 illustrates Eq. (6.3) with representative photographs of the impact process. The maximum spreading diameter of impacting drops in the film boiling regime has been measured in Tran et al. (2012) and Castanet et al. (2015) for various Weber numbers. A conservative correlation for the maximum diameter yields

$$D_{\max} = 0.81 D_0 (1 + 0.36\mathrm{We}^{0.48}). \tag{6.4}$$

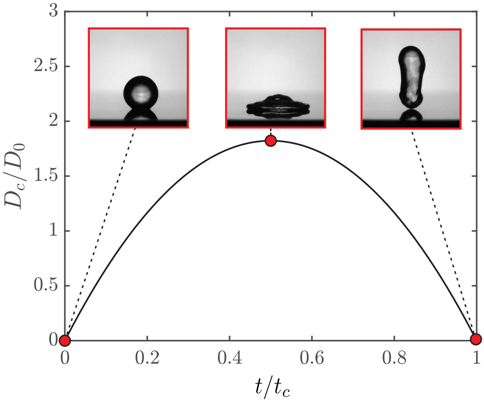

Figure 6.2: Equation (6.3) with representative photographs of the impact process of an water droplet. (Reprinted (adapted) from Breitenbach et al. (2017b). © 2017 Elsevier.)

The typical contact time in the film boiling regime is almost independent of the surface temperature and only influenced by the hydrodynamics of the drop impact. It can be roughly approximated from the obtained experimental data:

$$t_c \approx 4\frac{D_0}{U_0}. \tag{6.5}$$

The parameter λ_k can now be derived in the form

$$\lambda_k = \frac{2.1 j_m}{\rho_l U_0}(1 + 0.36\mathrm{We}^{0.48})^2. \tag{6.6}$$

Since the drop impacts are completely random in area and in time, the statistics of impacts follows the Poisson distribution (Feller, 1968). This means that the probability that a given point on the substrate belongs to exactly n spreading drops is

$$P(n; \lambda_k) = \frac{\lambda_k^n}{n!} e^{-\lambda_k}. \tag{6.7}$$

Correspondingly, the probability that a given point on the substrate is wetted finally leads to

$$P(n > 0; \lambda_k) = 1 - P(0; \lambda_k) \quad \Rightarrow \quad P_{\mathrm{wet}} = 1 - e^{-\lambda_k}. \tag{6.8}$$

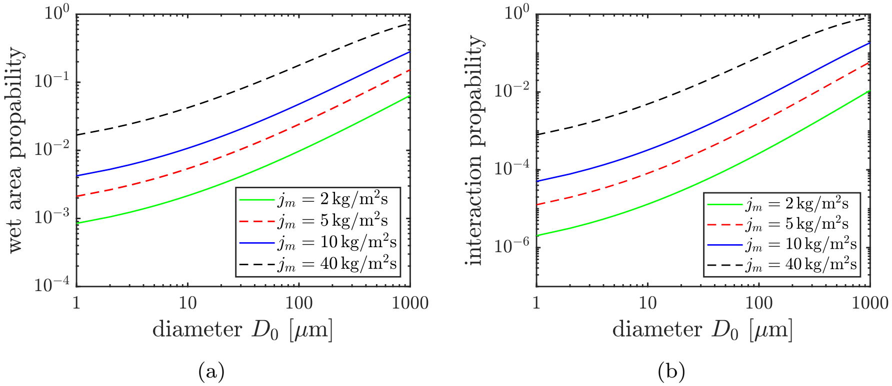

Figure 6.3: (a) Wet area probability P_{wet} and (b) drop interaction probability P_{int} as a function the mean diameter D_0 for different mass flux densities j_m of the spray. (Reprinted (adapted) from Breitenbach et al. (2017b). © 2017 Elsevier.)

The probability that an impinging drop on the substrate interacts with another drop can be calculated related to the analysis in Eq. (6.8). Using Poisson statistics the interaction probability of an impinging drop yields

$$P_{\mathrm{int}} = 1 - (1 + \lambda_{\mathrm{i}})\, e^{-\lambda_{\mathrm{i}}}, \tag{6.9}$$

with the parameter

$$\lambda_{\mathrm{i}} = \frac{5 j_m}{\rho_l U_0} (1 + 0.36 \mathrm{We}^{0.48})^2. \tag{6.10}$$

Figure 6.3(a) and (b) shows the wet area probability and drop interaction probability obtained in Eqs. (6.8)-(6.10) as a function of the diameter D_0 for various mass flux density j_m. Correspondingly, Fig. 6.4 and Fig. 6.5 illustrate a random drop distribution onto a well-defined area computed by Monte Carlo methods (based on the previous analysis) to graphically outline the drop interaction statistic during spray cooling. The computations are performed for various (a) mass flux densities j_m and (b) diameter D_0 of the spray. It is obvious that for higher mass flux densities the probability that a given point on the substrate is wetted, as well as the probability of drop interaction, significantly increases. This can be explained by the increasing

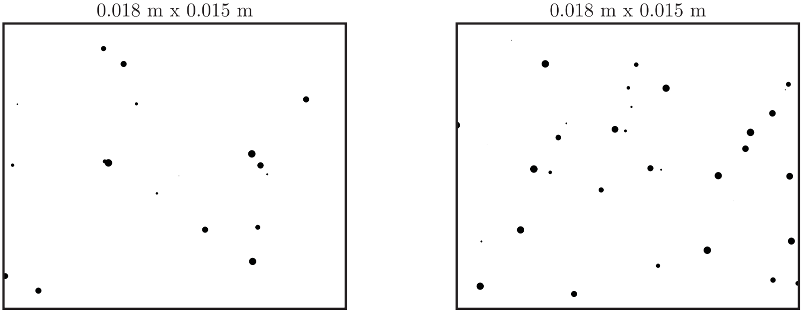

(a) $j_m = 1\,\mathrm{kg/m^2s}$ (b) $j_m = 2\,\mathrm{kg/m^2s}$

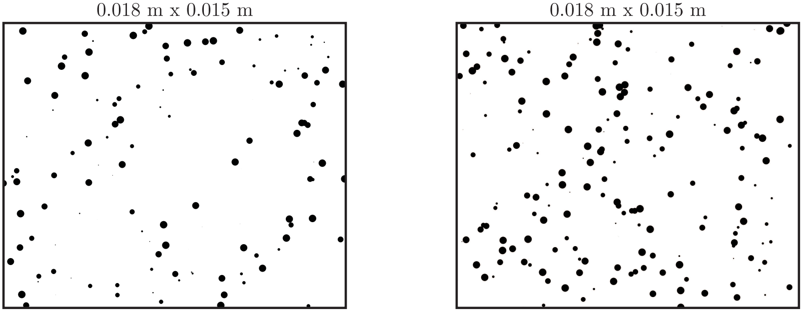

(c) $j_m = 5\,\mathrm{kg/m^2s}$ (d) $j_m = 10\,\mathrm{kg/m^2s}$

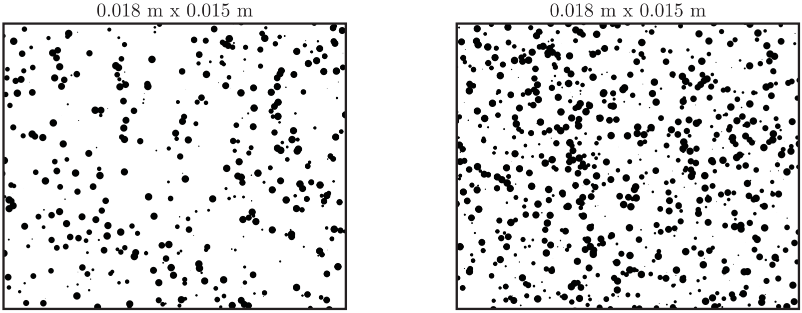

(e) $j_m = 20\,\mathrm{kg/m^2s}$ (f) $j_m = 40\,\mathrm{kg/m^2s}$

Figure 6.4: Random drop distribution onto the hot surface during spray cooling for various mass flux densities computed with Monte Carlo method. The constant diameter $D_0 = 100\,\mu\mathrm{m}$ and impact velocity $U_0 = 10\,\mathrm{m/s}$ of the spray are constant for all cases.

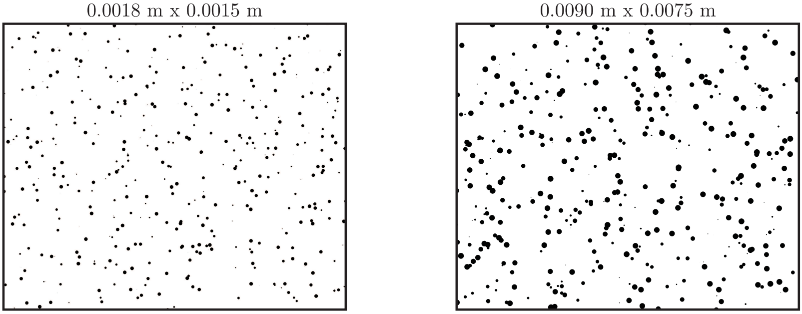

(a) $D_0 = 10\,\mu$m (b) $D_0 = 50\,\mu$m

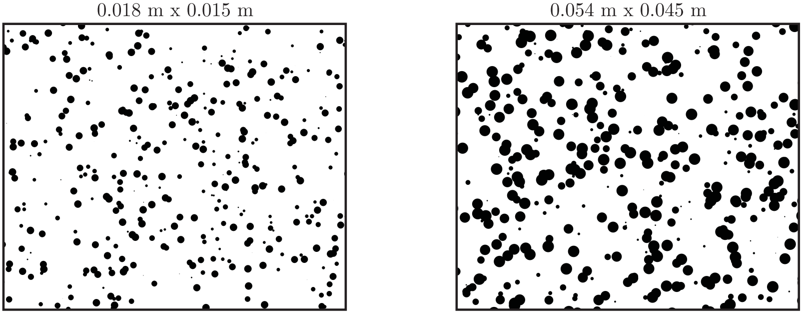

(c) $D_0 = 100\,\mu$m (d) $D_0 = 300\,\mu$m

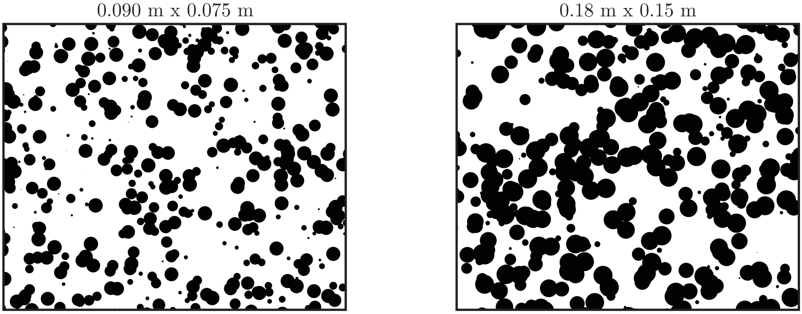

(e) $D_0 = 500\,\mu$m (f) $D_0 = 1000\,\mu$m

Figure 6.5: Random drop distribution onto the hot surface during spray cooling for various constant diameters computed with Monte Carlo method. The mass flux density $j_m = 20\,\mathrm{kg/m^2s}$ and mean impact velocity $U_0 = 10\,\mathrm{m/s}$ of the spray are constant for all cases.

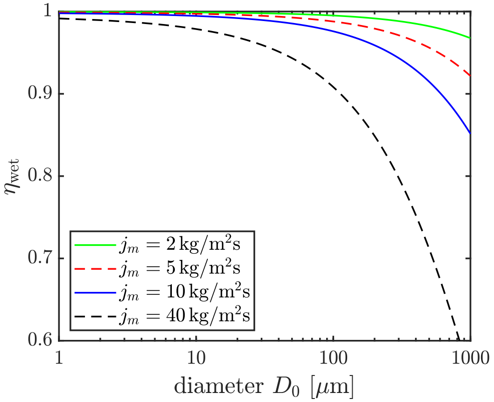

Figure 6.6: Effective wetted substrate ratio η_{wet} over the mean diameter D_0 for different mass flux densities j_m of the spray. (Reprinted (adapted) from Breitenbach et al. (2017b). © 2017 Elsevier.)

number flux density of drops impacting onto the surface (c.f. Fig. 6.1). In consequence, more and bigger drop clusters can be observed at higher mass flux densities. However, Fig. 6.3 and Fig. 6.5 prove that for an increasing diameter the probability of drop interaction increases as well, whereas the number flux density decreases (c.f. Fig. 6.1). For instance, with a constant drop diameter $D_0 = 1000\,\mu\text{m}$ the conditions are already close to percolation threshold (Yarin et al., 2017), although multiple dry spots are visible. This observation can be explained by an increasing spreading diameter and increasing contact time for larger droplets which results in a higher interaction probability.

Due to drop interactions, the actual wetted area of the substrate is smaller than the cumulative wetted area of all the impacting drops. An effective wetted substrate ratio is introduced as

$$\eta_{\text{wet}} = \frac{1 - e^{-\lambda_k}}{\lambda_k}, \tag{6.11}$$

which accounts for these interactions. Figure 6.6 illustrates the dependence of η_{wet} on drop diameter D_0 and the mass flux density j_m. As already indicated in the Monte Carlo simulations in Fig. 6.4 and Fig. 6.5, it is obvious that for larger drop diameters the effective wetted substrate ratio significantly decreases due to rising drop interactions. This analysis is important and can be used as a first estimation for an optimized spray solution, *i.e.*, which mass flux results in the lowest interaction probability and the highest heat flux.

6.2 Evaluation of heat transfer during spray cooling

Sparse spray impact

Considering a sparse spray, where the mass flux of the spray is small, drop interactions can be neglected. Therefore, the transferred heat from the hot substrate to the impinging spray can be calculated based on superposition of the transferred heat from the single drop event according to section 5.3. The heat transfer coefficient of a sparse spray for which the effect of drop interaction on the wall is negligibly small can be thus estimated as

$$\alpha_{\mathrm{ht}} \approx \frac{6\, j_m\, Q_{\mathrm{sd}}}{\pi D_0^3\, \rho_l\, \Delta T}, \quad \text{with} \quad \Delta T = T_{\mathrm{w}0} - T_{d0}. \tag{6.12}$$

where Q_{sd} is the heat removed by a single drop. With the help of Eq. (5.52) the heat transfer coefficient is expressed in the form

$$\alpha_{\mathrm{ht}} = 8.85\chi \frac{j_m G\, e_{\mathrm{w}}\, (T_{\mathrm{w}0} - T_{\mathrm{sat}})}{\rho_l \Delta T\, (K + 2G)\, D_0^{1/2} U_0^{1/2}}. \tag{6.13}$$

Here χ is an dimensionless constant. It accounts for the heat flux during the later stages of drop spreading, which is not considered in the present analysis. Since the heat flux density sharply reduces at large times, the value of χ has to be in order of unity. The coefficient χ will be estimated by fitting to the experimental data.

Expression (6.13) is valid only for sparse sprays for which the drop interactions at the substrate is rare and spray cooling can be thus described as a superposition of single drop impacts.

Dense spray impact

For a dense spray, however, drop interactions on the surface must be taken into account. This will decrease the total heat flux, since the effective wetted surface area decreases due to the drop interactions. The analysis has been

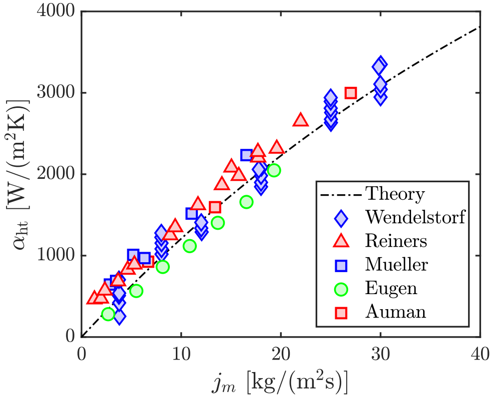

Figure 6.7: Heat transfer coefficient for water spray as a function of the mass flux densities of the spray j_m. Comparison of the theoretical predictions (6.14) with the existing experimental data for approximately the same operational conditions: $\Delta T \approx 700\,^\circ\mathrm{C}$, $D_0 \approx 350\,\mu\mathrm{m}$, $U_0 \approx 14\,\mathrm{m/s}$. The lines represent the theoretical predictions and the symbols present the corresponding experimental data from literature (Auman et al., 1967; Mizikar, 1970; Müller & Jeschar, 1983; Reiners, 1987; Wendelstorf et al., 2008a). (Reprinted (adapted) from Breitenbach et al. (2017b). © 2017 Elsevier.)

shown in section 6.1. The heat flux coefficient for dense spray can be obtained by modification of the expression (6.13)

$$\alpha_{\mathrm{ht}} = 8.85\chi \frac{j_m G\, e_{\mathrm{w}}\left(T_{\mathrm{w0}} - T_{\mathrm{sat}}\right)}{\rho_l \Delta T\left(K + 2G\right) D_0^{1/2} U_0^{1/2}} \eta_{\mathrm{wet}}, \tag{6.14}$$

where η_{wet} is determined using Eq. (6.6) and Eq. (6.11). The heat flux during spray cooling in the film boiling regime for a dense spray finally yields

$$\dot{q}_{\mathrm{spray}} = 8.85\chi \frac{j_m G\, e_{\mathrm{w}}\left(T_{\mathrm{w0}} - T_{\mathrm{sat}}\right)}{\rho_l\left(K + 2G\right) D_0^{1/2} U_0^{1/2}} \eta_{\mathrm{wet}}. \tag{6.15}$$

For polydisperse sprays the values of the mean arithmetic values for diameter D_0 and impact velocity U_0 are used in Eq. (6.13), Eq. (6.14) and Eq. 6.15, as claimed in the experiments used for estimation of the coefficient χ. In order to validate the model, in Fig. 6.7 the theoretical predictions are compared with existing experimental data for spray water cooling heat transfer.

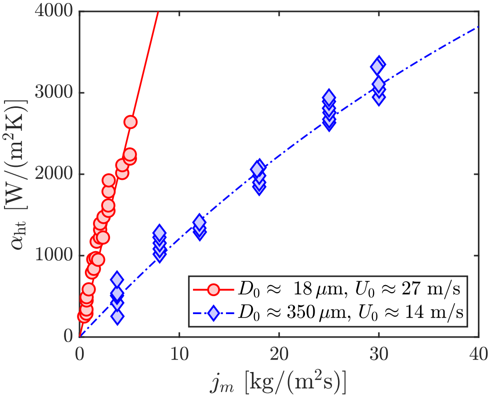

Figure 6.8: Heat transfer coefficient for water spray as a function of the mass flux densities of the spray j_m. Comparison of the theoretical predictions (6.14) with existing experimental data for different operational conditions. The lines represent the theoretical predictions and the symbols present the corresponding experimental data from literature (Wendelstorf et al., 2008a; Puschmann, 2003). (Reprinted (adapted) from Breitenbach et al. (2017b). © 2017 Elsevier.)

The comparison of the theoretical prediction (6.14) with various experimental data for the heat transfer coefficient α_{ht} (Auman et al., 1967; Mizikar, 1970; Müller & Jeschar, 1983; Reiners, 1987; Wendelstorf et al., 2008a) is performed for approximately the same operational conditions: $\Delta T \approx 700\,^\circ$C, $D_0 \approx 350\,\mu$m, $U_0 \approx 14$ m/s. The lines represent the theoretical predictions and the symbols present the corresponding experimental data from literature. The coefficient $\chi = 3.4$ is determined by fitting to the experimental data in Wendelstorf et al. (2008a). This parameter is the same for all the experiments used for the model evaluation. It is important that the value of χ is in order of unity, which indicates that the main physical mechanisms governing the heat transfer in the impacting drop are well described in the analysis.

In Fig. 6.8 the heat transfer coefficients are shown for different average spray impact parameters (Wendelstorf et al., 2008a; Puschmann, 2003), while Fig. 6.9 shows the heat transfer coefficient for various temperature difference $\Delta T = T_{\mathrm{w}0} - T_{d0}$ (Wendelstorf et al., 2008a).

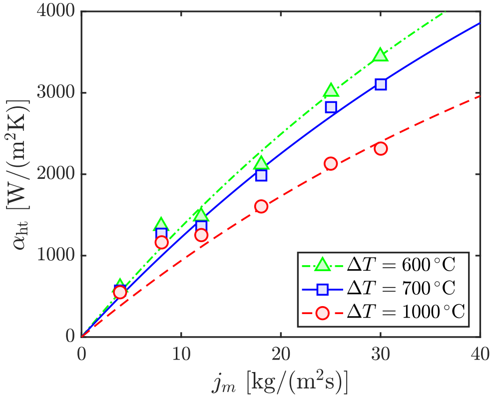

Figure 6.9: Heat transfer coefficient for water spray as a function of the mass flux densities of the spray j_m. Comparison of the theoretical predictions (6.14) with existing experimental data for various substrate temperatures. The lines represent the theoretical predictions and the symbols present the corresponding experimental data from literature (Wendelstorf et al., 2008a). (Reprinted (adapted) from Breitenbach et al. (2017b). © 2017 Elsevier.)

Noteworthy is the fact that Eq. (6.14) and Eq. (6.15) correctly capture the influence of drop size and drop velocity on the heat transfer coefficient, since the two experiments in Fig. 6.8 differed greatly in these parameters. Although χ was fitted to the Wendelstorf data in Wendelstorf et al. (2008a), the good agreement to the data obtained in Puschmann (2003) confirms the excellent predictive capability of Eq. (6.14) and Eq. (6.15). This influence of the drop size and impact velocity on the heat transfer coefficient is a novel finding in the modeling of spray cooling.

Furthermore, as the mass flux density j_m increases, the probability of drop interactions on the substrate increases (c.f. Fig. 6.3). This influence on the heat transfer coefficient, embodied in the factor η_{wet}, leads to a light flattening of the curves in Fig. 6.7, Fig. 6.8 and Fig. 6.9, again in excellent agreement with the experiments.

In order to summarize the influence of the mass flux density and the substrate temperature onto the heat flux, Fig. 6.10 shows a contour plot of the heat transfer coefficient as a function of the mass flux densities j_m and the temperature difference ΔT. This graph can be used for first estimations of

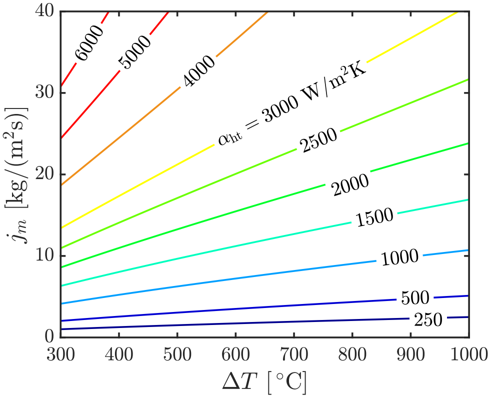

Figure 6.10: Contour plot of the theoretical prediction (6.14): heat transfer coefficient for water spray as a function of the mass flux densities of the spray j_m and the temperature difference ΔT. The spray impact conditions has been chosen: $D_0 = 350\,\mu\mathrm{m}$ and $U_0 = 14\,\mathrm{m/s}$.

the heat transfer coefficient in future spray cooling applications and therefore it can be used as new assessment tool (instead of the pure empirical correlation obtained in Wendelstorf et al. (2008a)).

7 Conclusions and outlook

In the present study the non-isothermal drop and spray impact have been investigated for various substrate and impact conditions. The research is motivated by a wide range of industrial spray applications, such as spray cooling or fuel injection in internal combustion engines. Even so, no universal model has been developed up to date to predict the heat transfer and cooling effectiveness during non-isothermal spray impact for a wide range of operating conditions. Hence, understanding single drop impact is an important and necessary preliminary step in the description and modeling of spray cooling, since it is a central element of the non-isothermal spray impact process. The present thesis has the objectives to enhance the long-term progress in utilizing knowledge about the heat transfer arising from single drop impacts onto hot surfaces to estimate the heat transfer involved in spray impact. The aim is to establish more universal physics-based correlations to describe quantities involved in the non-isothermal spray impact and cooling process.

The observed outcomes of single drop impact are classified for various impact conditions according to the heat transfer regimes: single phase cooling, nucleate boiling and thermal atomization, and film boiling. The present thesis underlines the observation that the hydrodynamic behavior of the drop impact can depend strongly on the respective regime. In general the Weber number is not adequate to capture or describe regime boundaries, since the Weber number does not involve any aspect of heat transfer.

To describe the quantities involved in the spray cooling process, different theoretical considerations for the various heat transfer regimes are obtained. For the single phase cooling regime a predictive model for the heat transfer during spreading and receding is developed, which is based on the similarity solution and also accounts for the heat convection within the fluid. It is shown that at high Prandtl number the heat transfer is mainly determined by the instantaneous wetted area as long as the effect of evaporation is minor. The model is extended to multiple drop impacts and predicts the decrease of heat flow due to interaction and coalescence of drops onto the hot substrate. In the nucleate boiling regime, characterized by an intensive heterogeneous nucleation and bubble generation which lead to contact line pinning, the heat transfer is analyzed theoretically. The analysis of the heat transferred from the substrate to the drop leads to the estimation of the typical time of drop evaporation. Both quantities are of paramount importance for spray cooling applications, since they can used to determine a first approach for an optimum spray. The analysis shows that, except for very sparse sprays, drop interaction and film accretion have to be taken into account for the nucleate boiling regime.

Observations from the present thesis allow to introduce the thermal atomization regime. The phenomenon is characterized by the dewetting of the substrate, caused not by rim dynamics but induced by thermal effects, and an intensive evaporation leading to a fine secondary spray. The characteristic velocity of the spray is scaled well with the theoretical vapor velocity. It is additionally shown that the Weber number, often used as a breakup threshold for splashing drops, is not a relevant parameter for the description of the thermal atomization threshold. For the film boiling regime a theoretical model for the heat transfer of an impinging single drop is developed, based on heat conduction in the solid wall, heat convection in the spreading drop and evaporation of the liquid phase, leading to the creation of a thin vapor layer. The thickness of the vapor layer increases with the square root of time and it is independent of the impact velocity. Consequently, the main part of the heat is transferred during the initial stages of drop impact where the vapor gap is at its thinnest, because it is inverse proportional to the vapor layer thickness. However, the total heat removed by one single drop is influenced by the impact velocity as well as the drop diameter since it influences the spreading dynamics. Furthermore, it can be concluded that the thermal effusivity of the solid substrate is one of the most important material properties to enhance heat transfer rates. Moreover, the same dependence can be equally seen for all the other boiling regimes.

The theoretical model for a single drop impact in the film boiling regime is applied to spray impact. An expression for the heat transfer coefficient is obtained, which predicts cooling even for a dense spray, since it accounts for drop interactions on the substrate surface. Due to drop interactions the wetted area of the substrate decrease, which leads to a decrease in heat

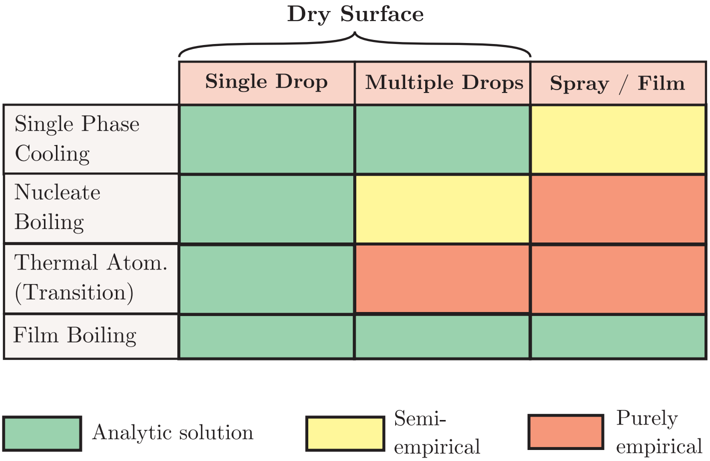

	Dry Surface		
	Single Drop	**Multiple Drops**	**Spray / Film**
Single Phase Cooling	🟩	🟩	🟨
Nucleate Boiling	🟩	🟨	🟥
Thermal Atom. (Transition)	🟩	🟥	🟥
Film Boiling	🟩	🟩	🟩

🟩 Analytic solution
🟨 Semi-empirical
🟥 Purely empirical

Figure 7.1: Summary: state of the art in terms of cooling regimes. (Reprinted (adapted) from Breitenbach et al. (2018b), with permission of Springer Nature. © 2018 Springer Nature.)

transfer. This interaction analysis is important to determine whether the spray is sparse or dense. It is shown that for higher mass flux densities and larger drop diameters the drop interaction probability significantly increases and drop interactions have to taken into account. Furthermore, it can be concluded that drop size and velocity of the spray have an significant influence onto the cooling efficiency of the spray. This drop size and velocity influence on the heat transfer is a novel finding in the modeling of spray cooling.

The extent to which data about single drop impacts can be used for spray impact depends primarily on the wetted surface area. For sprays in which the drop number density is low enough such that little drop interaction on the substrate arises, superposition of the single drop data can be used, incorporated into a statistical model for drop impact. This model is based on random spatial Poisson distribution of drops, but emphasizes the strong influence of both drop size and drop velocity on the overall heat transfer. Such an approach is shown to be successful for the single phase cooling (multiple drop impact) and the film boiling regimes (spray impact), whereas some further developments are still necessary for nucleate boiling.

Once the drop number density of the spray exceeds the limit at which a continuous film develops on the substrate, the situation becomes much more complicated. A review in the present literature indicates that under such conditions the hydrodynamics of drop impact onto a film are well described (Cossali et al., 1997; Weiss & Yarin, 1999; Yarin et al., 2017), but only rough estimates of the heat transfer can be made to date. For those conditions more work has to be done in future. On the other hand, for the film boiling regime a very promising model for heat transfer for sprays of high mass flux densities is introduced and verified in this thesis.

The results from the present thesis can be used for optimizing spray cooling efficiency. Figure 7.1 summarizes the current standing in terms of cooling regimes and whether single drops, multiple drop impacts or spray impact is examined. The state of the art is roughly given as the degree to which physics-based analytic models are now available.

One of the most challenging situations for which no adequate models are currently available is high mass flux sprays in the nucleate/transition boiling regime. For these conditions correlations are still highly empirical in nature.

Nomenclature

Small Greek Characters

α_{ht}	$\mathrm{W/m^2K}$	heat transfer coefficient
α_i	$\mathrm{m^2/s}$	thermal diffusivity of phase $i \in$ [v, w, l]
β	$\mathrm{m\sqrt{s}}$	thermodynamic factor
χ	$-$	adjustable coefficient
δt_{e}	s	exposure time
δx_{px}	m	spatial resolution
δ_i	m	thermal boundary layer in phase $i \in$ [w, l]
$\delta_{\nu l}$	m	viscous boundary layer in liquid
$\eta(t)$	$-$	area ratio factor
η_{wet}	$-$	effective wetted substrate ratio
γ_l	$\mathrm{S/m}$	electrical conductivity of liquid
λ_{i}	$-$	Poisson parameter for interaction probability
λ_i	$\mathrm{W/mK}$	thermal conductivity of phase $i \in$ [v, w, l]
λ_k	$-$	Poisson parameter for wetting probability
$\lambda_{1,2}$	m	wavelength of the light source 1, 2
ν	$\mathrm{m/s^2}$	kinematic viscosity of liquid
ν_0	$\mathrm{m/s^2}$	kinematic viscosity of liquid at room temperature
ϕ	rad	off-axis angle

π	–	Archimedes constant
ψ	rad	elevation angle
ρ_i	$^{\mathrm{kg}}/_{\mathrm{m}^3}$	density of phase $i \in$ [v, w, l]
σ	$^{\mathrm{N}}/_{\mathrm{m}}$	surface tension
τ	s	time delay / time constant
θ	rad	beam intersection angle
θ_c	deg	contact angle
ϑ	m	ϑ-coordinate
ξ	–	similarity variable
ζ	–	dimensionless coefficient

Capital Greek Characters

$\Delta\Phi_{12}$	deg	phase difference
ΔH_0	$^{\mathrm{J}}/_{\mathrm{kg}}$	enthalpy difference
Δl	m	distance between two points
ΔT	°C	temperature difference between substrate and fluid
ΔT_{w}	°C	superheated wall temperature
Δz	m	height above impact surface
Λ	–	dimensionless impact number
Θ	–	scaled wall temperature

Small Roman Characters

a_0	m	focal plane
a_f	m	far point
a_H	m	hyperfocal distance

a_n	m	near point
b	m	distance between two drops
c	m	circle of confusion
c_p	$^{\mathrm{J}}/_{\mathrm{kgK}}$	heat capacity
d	m	drop diameter (secondary spray)
d_{10}	m	mean diameter (secondary spray)
d_{32}	m	Sauter mean diameter (secondary spray)
d_L	m	diameter of the aperture
d_N	m	needle diameter
d_p	m	particle diameter
e	–	spacing parameter
e_i	$^{\mathrm{J}}/_{\mathrm{Km}^2\sqrt{\mathrm{s}}}$	thermal effusivity of phase $i \in$ [v, w, l]
f	m	focal length
f_D	$^{1}/_{\mathrm{s}}$	Doppler frequency
g	$^{\mathrm{m}}/_{\mathrm{s}^2}$	gravitational constant
$g(\xi)$	–	dimensionless function
$h(t)$	m	vapor layer thickness
h_{l0}	m	thickness of the evaporating layer
h_l	m	lamella thickness
$\bar{h}_l$	–	dimensionless lamella thickness
$\hat{h}_{\mathrm{film}}$	m	average film thickness
h_{res}	m	residual lamella thickness
j_m	$^{\mathrm{kg}}/_{\mathrm{m}^2\mathrm{s}}$	spray mass flux

k	$-$	f-number of the lens
k_d	$-$	adjustable coefficient
k_l	$-$	adjustable coefficient
k_w	$-$	adjustable coefficient
n	$-$	number of drops
n_r	$-$	relative refractive index
p	Pa	pressure
$\dot{q}$	W/m^2	heat flux
$\langle \dot{q} \rangle$	W/m^2	time averaged heat flux
$q_*^{''}$	$-$	dimensionless critical heat flux
r	m	r-coordinate
t	s	time
$\bar{t}$	$-$	dimensionless time
t_0	s	inception instant of the thermal boundary layer
t_c	s	contact time
$\bar{t}_c$	$-$	dimensionless contact time
t_i	s	initial time
t_max	s	time at maximum spreading
t_σ	s	typical time of capillary oscillations
t_w	s	bubble waiting time
u_d	m/s	drop velocity (secondary spray)
u_p	m/s	particle velocity
u_v	m/s	vapor velocity

$\boldsymbol{v}$	$\mathrm{m/s}$	film flow velocity vector
v_r	$\mathrm{m/s}$	film flow velocity in r-direction
v_z	$\mathrm{m/s}$	film flow velocity in z-direction
x	m	x-coordinate
y	m	y-coordinate
z	m	z-coordinate

Capital Roman Characters

A_c	m^2	contact area
A_d	m^2	cross-sectional drop area
A_e	m^2	cumulative wetted area
$\bar{A}(t)$	–	dimensionless function
B	–	dimensionless coefficient
Bo_m	–	modified boiling number
Ca	–	capillary number
D_0	m	initial drop diameter
D_{32}	m	Sauter mean diameter (impinging spray)
D_c	m	contact (spreading) diameter
D_max	m	maximum spreading diameter
$\overline{D}_\mathrm{max}$	–	spreading factor
DOF	m	depth of field
E^*	–	scaled heat
E_S	J	surface energy
G	–	dimensionless coefficient

$\mathscr{I}(\mathrm{Pr}_l)$	–	dimensionless function
Ja	–	Jakob number
K	–	K-number
K	–	dimensionless coefficient
L	J/kg	latent heat of evaporation
$\dot{N}$	1/m²s	number flux density
Nu	–	Nusselt number
Oh	–	Ohnesorge number
P	–	probability
P_D	–	probability density function
Pe	–	Peclet number
Pr_l	–	Prandtl number
$\dot{Q}$	W	heat flow
Q	J	heat
R	m	radius
$\bar{R}$	–	dimensionless radius
$\mathscr{R}$	–	dimensionless contact time
R_a	m	arithmetic average height
R_B	m	bubble radius
$R_d(t)$	m	drop spreading radius
Re	–	Reynolds number
R_max	m	maximum spreading radius
Rsm	m	root mean square roughness

Rpk	m	mean height of peaks
St	–	Stanton number
T_i	°C	temperature of phase $i \in$ [w, l, s]
T_c	°C	contact temperature
T_{dL}	°C	dynamic Leidenfrost temperature
T_{d0}	°C	initial drop temperature
T_{sat}	°C	saturation temperature
T_{sL}	°C	static Leidenfrost temperature
T_{w0}	°C	initial substrate temperature
$\mathscr{U}$	–	dimensionless heat flux
U_0	$^{\mathrm{m}}/_{\mathrm{s}}$	initial impact velocity
$U_{\max}$	$^{\mathrm{m}}/_{\mathrm{s}}$	maximum velocity
$\dot{V}''$	$^{\mathrm{m^3 s^{-1}}}/_{\mathrm{m^2}}$	local volumetric flux
W	$^{\mathrm{m}}/_{\mathrm{s}}$	momentum flux averaged velocity
We	–	Weber number

Shortcuts

atom	atomization
break	breakup
corona	corona splash threshold
crit	critical
DOF	depth of field
l	liquid fluid
prompt	prompt splash threshold

rec	receding
s	spray
sd	single drop
spr	spreading
v	vapor layer
w	solid substrate

Bibliography

Aamir, M., Qiang, L., Hong, W., Xun, Z., Wang, J., & Sajid, M. (2017). Transient heat transfer performance of stainless steel structured surfaces combined with air-water spray evaporative cooling at high temperature scenarios. *Appl. Thermal Eng.*, 115:418–434.

Abu-Zaid, M. (2004). An experimental study of the evaporation characteristics of emulsified liquid droplets. *Heat Mass Transf.*, 40(9):737–741.

Aktershev, S. P. & Ovchinnikov, V. V. (2011). Modeling of the vaporization front on a heater surface. *J. Eng. Thermophys.*, 20(1):77–88.

Albrecht, H.-E., Damaschke, N., Borys, M., & Tropea, C. (2013). *Laser Doppler and Phase Doppler Measurement Techniques*. Springer Science & Business Media.

Auman, P. M., Griffiths, D. K., & Hill, D. R. (1967). Hot strip mill runout table temperature control. *Iron Steel Eng.*, 9:174–179.

Bai, C. & Gosman, A. D. (1995). Development of methodology for spray impingement simulation. Technical Report 950283, SAE Technical Paper.

Bankoff, S. G. (1958). Entrapment of gas in the spreading of a liquid over a rough surface. *AIChE J.*, 4(1):24–26.

Bar-Cohen, A., Arik, M., & Ohadi, M. (2006). Direct liquid cooling of high flux micro and nano electronic components. *Proc. IEEE*, 94(8):1549–1570.

Batzdorf, S. (2016). *Heat transfer and evaporation during single drop impingement onto a superheated wall.* Phd thesis, Technische Universität Darmstadt, Darmstadt, Germany.

Batzdorf, S., Breitenbach, J., Schlawitschek, C., Roisman, I. V., Tropea, C., Stephan, P., & Gambaryan-Roisman, T. (2017). Heat transfer during simultaneous impact of two drops onto a hot solid substrate. *Int. J. Heat Mass Transf.*, 113:898–907.

Baumeister, K. & Simon, F. (1973). Leidenfrost temperature –its correlation for liquid metals, cryogens, hydrocarbons, and water. *J. Heat Transfer*, 95(2):166–173.

Berberović, E., Roisman, I. V., Jakirlić, S., & Tropea, C. (2011). Inertia dominated flow and heat transfer in liquid drop spreading on a hot substrate. *Int. J. Heat Fluid Flow*, 32(4):785–795.

Berenson, P. J. (1961). Film-boiling heat transfer from a horizontal surface. *J. Heat Transfer*, 83(3):351–356.

Bernardin, J. D. & Mudawar, I. (1997). Film boiling heat transfer of droplet streams and sprays. *Int. J. Heat Mass Transf.*, 40(11):2579 – 2593.

Bernardin, J. D. & Mudawar, I. (1999). The Leidenfrost point: experimental study and assessment of existing models. *ASME. J. Heat Transfer.*, 121(4):894–903.

Bernardin, J. D. & Mudawar, I. (2002). A cavity activation and bubble growth model of the Leidenfrost point. *ASME. J. Heat Transfer.*, 124(5):864–874.

Bernardin, J. D. & Mudawar, I. (2004). A Leidenfrost point model for impinging droplets and sprays. *J. Heat Transfer*, 126(2):272–278.

Bernardin, J. D., Stebbins, C. J., & Mudawar, I. (1996). Effects of surface roughness on water droplet impact history and heat transfer regimes. *Int. J. Heat Mass Transf.*, 40(1):73–88.

Bernardin, J. D., Stebbins, C. J., & Mudawar, I. (1997). Mapping of impact and heat transfer regimes of water drops impinging on a polished surface. *Int. J. Heat Mass Transf.*, 40(2):247–267.

Bertola, V. (2009). An experimental study of bouncing Leidenfrost drops: comparison between Newtonian and viscoelastic liquids. *Int. J. Heat Mass Transf.*, 52(7):1786–1793.

Bertola, V. (2015). An impact regime map for water drops impacting on heated surfaces. *Int. J. Heat Mass Transf.*, 85:430–437.

Bertola, V. & Sefiane, K. (2005). Controlling secondary atomization during drop impact on hot surfaces by polymer additives. *Physics of Fluids*, 17(10):108104.

Biance, A.-L., Chevy, F., Clanet, C., Lagubeau, G., & Quéré, D. (2006). On the elasticity of an inertial liquid shock. *J. Fluid Mech.*, 554:47–66.

Biance, A.-L., Clanet, C., & Quéré, D. (2003). Leidenfrost drops. *Phys. Fluids*, 15(6):1632–1637.

Bird, J. C., Tsai, S. S., & Stone, H. A. (2009). Inclined to splash: triggering and inhibiting a splash with tangential velocity. *New J. Phys.*, 11(6):063017.

Bolle, L. & Moureau, J. C. (1982). Spray cooling of hot surfaces. *Multiphase Sci. Technol.*, 1(1-4).

Breitenbach, J., Kissing, J., Roisman, I. V., & Tropea, C. (2018a). Characterization of secondary droplets during thermal atomization regime. *Exp. Therm Fluid Sci.*, 98:516 – 522.

Breitenbach, J., Roisman, I. V., & Tropea, C. (2017a). Drop collision with a hot, dry solid substrate: Heat transfer during nucleate boiling. *Phys. Rev. Fluids*, 2(7):074301.

Breitenbach, J., Roisman, I. V., & Tropea, C. (2017b). Heat transfer in the film boiling regime: Single drop impact and spray cooling. *Int. J. Heat Mass Transf.*, 110:34–42.

Breitenbach, J., Roisman, I. V., & Tropea, C. (2018b). From drop impact physics to spray cooling models: a critical review. *Exp. Fluids*, 59(3):55.

Brenn, G. (2017). *Heat and Mass Transfer*, pages 175–270. Springer Berlin Heidelberg, Berlin, Heidelberg.

Brutin, D., editor (2015). *Droplet wetting and evaporation: from pure to complex fluids.* Academic Press, London.

Buchmüller, I. (2014). *Influence of pressure on Leidenfrost effect*. PhD thesis, TU Darmstadt, Darmstadt.

Burton, J., Sharpe, A., van der Veen, R., Franco, A., & Nagel, S. (2012). Geometry of the vapor layer under a Leidenfrost drop. *Phys. Rev. Lett.*, 109(7):074301.

Butt, H.-J., Roisman, I. V., Brinkmann, M., Papadopoulos, P., Vollmer, D., & Semprebon, C. (2014). Characterization of super liquid-repellent surfaces. *Curr. Opin. Colloid. Interface Sci.*, 19(4):343–354.

Carey, V. P. (1992). *Liquid-Vapor Phase-Change Phenomena: An Introduction to the Thermophysics of Vaporization and Condensation Processes in Heat Transfer Equipment*. Series in Chemical and Mechanical Engineering. Taylor & Francis, Bristol.

Castanet, G., Caballina, O., & Lemoine, F. (2015). Drop spreading at the impact in the Leidenfrost boiling. *Phys. Fluids*, 27(6):063302.

Cazabat, A.-M. & Guena, G. (2010). Evaporation of macroscopic sessile droplets. *Soft Matter*, 6(12):2591–2612.

Celata, G. P., Cumo, M., Mariani, A., & Zummo, G. (2006). Visualization of the impact of water drops on a hot surface: effect of drop velocity and surface inclination. *Heat Mass Transf.*, 42(10):885–890.

Chandra, S. & Avedisian, C. T. (1991). On the collision of a droplet with a solid surface. *Proc. R. Soc. Lond. A Math. Phys. Sci.*, 432(1884):13–41.

Chaze, W. (2017). *Heat and mass transfert at the impact of a droplet in the film boiling regime: Application of optical diagnostics and modelling*. PhD thesis, Université de Lorraine.

Chaze, W., Castanet, G., Cabalina, O., Maillet, D., Pierson, J.-F., & Lemoine, F. (2017). Instantaneous heat transfers at the impact of a droplet onto a hot surfaces in the boiling regime. In *28th Conference ILASS-Europe 2017*, pages 282–289, Valencia, Spain. ILASS Europe.

Chen, L. (1977). Dynamic Spreading of Drops Impacting onto a Solid Surface. *Ind. Eng. Chem. Process Des. Dev.*, 16(2):192–197.

Chen, R.-H., Chow, L. C., & Navedo, J. E. (2002). Effects of spray characteristics on critical heat flux in subcooled water spray cooling. *Int. J. Heat Mass Transf.*, 45(19):4033 – 4043.

Chen, S.-J. & Tseng, A. A. (1992). Spray and jet cooling in steel rolling. *Int. J. Heat Mass Transf.*, 13(4):358–369.

Cheng, W.-L., Zhang, W.-W., Chen, H., & Hu, L. (2016). Spray cooling and flash evaporation cooling: the current development and application. *Renew. Sust. Energ. Rev.*, 55:614–628.

Cho, J. & Goodson, K. E. (2015). Thermal transport: cool electronics. *Nature Mater.*, 14:136–137.

Choi, K. & Yao, S. (1987). Mechanisms of film boiling heat transfer of normally impacting spray. *Int. J. Heat Mass Transf.*, 30(2):311 – 318.

Clanet, C., Béguin, C., Richard, D., & Quéré, D. (2004). Maximal deformation of an impacting drop. *J. Fluid Mech.*, 517:199.

Collings, E. W., Markworth, J. K., McCoy, J. K., & Saunders, J. H. (1990). Splat-quench solidification of freely falling liquid-metal drops by impact on a planar substrate. *J. Mater. Sci.*, 25:3677–3682.

Cossali, G. E., Coghe, A., & Marengo, M. (1997). The impact of a single drop on a wetted surface. *Exp. Fluids*, 22:463–472.

Cossali, G. E., Marengo, M., & Santini, M. (2005). Secondary atomisation produced by single drop vertical impacts onto heated surfaces. *Exp. Therm Fluid Sci.*, 29(8):937 – 946.

Cossali, G. E., Marengo, M., & Santini, M. (2008). Thermally induced secondary drop atomisation by single drop impact onto heated surfaces. *Int. J. Heat Fluid Flow*, 29(1):167–177.

Craig, V. S. J., Ninham, B. W., & Pashley, R. M. (1993). Effect of electrolytes on bubble coalescence. *Nature*, 364(6435):317–319.

Cui, Q., Chandra, S., & McCahan, S. (2003). The effect of dissolving salts in water sprays used for quenching a hot surface: Part 1 – Boiling of single droplets. *ASME. J. Heat Transfer.*, 125(2):326–332.

Datrice, N., Ramirez-San-Juan, J., Zhang, R., Meshkinpour, A., Aguilar, G., Nelson, J. S., & Kelly, K. M. (2006). Cutaneous effects of cryogen spray cooling on in vivo human skin. *Dermatol. Surg.*, 32(8):1007–1012.

Dawi, A. H., Herbert, S., Roisman, I. V., Gambaryan-Roisman, T., Stephan, P., & Tropea, C. (2013). Numerical Investigation of Drop Impact onto Hot Surfaces. In Gavaises, M., editor, *Proc. 25th European Conf. Liquid Atomization and Spray Systems*, Chania, Greece.

Deng, W. & Gomez, A. (2011). Electrospray cooling for microelectronics. *Int. J. Heat Mass Transf.*, 54(11):2270 – 2275.

DIN SPEC 91325 (2015). Characterization of sprays and spraying processes by measuring the size and velocity of non-transparent droplets.

Elston, L. J., Yerkes, K. L., Thomas, S. K., & McQuillen, J. (2009). Cooling performance of a 16-nozzle array in variable gravity. *J. Thermophys. Heat Transfer*, 23(3):571.

Erbil, H. Y. (2012). Evaporation of pure liquid sessile and spherical suspended drops: A review. *Adv. Colloid Interface Sci.*, 170(1-2):67–86.

Estes, K. A. & Mudawar, I. (1995). Correlation of Sauter mean diameter and critical heat flux for spray cooling of small surfaces. *Int. J. Heat Mass Transf.*, 38(16):2985–2996.

Fabbri, M., Jiang, S., & Dhir, V. K. (2005). A comparative study of cooling of high power density electronics using sprays and microjets. *J. Heat Transfer*, 127(1):38–48.

Faghri, A. & Zhang, Y. (2006). *Transport phenomena in multiphase systems.* Academic Press.

Favaro, P. & Soatto, S. (2007). *3–D Shape Estimation and Image Restoration: Exploiting Defocus and Motion Blur.* Springer-Verlag, London.

Feller, W. (1968). *An Introduction to Probability Theory and its Applications*, volume I. John Wiley & Sons., New York, 3rd edition.

FMP Technology GmbH (2014). Broschüre Tropfengenerator. Brochure.

Ford, R. & Furmidge, C. (1967). Impact and spreading of spray drops on foliar surfaces. *Soc Chem Ind Monogr*, 25:417–32.

Forster, H. K. & Zuber, N. (1954). Growth of a vapor bubble in a superheated liquid. *J. Appl. Phys.*, 25(4):474–478.

Forster, H. K. & Zuber, N. (1955). Dynamics of vapor bubbles and boiling heat transfer. *AIChE J.*, 1(4):531–535.

Fukai, J., Shiiba, Y., Yamamoto, T., Miyatake, O., Poulikakos, D., Megaridis, C. M., & Zhao, Z. (1995). Wetting effects on the spreading of a liquid droplet colliding with a flat surface: Experiment and modeling. *Phys. Fluids*, 7:236–247.

Ghodbane, M. & Holman, J. (1991). Experimental study of spray cooling with Freon-113. *Int. J. Heat Mass Transf.*, 34(4):1163 – 1174.

Gottfried, B., Lee, C., & Bell, K. (1966). The Leidenfrost phenomenon: film boiling of liquid droplets on a flat plate. *Int. J. Heat Mass Transf.*, 9(11):1167–1188.

Gottfried, B. S. & Bell, K. J. (1966). Film Boiling of Spheroidal Droplets. Leidenfrost Phenomenon. *Industrial & Engineering Chemistry Fundamentals*, 5(4):561–568.

Griffith, P. (1958). Bubble growth rates in boiling. *J. Heat Transfer*, 80:721–726.

Gross, K. A. & Berndt, C. C. (1998). Thermal processing of hydroxyapatite for coating production. *J. Biomed. Mater. Res.*, 39(4):580–587.

Hall, D. D. & Mudawar, I. (1995). Experimental and numerical study of quenching complex-shaped metallic alloys with multiple, overlapping sprays. *Int. J. Heat Mass Transf.*, 38(7):1201–1216.

Hammad, J., Mitsutake, Y., & Monde, M. (2004). Movement of maximum heat flux and wetting front during quenching of hot cylindrical block. *Int. J. Therm. Sci.*, 43(8):743–752.

Hecht, E. (1998). *Optics*. Addison-Wesley World Student Series. Addison-Wesley.

Herbert, S., Fischer, S., Gambaryan-Roisman, T., & Stephan, P. (2013). Local heat transfer and phase change phenomena during single drop impingement on a hot surface. *Int. J. Heat Mass Transf.*, 61:605–614.

Holman, J. & Kendall, C. (1993). Extended studies of spray cooling with Freon-113. *Int. J. Heat Mass Transf.*, 36(8):2239 – 2241.

Hsieh, S.-S., Fan, T.-C., & Tsai, H.-H. (2004). Spray cooling characteristics of water and R-134a. Part I: nucleate boiling. *Int. J. Heat Mass Transf.*, 47(26):5703–5712.

Hsieh, S.-S., Hsu, Y.-F., & Wang, M.-L. (2014). A microspray-based cooling system for high powered LEDs. *Energy Convers. Manage.*, 78:338 – 346.

Huddle, J. J., Chow, L. C., Lei, S., Marcos, A., Rini, D., Lindauer, S., Bass, M., & Delfyett, P. (2000). Thermal management of diode laser arrays. In *Semiconductor Thermal Measurement and Management Symposium, 2000. Sixteenth Annual IEEE*, pages 154–160. IEEE.

IEC 60584-1 (2013). Thermocouples - Part 1: EMF specifications and tolerances.

Inada, S. & Yang, W.-J. (1994). Film boiling heat transfer for saturated drops impinging on a heating surface. *Int. J. Heat Mass Transf.*, 37(16):2588 – 2591.

Ing, P., Sperry, C., Philstrom, R., Claybaker, P., Webster, J., & Cree, R. (1993). SS-1 supercomputer cooling system. In *Proceedings of IEEE 43rd Electronic Components and Technology Conference (ECTC '93)*, pages 218–237.

Itaru, M. & Kunihide, M. (1978). Heat transfer characteristics of evaporation of a liquid droplet on heated surfaces. *Int. J. Heat Mass Transf.*, 21(5):605–613.

Josserand, C. & Thoroddsen, S. T. (2016). Drop Impact on a Solid Surface. *Annu. Rev. Fluid Mech.*, 48(1):365–391.

Kandlikar, S. G. & Steinke, M. E. (2002). Contact angles and interface behavior during rapid evaporation of liquid on a heated surface. *Int. J. Heat Mass Transf.*, 45(18):3771 – 3780.

Karl, A., Anders, K., Rieber, M., & Frohn, A. (1996). Deformation of liquid droplets during collisions with hot walls: experimental and numerical results. *Part. Part. Syst. Charact.*, 13(3):186–191.

Karwa, N., Gambaryan-Roisman, T., Stephan, P., & Tropea, C. (2011). Experimental investigation of circular free-surface jet impingement quenching: transient hydrodynamics and heat transfer. *Exp. Therm. Fluid Sci.*, 35(7):1435–1443.

Karwa, N., Kale, S. R., & Subbarao, P. (2007). Experimental study of non-boiling heat transfer from a horizontal surface by water sprays. *Exp. Therm Fluid Sci.*, 32(2):571 – 579.

Kato, M., Abe, Y., Mori, Y. H., & Nagashima, A. (1995). Spray cooling characteristics under reduced gravity. *J. Thermophys. Heat Transfer*, 9(2):378–380.

Keitel, G. & Onken, U. (1982). Inhibition of bubble coalescence by solutes in air/water dispersions. *Chem. Eng. Sci.*, 37(11):1635 – 1638.

Kelly, K. M., Nelson, J. S., Lask, G. P., Geronemus, R. G., & Bernstein, L. J. (1999). Cryogen spray cooling in combination with nonablative laser treatment of facial rhytides. *Arch. Dermatol.*, 135(6):691–694.

Khavari, M., Sun, C., Lohse, D., & Tran, T. (2015). Fingering patterns during droplet impact on heated surfaces. *Soft matter*, 11(17):3298–3303.

Kim, J. (2007). Spray cooling heat transfer: the state of the art. *Int. J. Heat Fluid Flow*, 28(4):753–767.

Kissing, J. (2017). *Experimental study of the main parameters of secondary droplets produced by the non-isothermal drop impact phenomena.* Master thesis, Technische Universität Darmstadt.

Klinzing, W. P., Rozzi, J. C., & Mudawar, I. (1992). Film and transition boiling correlations for quenching of hot surfaces with water sprays. *J. Heat. Treat.*, 9(2):91–103.

Kunkelmann, C., Ibrahem, K., Schweizer, N., Herbert, S., Stephan, P., & Gambaryan-Roisman, T. (2012). The effect of three-phase contact line speed on local evaporative heat transfer: Experimental and numerical investigations. *Int. J. Heat Mass Transf.*, 55(7):1896–1904.

Kyriopoulos, O. N. (2010). *Gravity effect on liquid film hydrodynamics and spray cooling*. Ph.d. thesis, Technische Universität Darmstadt, Darmstadt, Germany.

Labergue, A., Gradeck, M., & Lemoine, F. (2015). Comparative study of the cooling of a hot temperature surface using sprays and liquid jets. *Int. J. Heat Mass Transf.*, 81(Supplement C):889 – 900.

Lagubeau, G., Fontelos, M. A., Josserand, C., Maurel, A., Pagneux, V., & Petitjeans, P. (2012). Spreading dynamics of drop impacts. *J. Fluid Mech.*, 713:50–60.

Landau, L. D. & Levich, B. G. (1988). Dragging of a liquid by a moving plate. *Acta Physicochim. U.R.S.S.*, 17:42–54.

Lefebvre, A. H. & McDonell, V. G. (2017). *Atomization and Sprays, Second Edition*. CRC Press, Boca Raton.

Leidenfrost, J. G. (1966). On the fixation of water in diverse fire. *Int. J. Heat Mass Transf.*, 9(11):1153–1166.

Lembach, A. N., Tan, H.-B., Roisman, I. V., Gambaryan-Roisman, T., Zhang, Y., Tropea, C., & Yarin, A. L. (2010). Drop impact, spreading, splashing, and penetration into electrospun nanofiber mats. *Langmuir*, 26(12):9516–9523.

Lewis, W. K. (1922). The evaporation of a liquid into a gas. *Trans. ASME.*, 44:325–340.

Liang, G. & Mudawar, I. (2017a). Review of drop impact on heated walls. *Int. J. Heat Mass Transf.*, 106:103–126.

Liang, G. & Mudawar, I. (2017b). Review of spray cooling – Part 1: Single-phase and nucleate boiling regimes, and critical heat flux. *Int. J. Heat Mass Transf.*, 115(Part A):1174 – 1205.

Liang, G. & Mudawar, I. (2017c). Review of spray cooling – Part 2: High temperature boiling regimes and quenching applications. *Int. J. Heat Mass Transf.*, 115(Part A):1206 – 1222.

Liang, G., Shen, S., Guo, Y., & Zhang, J. (2016). Boiling from liquid drops impact on a heated wall. *Int. J. Heat Mass Transf.*, 100:48 – 57.

Lin, L. & Ponnappan, R. (2003). Heat transfer characteristics of spray cooling in a closed loop. *Int. J. Heat Mass Transf.*, 46(20):3737–3746.

Lopes, M. C., Bonaccurso, E., Gambaryan-Roisman, T., & Stephan, P. (2013). Influence of the substrate thermal properties on sessile droplet evaporation: Effect of transient heat transport. *Colloids and Surfaces A: Physicochem. Eng. Aspects*, 432:64–70.

Lv, C., Hao, P., Zhang, X., & He, F. (2016). Drop impact upon superhydrophobic surfaces with regular and hierarchical roughness. *Appl. Phys. Lett.*, 108(14):141602.

Marengo, M., Antonini, C., Roisman, I. V., & Tropea, C. (2011). Drop collisions with simple and complex surfaces. *Curr. Opin. Colloid Interface Sci.*, 16(4):292–302.

Marmanis, H. & Thoroddsen, S. T. (1996). Scaling of the fingering pattern of an impacting drop. *Phys. Fluids*, 8(6):1344–1346.

Marrucci, G. (1969). A theory of coalescence. *Chem. Eng. Sci.*, 24(6):975 – 985.

Maxwell, J. C. (1877). Diffusion. In *Encyclopedia Britannica*, volume 2, page 82. Reprinted in *The Scientific Papers of James Clerk Maxwell*, edited by W. D. Niven. Cambridge University Press, Cambridge, 1890, p. 625.

McGinnis, F. & Holman, J. (1969). Individual droplet heat-transfer rates for splattering on hot surfaces. *Int. J. Heat Mass Transf.*, 12(1):95 – 108.

Mehdi-Nejad, V., Mostaghimi, J., & Chandra, S. (2003). Air bubble entrapment under an impacting droplet. *Phys. Fluids*, 15(1):173–183.

Michalak, T. E., Yerkes, K. L., Thomas, S. K., & McQuillen, J. B. (2010). Acceleration Effects on the Cooling Performance of a Partially Confined FC-72 Spray. *J. Thermophys. Heat Transfer*, 24(3):463–479.

Mikic, B. B. & Rohsenow, W. M. (1969). Bubble growth rates in non-uniform temperature field. *Prog. Heat Mass Transf.*, 2:283–292.

Mizikar, E. A. (1970). Spray-cooling investigation for continuous casting of billets and blooms. *Iron Steel Eng*, 47(6):53–60.

Moita, A. S. & Moreira, A. L. (2012). Scaling the effects of surface topography in the secondary atomization resulting from droplet/wall interactions. *Exp. Fluids*, 52(3):679–695.

Moita, A. S. & Moreira, A. L. N. (2009). Development of empirical correlations to predict the secondary droplet size of impacting droplets onto heated surfaces. *Exp. Fluids*, 47(4):755.

Moreira, A., Moita, A., & Panao, M. (2010). Advances and challenges in explaining fuel spray impingement: How much of single droplet impact research is useful? *Prog. Energy Combust. Sci.*, 36(5):554–580.

Moreira, A. L. N., Moita, A. S., Cossali, E., Marengo, M., & Santini, M. (2007). Secondary atomization of water and isooctane drops impinging on tilted heated surfaces. *Exp. Fluids*, 43(2-3):297–313.

Mudawar, I. & Deiters, T. A. (1994). A universal approach to predicting temperature response of metallic parts to spray quenching. *Int. J. Heat Mass Transf.*, 37(3):347–362.

Mudawar, I. & Valentine, W. S. (1989). Determination of the local quench curve for spray-cooled metallic surfaces. *J. Heat. Treat.*, 7(2):107–121.

Müller, H. R. & Jeschar, R. (1983). *Wärmeübergang bei der Spritzwasserkühlung von Nichteisenmetallen.* VDI-Verlag.

Myers, G. E. (1987). *Analytical methods in conduction heat transfer.* Genium Publishing Corporation, Schenectady.

Naber, J. D. & Reitz, R. D. (1988). Modeling engine spray/wall impingement. Technical Report 880107, SAE Technical Paper.

Nakoryakov, V. E., Misyura, S. Y., & Elistratov, S. L. (2012). The behavior of water droplets on the heated surface. *Int. J. Heat Mass Transf.*, 55(23):6609 – 6617.

Nayak, S. K., Mishra, P. C., & Parashar, S. K. S. (2016). Influence of spray characteristics on heat flux in dual phase spray impingement cooling of hot surface. *AEJ*, 55(3):1995 – 2004.

Nelson, J. S., Milner, T. E., Anvari, B., Tanenbaum, B. S., Kimel, S., Svaasand, L. O., & Jacques, S. L. (1995). Dynamic epidermal cooling during pulsed laser treatment of port-wine stain: A new methodology with preliminary clinical evaluation. *Arch. Dermatol.*, 131(6):695–700.

Nishio, S. & Kim, Y.-C. (1998). Heat transfer of dilute spray impinging on hot surface (simple model focusing on rebound motion and sensible heat of droplets). *Int. J. Heat Mass Transf.*, 41(24):4113 – 4119.

Ohtake, H. & Koizumi, Y. (2004). Study on propagative collapse of a vapor film in film boiling (mechanism of vapor-film collapse at wall temperature above the thermodynamic limit of liquid superheat). *Int. J. Heat Mass Transf.*, 47(8):1965–1977.

Oliphant, K., Webb, B., & McQuay, M. (1998). An experimental comparison of liquid jet array and spray impingement cooling in the non-boiling regime. *Exp. Therm Fluid Sci.*, 18(1):1 – 10.

Opfer, L. (2014). *Controlling Liquid Atomization using Dilute Emulsions: Mitigation of Pesticide Spray Drift*. PhD thesis, Technische Universität Darmstadt, Darmstadt, Germany.

Opfer, L., Roisman, I. V., Venzmer, J., Klostermann, M., & Tropea, C. (2014). Droplet-air collision dynamics: Evolution of the film thickness. *Phys. Rev. E*, 89:013023.

Otsu, N. (1979). A Threshold Selection Method from Gray-Level Histograms. *IEEE Transactions on Systems, Man, and Cybernetics*, 9(1):62–66.

Pais, M. R., Chow, L. C., & Mahefkey, E. T. (1992). Surface roughness and its effects on the heat transfer mechanism in spray cooling. *J. Heat Transfer*, 114(1):211–219.

Palacios, J., Hernández, J., Gómez, P., Zanzi, C., & López, J. (2013). Experimental study of splashing patterns and the splashing/deposition threshold in drop impacts onto dry smooth solid surfaces. *Exp. Therm. Fluid. Sci.*, 44:571–582.

Pan, K.-L., Tseng, K.-C., & Wang, C.-H. (2010). Breakup of a droplet at high velocity impacting a solid surface. *Exp. Fluids*, 48(1):143–156.

Pasandideh-Fard, M., Qiao, Y. M., Chandra, S., & Mostaghimi, J. (1996). Capillary effects during droplet impact on a solid surface. *Phys. Fluids*, 8:650–659.

Pedrotti, F., Pedrotti, L., Bausch, W., & Schmidt, H. (2007). *Optik für Ingenieure: Grundlagen.* Springer Berlin Heidelberg.

Piggott, B. D. G., White, E. P., & Duffey, R. B. (1976). Wetting delay due to film and transition boiling on hot surfaces. *Nucl. Eng. Des.*, 36(2):169–181.

Plesset, M. & Zwick, S. A. (1954). The growth of vapor bubbles in superheated liquids. *J.Appl. Phys.*, 25(4):493–500.

Prosperetti, A. & Plesset, M. S. (1978). Vapour-bubble growth in a superheated liquid. *J. Fluid Mech.*, 85(02):349–368.

Puschmann, F. (2003). *Experimentelle Untersuchung der Spraykühlung zur Qualitätsverbesserung durch definierte Einstellung des Wärmeübergangs.* PhD thesis, Otto-von-Guericke-Universität Magdeburg, Universitätsbibliothek.

Quéré, D. (2013). Leidenfrost Dynamics. *Annu. Rev. Fluid Mech.*, 45:197–215.

Rayleigh, L. (1917). On the pressure developed in a liquid during the collapse of a spherical cavity. *Phil. Mag.*, 34(200):94–98.

Rein, M. (2002). *Drop-surface interactions*, volume 456. Springer.

Reiners, U. (1987). *Wärmeübertragung durch Spritzwasserkühlung heißer Oberflächen im Bereich der stabilen Filmverdampfung.* PhD thesis, Technische Universität Clausthal.

Rini, D. P., Chen, R.-H., & Chow, L. C. (2002). Bubble behavior and nucleate boiling heat transfer in saturated FC-72 spray cooling. *ASME. J. Heat Transfer.*, 124(1):63–72.

Rioboo, R., Marengo, M., & Tropea, C. (2002). Time evolution of liquid drop impact onto solid, dry surfaces. *Exp. Fluids*, 33(1):112–124.

Rioboo, R., Tropea, C., & Marengo, M. (2001). Outcomes from a drop impact on solid surfaces. *Atomization Sprays*, 11(2):155–165.

Rioboo, R., Voué, M., Vaillant, A., & De Coninck, J. (2008). Drop impact on porous superhydrophobic polymer surfaces. *Langmuir*, 24(24):14074–14077.

Rohsenow, W. M. (1962). A method of correlating heat transfer data for surface boiling of liquids. *J. Heat Transfer*, 84:969.

Roisman, I. V. (2009). Inertia dominated drop collisions. II. An analytical solution of the navier–stokes equations for a spreading viscous film. *Phys. Fluids*, 21(5):052104.

Roisman, I. V. (2010). Fast forced liquid film spreading on a substrate: flow, heat transfer and phase transition. *J. Fluid Mech.*, 656:189–204.

Roisman, I. V., Berberović, E., & Tropea, C. (2009). Inertia dominated drop collisions. I: on the universal flow in the lamella. *Phys. Fluids*, 21(5):052103.

Roisman, I. V., Breitenbach, J., & Tropea, C. (2018). Thermal atomisation of a liquid drop after impact onto a hot substrate. *J. Fluid Mech.*, 842:87–101.

Roisman, I. V., Lembach, A., & Tropea, C. (2015). Drop splashing induced by target roughness and porosity: The size plays no role. *Adv. Colloid Interface Sci.*, 222:615–621.

Roisman, I. V., Rioboo, R., & Tropea, C. (2002). Normal impact of a liquid drop on a dry surface: model for spreading and receding. *Proc. R. Soc. Lond. A Math. Phys. Sci.*, 458(2022):1411–1430.

Roisman, I. V. & Tropea, C. (2005). Fluctuating flow in a liquid layer and secondary spray created by an impacting spray. *Int. J. Multiph. Flow*, 31(2):179–200.

Rolls Royce (2015). *The Jet Engine.* Wiley.

Rybicki, J. R. & Mudawar, I. (2006). Single-phase and two-phase cooling characteristics of upward-facing and downward-facing sprays. *Int. J. Heat Mass Transf.*, 49(1):5 – 16.

Saski, K., Sugitani, Y., & Kawasaki, M. (1979). Heat Transfer in Spray Cooling on Hot Surface. *Tetsu-to-Hagane*, 65(1):90–96.

Sawan, M. E. & Carbon, M. W. (1975). Spray-Cooling and Bottom-Flooding Work for LWR cores. *Nucl. Eng. Des.*, 32(2):191–207.

Scheller, B. L. & Bousfield, D. W. (1995). Newtonian drop impact with a solid surface. *AIChE J.*, 41(6):1357–1367.

Schmidt, J. B. (2018). *Experimental study of the heat flux during the drop impact onto a hot surface.* Master thesis, Technische Universität Darmstadt.

Schremb, M., Borchert, S., Berberovic, E., Jakirlic, S., Roisman, I. V., & Tropea, C. (2017). Computational modelling of flow and conjugate heat transfer of a drop impacting onto a cold wall. *Int. J. Heat Mass Transf.*, 109:971–980.

Scriven, L. (1959). On the dynamics of phase growth. *Chem. Eng. Sci.*, 10(1-2):1–13.

Sehmbey, M. S., Chow, L. C., Hahn, O. J., & Pais, M. R. (1995). Spray cooling of power electronics at cryogenic temperatures. *J. Thermophys. Heat Transfer*, 9(1):123–128.

Shedd, T. A. (2007). Next Generation Spray Cooling: High Heat Flux Management in Compact Spaces. *Heat Transfer Eng.*, 28(2):87–92.

Shirota, M., van Limbeek, M. A. J., Sun, C., Prosperetti, A., & Lohse, D. (2016). Dynamic Leidenfrost Effect: Relevant Time and Length Scales. *Phys. Rev. Lett.*, 116(6):064501.

Siemons, N., Bruining, H., Castelijns, H., & Wolf, K.-H. (2006). Pressure dependence of the contact angle in a CO2–H2O–coal system. *J. Colloid Interface Sci.*, 297(2):755–761.

Silk, E. A., Kim, J., & Kiger, K. (2006). Spray cooling of enhanced surfaces: impact of structured surface geometry and spray axis inclination. *Int. J. Heat Mass Transf.*, 49(25):4910–4920.

Sodtke, C. & Stephan, P. (2007). Spray cooling on micro structured surfaces. *Int. J. Heat Mass Transf.*, 50(19):4089–4097.

Staat, H. J. J., Tran, T., Geerdink, B., Riboux, G., Sun, C., Gordillo, J. M., & Lohse, D. (2015). Phase diagram for droplet impact on superheated surfaces. *J. Fluid Mech.*, 779.

Stephan, P. & Hammer, J. (1994). A new model for nucleate boiling heat transfer. *Heat Mass Transf.*, 30(2):119–125.

Stevens, C. S., Latka, A., & Nagel, S. R. (2014). Comparison of splashing in high-and low-viscosity liquids. *Phys. Rev. E*, 89(6):063006.

Synytska, A., Biehlig, E., & Ionov, L. (2014). Adaptive PEG–PDMS Brushes: Effect of Architecture on Adhesiveness in Air and under Water. *Macromolecules*, 47(23):8377–8385.

Tartarini, P., Lorenzini, G., & Randi, M. R. (1999). Experimental study of water droplet boiling on hot, non-porous surfaces. *Heat Mass Transf.*, 34(6):437–447.

Taylor, G. I. (1959). The dynamics of thin sheets of fluid. II. Waves on fluid sheets. *Proc. R. Soc. Lond. A Math. Phys. Sci.*, 253(1274):296–312.

Testa, P. & Nicotra, L. (1986). Influence of pressure on the Leidenfrost temperature and on extracted heat fluxes in the transient mode and low pressure. *J. Heat Transfer*, 108(4):916–921.

Thoroddsen, S. T., Etoh, T. G., Takehara, K., Ootsuka, N., & Hatsuki, Y. (2005). The air bubble entrapped under a drop impacting on a solid surface. *J. Fluid Mech.*, 545:203–212.

Tilton, D. E., Kearns, D. A., & Tilton, C. L. (1994). Liquid nitrogen spray cooling of a simulated electronic chip. In *Adv. Cryog. Eng.*, pages 1779–1786. Springer.

Tran, T., Staat, H. J. J., Prosperetti, A., Sun, C., & Lohse, D. (2012). Drop impact on superheated surfaces. *Phys. Rev. Lett.*, 108(3):036101.

Tropea, C. (2011). Optical Particle Characterization in Flows. *Annu. Rev. Fluid Mech.*, 43(1):399–426.

Tropea, C., Xu, T.-H., Onofri, F., Gréhan, G., Haugen, P., & Stieglmeier, M. (1996). Dual-Mode Phase-Doppler Anemometer. *Part. Part. Syst. Charact.*, 13(2):165–170.

Tsai, P., Pacheco, S., Pirat, C., Lefferts, L., & Lohse, D. (2009). Drop impact upon micro-and nanostructured superhydrophobic surfaces. *Langmuir*, 25(20):12293–12298.

Tsui, Y. C. & Clyne, T. W. (1997). An analytical model for predicting residual stresses in progressively deposited coatings .1. Planar geometry. *Thin Solid Films*, 306(1):23–33.

Ueda, T., Enomoto, T., & Kanetsuki, M. (1979). Heat Transfer Characteristics and Dynamic Behavior of Saturated Droplets Impinging on a Heated Vertical Surface. *Bull. JSME*, 22(167):724–732.

Ukiwe, C. & Kwok, D. Y. (2005). On the Maximum Spreading Diameter of Impacting Droplets on Well-Prepared Solid Surfaces. *Langmuir*, 21:666–673.

v. Kieckebusch, N. (2018). *Experimentelle Untersuchung des Aufpralls eines Tropfens auf eine beheizte Oberfläche: Einfluss von Oberflächenmaterialien und -strukturierungen.* Master thesis, Technische Universität Darmstadt.

van Dam, D. B. & Clerc, C. L. (2004). Experimental study of the impact of an ink-jet printed droplet on a solid substrate. *Phys. Fluids*, 16(9):3403–3414.

van Limbeek, M. A., Shirota, M., Sleutel, P., Sun, C., Prosperetti, A., & Lohse, D. (2016). Vapour cooling of poorly conducting hot substrates increases the dynamic Leidenfrost temperature. *Int. J. Heat Mass Transf.*, 97:101 – 109.

Van Stralen, S. J. D., Sohal, M. S., Cole, R., & Sluyter, W. M. (1975). Bubble growth rates in pure and binary systems: combined effect of relaxation and evaporation microlayers. *Int. J. Heat Mass Transf.*, 18(3):453–467.

Vander Wal, R. L., Berger, G. M., & Mozes, S. D. (2006). The splash/non-splash boundary upon a dry surface and thin fluid film. *Exp. Fluids*, 40(1):53–59.

Visaria, M. & Mudawar, I. (2008a). Effects of high subcooling on two-phase spray cooling and critical heat flux. *Int. J. Heat Mass Transf.*, 51(21):5269 – 5278.

Visaria, M. & Mudawar, I. (2008b). Theoretical and experimental study of the effects of spray inclination on two-phase spray cooling and critical heat flux. *Int. J. Heat Mass Transf.*, 51(9):2398 – 2410.

Visser, C. W., Frommhold, P. E., Wildeman, S., Mettin, R., Lohse, D., & Sun, C. (2015). Dynamics of high-speed micro-drop impact: numerical simulations and experiments at frame-to-frame times below 100 ns. *Soft Matter*, 11(9):1708–1722.

Wachters, L. & Westerling, N. (1966). The heat transfer from a hot wall to impinging water drops in the spheroidal state. *Chem. Eng. Sci.*, 21(11):1047 – 1056.

Wagner, W. & Kretzschmar, H.-J. (2007). *International Steam Tables-Properties of Water and Steam based on the Industrial Formulation IAPWS-IF97: Tables, Algorithms, Diagrams, and CD-ROM Electronic Steam Tables-All of the equations of IAPWS-IF97 including a complete set of supplementary backward equations for fast calculations of heat cycles, boilers, and steam turbines.* Springer Science & Business Media.

Walzel, P. (1980). Zerteilgrenze beim Tropfenprall. *Chem. Ing. Tech.*, 52(4):338–339.

Wang, H., Wu, J., Yang, Q., Zhu, X., & Liao, Q. (2016). Heat transfer enhancement of ammonia spray cooling by surface modification. *Int. J. Heat Mass Transf.*, 101:60–68.

Wang, Y., Liu, M., Liu, D., Xu, K., & Chen, Y. (2010). Experimental study on the effects of spray inclination on water spray cooling performance in non-boiling regime. *Exp. Therm Fluid Sci.*, 34(7):933 – 942.

Weiss, D. A. & Yarin, A. L. (1999). Single drop impact onto liquid films: neck distortion, jetting, tiny bubble entrainment, and crown formation. *J. Fluid Mech.*, 385:229–254.

Wendelstorf, J., Spitzer, K.-H., & Wendelstorf, R. (2008a). Spray water cooling heat transfer at high temperatures and liquid mass fluxes. *Int. J. Heat Mass Transf.*, 51(19):4902–4910.

Wendelstorf, R., Spitzer, K.-H., & Wendelstorf, J. (2008b). Effect of oxide layers on spray water cooling heat transfer at high surface temperatures. *Int. J. Heat Mass Transf.*, 51(19):4892 – 4901.

Wildeman, S., Visser, C. W., Sun, C., & Lohse, D. (2016). On the spreading of impacting drops. *J. Fluid Mech.*, 805:636–655.

Willis, K. D. & Orme, M. E. (2000). Experiments on the dynamics of droplet collisions in a vacuum. *Exp. Fluids*, 29(4):347–358.

Worthington, A. M. (1876). On the forms assumed by drops of liquids falling vertically on a horizontal plate. *Proc. R. Soc. Lond.*, 25(171-178):261–272.

Worthington, A. M. & Cole, R. S. (1897). Impact with a liquid surface, studied by the aid of instantaneous photography. *Phil. Trans. R. Soc. Lond. A*, 189:137–148.

Xu, L., Zhang, W. W., & Nagel, S. R. (2005). Drop splashing on a dry smooth surface. *Phys. Rev. Lett.*, 94(18):184505.

Yamanouc, A. (1968). Effect of Core Spray Cooling in Transient State after Loss of Coolant Accident. *J. Nucl. Sci. Technol.*, 5(11):547–558.

Yang, J., Chow, L. C., & Pais, M. R. (1996). Nucleate boiling heat transfer in spray cooling. *ASME. J. Heat Transfer.*, 118(3):668–671.

Yao, S. & Choit, K. (1987). Heat transfer experiments of mono-dispersed vertically impacting sprays. *Int. J. Multiph. Flow*, 13(5):639 – 648.

Yao, S.-C. & Cai, K. Y. (1988). The dynamics and Leidenfrost temperature of drops impacting on a hot surface at small angles. *Exp. Therm. Fluid. Sci.*, 1(4):363–371.

Yao, S. C. & Cox, T. L. (2002). A general heat transfer correlation for impacting water sprays on high-temperature surfaces. *Exp. Heat Transfer*, 15(4):207–219.

Yao, S.-C. & Henry, R. E. (1978). An investigation of the minimum film boiling temperature on horizontal surfaces. *J. Heat Transfer*, 100(2):260–267.

Yarin, A. L. (2006). Drop impact dynamics: Splashing, spreading, receding, bouncing... *Annu. Rev. Fluid Mech.*, 38:159–192.

Yarin, A. L., Roisman, I. V., & Tropea, C. (2017). *Collision Phenomena in Liquids and Solids*. Cambridge University Press, Cambridge.

Yarin, A. L. & Weiss, D. A. (1995). Impact of drops on solid surfaces: self-similar capillary waves, and splashing as a new type of kinematic discontinuity. *J. Fluid Mech.*, 283:141–173.

Zenzie, H. H., Altshuler, G. B., Smirnov, M. Z., & Anderson, R. R. (2000). Evaluation of cooling methods for laser dermatology. *Lasers Surg. Med.*, 26(2):130–144.

Zhang, Z., Jiang, P.-X., Ouyang, X.-L., Chen, J.-N., & Christopher, D. M. (2014). Experimental investigation of spray cooling on smooth and micro-structured surfaces. *Int. J. Heat Mass Transf.*, 76:366 – 375.

Zhang, Z., Li, J., & Jiang, P.-X. (2013). Experimental investigation of spray cooling on flat and enhanced surfaces. *Appl. Thermal Eng.*, 51(1):102 – 111.

Zhong, L. & Guo, Z. (2017). Effect of surface topography and wettability on the Leidenfrost effect. *Nanoscale*, 9(19):6219–6236.

List of Figures

List of Tables